

Development and Evaluation of a Power Management System for an Off-grid Power System with PV Generation and Energy Storage

by

Mo'ath Ramadan Mustafa Farraj

A thesis submitted to the Faculty of Graduate Studies of

The University of Manitoba

in partial fulfilment of the requirements for the degree of

MASTER OF SCIENCE

Department of Electrical and Computer Engineering

University of Manitoba

Winnipeg.

Copyright © 2021 by Mo'ath Ramadan Mustafa Farraj

Abstract

Utilization of locally available solar energy resources alongside energy storage has emerged as a feasible renewable retrofit to the solely diesel generation-based remote off-grid power systems. The declining cost and improving reliability of photovoltaic (PV) systems, battery energy storage systems (BESS), and power electronics components have contributed to accelerate this trend. The integration of inverter-interfaced Distributed Energy Resources (DERs) such as solar PV systems and BESS along with conventional generation resources significantly increases the complexity of these isolated power grids. Therefore, a hierarchical control system consisting of an energy management system, a power management system and the local controllers of generating and storage resources is often employed to achieve a reliable, secure, and stable power system operation.

This thesis develops a real-time simulation model of an isolated power system based on the typical configuration of power systems in remote communities of Northern-Canada. The isolated grid includes a diesel generation plant, a PV system and a BESS with the diesel generators forming the grid under normal operation. Control strategies for the PV system and the BESS under both grid-following and grid-forming modes of operation are discussed. This thesis develops a secondary control layer of a hierarchical microgrid control system to perform power management functions and implements them on a digital automation controller. In order to demonstrate the functionality of the proposed microgrid controller, a Controller Hardware in the Loop (CHIL) simulation testbed is developed. The structure of the testbed, the development and coordination of different levels in the hierarchical control system, and the integration of the IEC-61850 communication for

information exchange among various components are discussed. The overall study confirms the effectiveness of the proposed hierarchical controller as well as the applicability of the developed testbed in providing a realistic operation evaluation platform.

Acknowledgment

This research was completed with significant support from various individuals and institutes. My sincere thanks go out to all those who helped me throughout my research process.

First and foremost, I would like to acknowledge my supervisor Prof. Athula Rajapakse. This research would not be possible without his guidance, encouragement, and dedication.

Then, I would like to express my deepest gratitude to Schweitzer Engineering Laboratories (SEL), for providing the digital controller for the completion of this research.

Additionally, I am grateful for the support and guidance received from Mr. Victor Menezes from SEL and Mr. Ken Hamilton from Pro-Tech Power Sales Inc. on choosing a suitable hardware device and facilitating its donation.

Mr. Shrimal Koruwage deserves special thanks for providing technical and IT support whenever necessary.

My last words of thanks go to my parents, who have always nurtured, supported, pushed, motivated and made me the person I am today.

Dedication

To my beloved family.....

Table of Contents

Chapter 1	Introduction.....	1
1.1	Background.....	1
1.2	Research Motivation.....	6
1.3	Research Objectives.....	8
1.4	Thesis Organization.....	9
Chapter 2	Literature Review.....	10
2.1	Microgrid Controller Requirements.....	10
2.1.1	Microgrid Controller Functions.....	13
2.2	Microgrid Controller Communication.....	14
2.2.1	IEC 61850 Standard for Substation Automation.....	15
2.2.2	IEC 61850 Modelling.....	16
2.2.3	Generic Object Oriented Substation Event (GOOSE) Messaging.....	16
2.3	Implementation of Microgrid Controllers.....	17
2.4	Microgrid Control System Testing.....	19
2.4.1	Core Level Functions Testing.....	20
2.4.2	Test Metrics.....	21
2.5	Operating Modes of Power Converters in Microgrids.....	21

2.5.1	Grid-following Inverters	22
2.5.2	Grid-forming Inverters.....	23
2.5.3	Grid-supporting Inverters.....	26
2.6	Previous Work on Microgrid Controls	27
Chapter 3 System Configuration, Model and Control		30
3.1	Introduction.....	30
3.2	System Description	30
3.3	Diesel Plant	32
3.3.1	Speed Reference Generator.....	33
3.3.2	Voltage Reference Generator.....	36
3.4	Photovoltaic System.....	38
3.4.1	PV Array Model.....	39
3.4.2	Average Value Models (AVMs) of Power Converters.....	42
3.4.3	PV System Control Strategy	46
3.5	Battery Energy Storage System	55
3.5.1	Battery Array Model	55
3.5.2	Average Value Models of Power Converters	56
3.5.3	BESS Control Strategy	57
3.6	Results and Discussion	60

3.6.1	GENSUP mode	60
3.6.2	Islanded mode	65
3.6.3	PV-BESS Joint Grid-forming	68
3.7	Summary	71
Chapter 4 Power Management System		72
4.1	Introduction	72
4.2	Power Management System Core Functions	72
4.2.1	Dispatch Function	72
4.2.2	Transition Function	80
4.3	Summary	83
Chapter 5 Microgrid Testbed		84
5.1	Introduction	84
5.2	Elements of the Microgrid Testbed	84
5.2.1	Energy Management System	86
5.2.2	Power Management System	87
5.2.3	Communication Links	87
5.2.4	Human Machine Interface (HMI)	88
5.3	Performance Testing	90
5.3.1	Results – PMS Functions	90

5.4	Summary	104
Chapter 6	Conclusions.....	105
6.1	Contributions and Conclusions.....	105
6.2	Future Work	108
Appendix. A		109
References		111

List of Tables

Table 2-1: Transition function state.....	19
Table 4-1: Constraints of dispatch function.....	73
Table 4-2: Synchronization parameters limits [2].	81
Table A-1: SEL RTAC input and output signals.....	109
Table A-2: EMS input and output signals.....	110

List of Figures

Figure 1-1: Hierarchical structure of a microgrid control system.....	5
Figure 2-1: Microgrid components.	10
Figure 2-2: Interactions between core level functions [12].	13
Figure 2-3: IEC 61850 data model.....	16
Figure 2-4: State diagram of FSM.	18
Figure 2-5: Grid-following inverter equivalent representation [36].	23
Figure 2-6: Grid-forming inverter representation [36].	24
Figure 2-7: Single master operation schematic in islanded microgrid [38].	25
Figure 2-8: Multi-master operation schematic in islanded microgrid [38].	26
Figure 2-9: Grid-supporting inverter representation [36].	27
Figure 3-1: Microgrid test system.....	31
Figure 3-2: Diesel generator model schematic [55].	33
Figure 3-3: Schematic of speed reference (<i>wref</i>) generator.....	34
Figure 3-4: $P - w$ (active power – speed) droop curve.....	35
Figure 3-5: Speed reference secondary controllers.....	36
Figure 3-6: Active power reference generator.	36
Figure 3-7: Schematic of voltage reference generator.....	37
Figure 3-8: $Q - V$ (reactive power – voltage) droop curve.	37

Figure 3-9: Voltage reference secondary controllers.....	38
Figure 3-10: Reactive power set generator.	38
Figure 3-11: Schematic of the PV system.....	39
Figure 3-12: RTDS PV array model.	39
Figure 3-13: Solar cell model.	40
Figure 3-14: Typical I-V characteristics for a solar cell.	42
Figure 3-15: AVM of VSC.	44
Figure 3-16: Boost converter.	44
Figure 3-17: one cycle of the switching input ($g1$).....	45
Figure 3-18: AVM of a Boost DC/DC converter.....	46
Figure 3-19: PV system control structure.	47
Figure 3-20: VSC current controller.	48
Figure 3-21: PV-VSC power control loop.....	49
Figure 3-22: PV-VSC voltage control loops.....	50
Figure 3-23: Frequency external control loop.	52
Figure 3-24: PV-VSC power reference generator schematic.	53
Figure 3-25: PV array controller.....	54
Figure 3-26: BESS system.....	55
Figure 3-27: Battery model equivalent circuit.....	56

Figure 3-28: Buck/boost converter circuit used in BESS	56
Figure 3-29: Buck/boost AVM equivalent model.	57
Figure 3-30: Schematic of BESS control strategy.	58
Figure 3-31: Battery controller schematic.	59
Figure 3-32: GENSUP mode: (a) Active power, (b) Reactive power, (c) AC voltage, and (d) Frequency.	61
Figure 3-33: GENSUP mode: (a) Active power, (b) Reactive power, (c) Frequency, and (d) AC voltage.	63
Figure 3-34: Diesel plant control: (a) Active power, (b) Reactive power, (c) Frequency, and (d) AC voltage.	65
Figure 3-35: Islanded mode: (a) Active power, (b) Reactive power, (c) Frequency, and (d) AC voltage.	67
Figure 3-36: PV limited power mode: (a) Active power, and (b) PV voltage.	68
Figure 3-37: PV-BESS joint grid-forming: (a) Active power, (b) Reactive power, (c) Frequency, and (d) AC voltage.	70
Figure 3-38: VSC droop limited power mode: (a) Active power, and (b) SOC.	71
Figure 4-1: GENSUP dispatch strategy.	74
Figure 4-2: Decision tree to FSM conversion.	76
Figure 4-3: Dispatch strategy in islanded mode.	78
Figure 4-4: Planned islanding transition process.	80

Figure 4-5: Reconnection process scheme.....	82
Figure 5-1: CHIL testbed testing platform.....	85
Figure 5-2: Laboratory setup.	86
Figure 5-3: Single line diagram of the HMI.	88
Figure 5-4: BESS HMI dashboard.....	89
Figure 5-5: Active and reactive power trends.....	89
Figure 5-6: Emergency diesel generator transition during the GENSUP operation: (a) active power, (b) reactive power, (c) SOC, (d) frequency, and (e) AC voltage.....	91
Figure 5-7: Power management when BESS reaches minimum SOC while in GENSUP mode: (a) active power, (b) reactive power, (c) SOC, (d) frequency, and (e) AC voltage.	92
Figure 5-8: Emergency connection of a diesel generator in islanded mode (a) active power, (b) reactive power, (c) SOC, (d) frequency, and (e) AC voltage.....	93
Figure 5-9: Islanded energy reserve scheme: (a) active power, (b) reactive power, (c) SOC, (d) frequency, and (e) AC voltage.	95
Figure 5-10: Unplanned islanding: (a) active power, (b) reactive power, (c) SOC, (d) frequency, and (e) AC voltage.....	96
Figure 5-11: Optimum operational routine: (a) Forecasts, (b) dispatch, and (c) SOC.	97
Figure 5-12: System actual operation: (a) active power, (b) reactive power, and (c) SOC.	98

Figure 5-13: Diesel minimum loading scenario (8th hour): Active power.....	99
Figure 5-14: DIS-1 overloading scenario (23rd hour): Active power.	100
Figure 5-15: Results from 15th hour, when SOC reaches <i>SOCMAX</i> : (a) active power and (b) SOC.....	101
Figure 5-16: Planned islanding at the start of 9th hour: (a) active power, (b) reactive power, (c) frequency, (d) AC voltage, (e) diesel unit breaker status, and (f) BESS control mode.	102
Figure 5-17: Reconnection at the start of 21st hour: (a) active power, (b) reactive power, (c) frequency, (d) AC voltage, (e) diesel unit breaker status, and (f) BESS control mode.	103

List of Abbreviations

DER	Distributed Energy Resource
PV	Photovoltaic
BESS	Battery Energy Storage System
CHIL	Controller Hardware in the Loop
DG	Distributed Generation
DS	Distributed Storage
MGCC	Microgrid Central Controller
PMS	Power Management System
SOC	State of Charge
EMS	Energy Management System
PHIL	Power Hardware in the Loop
DRTS	Digital Real Time Simulator
HIL	Hardware in the Loop
MBE	Model-based Engineering
HDUT	Hardware Device under Test
POI	Point of Interconnection
EDO	Emergency Dispatch Order
GOOSE	Generic Object Oriented Substation Event
IED	Intelligent Electronic Device
SV	Samples Values
MMS	Manufacturing Message Specification
FSM	Finite State Machines
PLC	Programmable Logic Controller
ST	Structured Text
PLL	Phase-locked Loop

VSG	Virtual Synchronous Generator
HESS	Hybrid Energy Storage System
SC	Super Capacitor
PWM	Pulse Width Modulation
AVM	Average Value Model
MPP	Maximum Power Point
MPPT	Maximum Power Point Tracking
PF	Power Factor
RGC	Reserve Generation Capacity
HMI	Human Machine Interface
SEL	Schweitzer Engineering Laboratories

Chapter 1

Introduction

1.1 Background

Owing to various measures taken to reduce to the impact of increasing demand of electricity on climate change, the contribution of renewable energy for electricity generation is rapidly expanding. As a result of utilities providing access to interconnecting renewable energy resources, such as wind and Photovoltaics (PV) at local end-user points, the structure of the conventional power distribution systems is evolving to incorporate microgrids [1]. The significant integration of Distributed Energy Resources (DERs) at distribution voltage level is due to several economical and environmental benefits: low capital cost of DERs, reduced carbon emissions due to replacement of conventional generators, increased reliability and resiliency of local grids and reduction of transmission losses.

A microgrid is a local group of DERs and loads operating as a single unit in both grid-connected and islanded mode [2]. DERs can be either Distributed Generation (DG) or Distributed Storage (DS) units connected at medium or low voltage levels [3]. DG units are usually renewable resources such as PV and wind generators. DS units are typically batteries but can be formed by supercapacitors, flywheels or any other energy storage technology.

DERs are classified into two groups according to the type of interface with the grid. Conventional DGs based on rotating machines, such as diesel generators, fixed-speed wind turbines and small hydro generators are directly connected to the grid. On the other hand, many renewable energy-based generation and energy storage such as PV, wind and batteries are interconnected through power electronics converters. The control system of conventional rotary machines is very well understood by the utility engineers. On the other hand, power electronic converters that interface DER require more complex control strategies and several control modes. Depending on the requirements, they may operate as constant real and reactive power generators in PQ control mode or contribute to regulate the network voltage and frequency operating in Vf control mode. They are also expected to behave in a specific way during grid disturbances.

Rapid integration of renewable energy sources and storage methods to retrofit diesel-based resources has been perceived as a feasible solution to deal with many economic and environmental concerns prevailing in remote microgrids [4]. The modular nature of PV enables gradual expansion making investments manageable and avoiding idle capacity. Due to the intermittency of solar radiation, PV power generation is often classified as non-dispatchable [3]. Therefore, when considering isolated distribution networks, PV units are often integrated alongside a dispatchable DG or a DS unit. As a result, PV-Diesel-Battery renewable energy system topology at high PV penetration levels is emerging as a reliable and cost-effective solution to remote off-grid power systems, representing a satisfactory compromise between the high capital cost of PV and the expenses associated with operation and maintenance of diesel generators [4]–[6]. A diesel generator is capable of generating power at anytime, which deals with the PV uncertainty and makes the system

more reliable. Furthermore, the installation of batteries makes the diesel generators run less frequently and at more efficient operating points minimizing the fuel consumption [7]. In such power systems, for periods with high renewable power generation, economic dispatch models show that it is economical to meet the load demand and reserve requirements solely by the inverter-interfaced PV and battery units without any diesel generator [8]. Such microgrids should have the capability to operate with and without the diesel generation to enhance grid efficiency, security, and resiliency. The operation of inverter-interfaced renewable resources along with existing conventional power resources requires complex control algorithms, energy management systems and protection schemes.

A microgrid control system is required to achieve a set of objectives pertained by the microgrid assets. It is responsible of optimizing the operation of microgrid DERs by providing them with appropriate reference commands under both grid-connected and islanded modes. It should also have the capability to manage smooth transitions by initiating islanding/synchronizing commands and take appropriate actions responding to abnormal events. As shown in Figure 1-1, a microgrid control system has a hierarchical structure and consists of three layers based on their response time, namely the primary, secondary and tertiary controls [9], [10]. The primary control acts in a very short time frame and is responsible of maintaining a stable voltage and frequency in the microgrid and sharing the load between DERs, preferably without communication links. The primary controls of inverter interfaced DER include the local voltage and current control loops referred to as Vf and PQ control [9], [10].

The secondary control layer has a slower response than that of the primary and usually implemented inside a central Microgrid Central Controller (MGCC), representing a Power Management System (PMS). Its is conceived to monitor real-time system conditions and maintain the microgrid power balance, voltage and frequency within acceptable levels while following the optimum operation routine suggested by the tertiary level. Moreover, the secondary level controls ensure the safety of equipment and quality of supply by computing the appropriate command and reference signals for the primary level control while enforcing a set of constraints such as minimum loading of diesel generators, battery State of Charge (SOC) limits, and device ratings. In addition, the secondary controller includes synchronization and islanding control signals to transfer the microgrid smoothly and seamlessly between isolated and grid-connected modes in conjunction with appropriately switching inverter control modes between PQ and Vf [11].

The tertiary control optimizes the overall operation of the microgrid over longer timeframe usually expanding hours to days, representing an Energy Management System (EMS) [11]. Standards such as the IEEE 2030 suite of standards are being developed to guide various aspects of the development of microgrids. Specifically, the IEEE 2030.7-2017 standard outlines the specific requirements and tasks of microgrid controllers to help the development of microgrid control system functions [12].

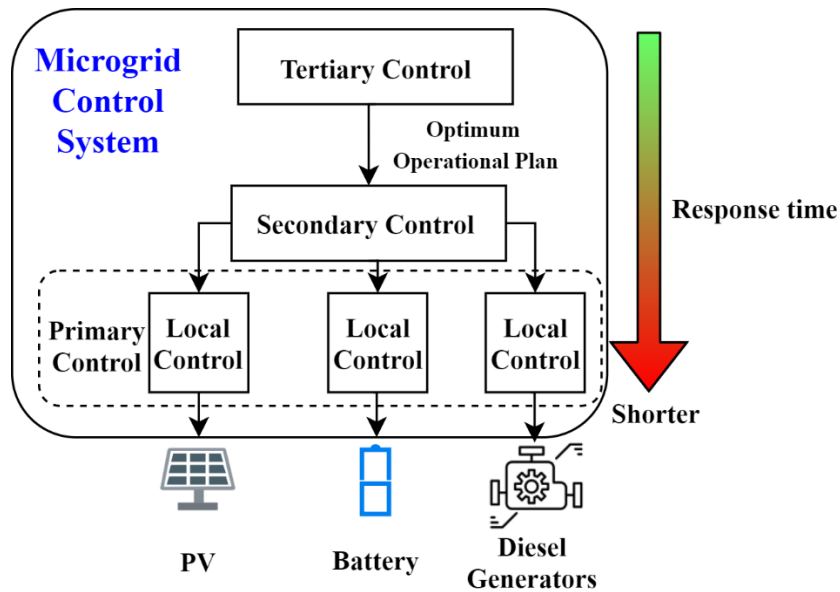


Figure 1-1: Hierarchical structure of a microgrid control system.

A microgrid control system is generally specific to the microgrid site and therefore it should be assessed within an environment capable of conducting different conditions anticipated to occur on-site. IEEE 2030.8-2018 standard gives some guidance in this regard and describes test scenarios that can be used to assess whether a microgrid controller complies with the requirements specified in IEEE 2030.7-2017 standard [13]. In order to perform diverse test scenarios, the development of flexible tools for microgrid control systems testing is becoming an important need.

Pure simulation, Controller Hardware in the Loop (CHIL) simulation, Power Hardware in the Loop (PHIL) simulation, and testing using hardware are different techniques to evaluate the performance of microgrid control systems [14]. Pure simulation is the cheapest method and is usually used by the researchers and engineers at the initial phase of development. However, real-world challenges such as communication and interoperability are not reflected in pure simulation-based assessment. On the other hand, testing using a setup

containing only physical devices such as CERTS microgrid [15] provide a high fidelity test environment, but its associated with more costs and space requirements. Furthermore, a physical test bench involving a fixed or limited hardware configuration is not flexible to test various experimental scenarios. Therefore, hardware in the loop (both CHIL and PHIL) has become a popular method to validate microgrid control systems [16]. It involves interfacing hardware with a Digital Real Time Simulator (DRTS) such as RTDS® through a communication medium, offering more closer real-world testing conditions. In the literature, there are many real-time implementations of microgrid controllers [17]–[20]. However, only a few studies [21], [22] involve developing and validating microgrid controllers in compliance with the emerging IEEE standards.

1.2 Research Motivation

To reduce the risk of undesirable operation of a microgrid control system, its performance must be validated before integrating to the actual power system. Real-time simulators enabling Hardware in the Loop (HIL) simulations, which are built on the principles of Model-based Engineering (MBE) has become the growing trend to perform such validation tasks in a more effective and economical manner. In HIL simulations, parts of the power system are modeled in a software environment and interfaced with a physical Hardware Device under Test (HDUT) using analog and digital signals outputs of the real-time simulator, or through a communication protocol. When the integrated hardware involves a controller, the testbed falls under a special category referred to as CHIL, which is the primary focus of this research. Using CHIL technology, the controller performance can be evaluated through a wide array of scenarios, some of which can be impractical or rather

risky to perform in real life. Also, the designed testbed could facilitate faster and more accurate design iterations in a time saving and cost-effective way than with actual physical tests. Most importantly the use of HIL in conjunction with controllers allows the designed controller algorithms to be tested and vetted to comply with IEEE 2030 standards for testing and developing microgrid controllers before deployment to the field. So far, the CHIL technology and its associated modelling platform has been used for time domain short-circuit, failure mode, and coordination analysis; interoperability and functional testing; and testing performance and reliability of the controller's hardware, firmware, software and communications systems.

Although there are several sophisticated microgrid controllers available in the market deploying very advanced algorithms, they are generally expensive and still need to be customized to the specific microgrid. Expensive grid controlling software and hardware platforms are not affordable for many small players connected to the grid, and the development of low cost and readily available options are needed. Also, once purchased, the buyers are often left with a blackbox in terms of underlying algorithms governing the controller functionality. So, any modifications in relation to the future requirements becomes a challenging task. Also, every time the software on one component is upgraded, the engineers must ensure the accurate functionality of the whole system. A HIL testbed allows the components to be tested independently and as part of the system before bringing the system back online. Also, the ability to deploy one testing tool from design to deployment can reduce the engineering time and costs. Furthermore, majority of HIL testbeds implementations are limited to a microgrid connected to a stiff grid and have been

developed without conforming to the acknowledged standards. These research gaps and prospects motivated this research.

1.3 Research Objectives

The main objective is to develop a microgrid controller and a CHIL test system for a remote isolated power system consisting of diesel generation, PV generation and battery energy storage. The specific objectives include:

- Studying the current state of the art in developing microgrid control functions, and identification of the advantages, limitations, and implementation challenges associated with different methods.
- Development of a real-time simulation model of an example isolated microgrid.
- Identifying control requirements during all modes of operation and during transitions between the modes, and design of required control algorithms with the help of simulation studies.
- Selection of a suitable hardware device and implementation of the control algorithms associated with secondary control functions in compliance with IEEE 2030.7-2017 standard.
- Validating the performance of the implemented controls using controller hardware in the loop real-time simulations following IEEE 2030.8-2018 standard.

1.4 Thesis Organization

Chapter 1 provides the background, motivation, and objectives of this thesis.

Chapter 2 presents a literature review about the requirements and testing of microgrid controllers, and the IEEE 2030 suite standards. An overview of power converter operating modes is also provided.

Chapter 3 describes the modelling of the microgrid study system and its associated control loops. Simulation results under various operating scenarios are also presented to justify the models.

Chapter 4 presents the development of the power management functions for the considered microgrid in compliance with IEEE 2030.7-2017 standard.

Chapter 5 develops and demonstrates the test setup for performing CHIL simulations. Testing scenarios to validate the performance of the testbed are also presented.

Chapter 6 provides the conclusions, contributions, and future work.

Chapter 2

Literature Review

This chapter introduces microgrid control requirements, the methods used to assess the performance of a microgrid control system, and the control strategies commonly used for the power converters in microgrids.

2.1 Microgrid Controller Requirements

A microgrid control system supervises the components within a microgrid, achieving coordinated operation. Figure 2-1 shows the arrangement of a microgrid.

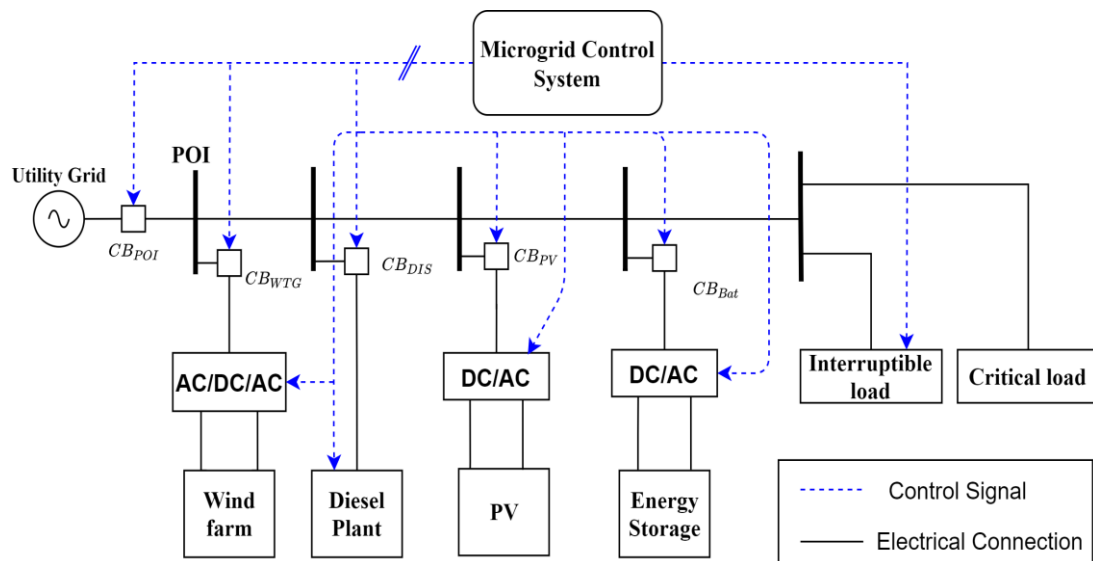


Figure 2-1: Microgrid components.

Integrating DERs to the distribution grid requires a microgrid controller to interact with the main grid as a single entity with the capability of supervising DERs, local loads, and

intertie equipment within the microgrid system. The microgrid controller can be distributed through the microgrid or centralized in a single controller.

The functions of a microgrid controller should include an EMS in order to ensure optimal operation of the microgrid in both grid-connected and islanded modes by managing the energy exchange within the microgrid while being subjected to economical, technical, and environmental constraints. The EMS optimizes the overall operation of microgrid, typically over a time window of 24 hours, by optimally scheduling the commitment and dispatch of energy resources according to the forecasted load consumption, renewable generation, and microgrid conditions. The term energy management is sometimes used in literature to refer to short-term power balancing functions. However, in this thesis, short-term power balancing function will be referred to as power management to distinguish it from long-term energy management. The long-term energy management is responsible for the following [3], [23]:

- Schedule optimal unit-commitment and dispatch (active and reactive power setpoints) for dispatchable DERs while maintaining adequate reserve capacity based on a suitable optimization framework to achieve a set of objectives, such as minimizing the overall operation cost, maximizing the output of renewable DERs, minimizing the power losses, meeting the Point of Interconnection (POI) power exchange requirements, or a combination of several objectives.
- Perform demand response.
- Load and resource forecasting.

The short-term power balancing or power management is responsible for the following tasks [3], [23]:

- Voltage and frequency regulation.
- Balancing power generation and demand by taking appropriate actions such as load shedding.
- Restoration of loads that are shed in response to a power mismatch or islanding event.
- Restoration of acceptable voltage and frequency following the dynamic response upon islanding.
- Resynchronization of the islanded microgrid with the main grid in response to a reconnection command.

In this thesis, the long-term energy management system will be called EMS, whereas the short-term power balancing controllers will be termed PMS.

Since microgrid topologies and elements differ depending on the expected operating conditions and the objectives of the microgrid, the developed microgrid control system functions and requirements should be specific to a microgrid. However, there are some minimum functional specifications which all microgrid control systems should satisfy as stated in the IEEE 2030.7-2017 standard, which provides technical specifications and requirements of microgrid controllers. The main objective of IEEE 2030.7-2017 is to allow the standardization of microgrid control systems and ultimately offer more flexibility when developing a microgrid control system. Core level functions, which are transition and dispatch functions are stated as the minimum requirements of a microgrid controller by IEEE 2030.7-2017 standard [12].

2.1.1 Microgrid Controller Functions

2.1.1.1 Dispatch Function

The dispatch function balances power generation and demand under various operating conditions, re-dispatches DERs according to the changes in load and generation, and responds to external orders, such as interconnection agreement requirements [12].

2.1.1.2 Transition Function

The objective of the transition function is to manage the transitions of the microgrid by switching the dispatch function between different modes in response to the following four transition modes [12]:

- Unplanned islanding.
- Planned islanding.
- Reconnect.
- Black start.

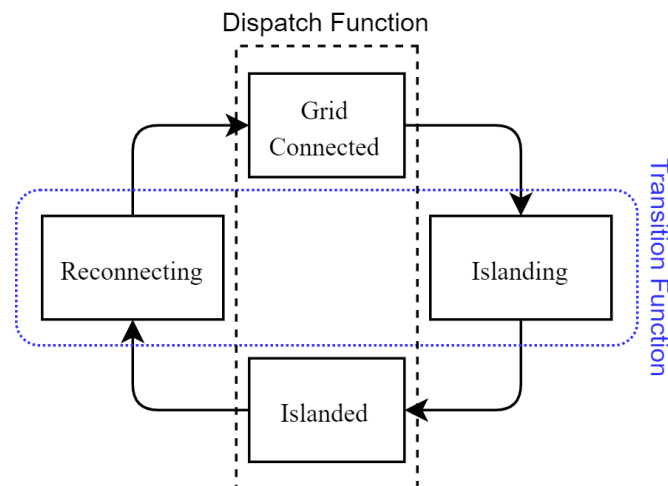


Figure 2-2: Interactions between core level functions [12].

The relationship between dispatch and transition functions is shown in Figure 2-2. For planned islanding, local DGs become primarily responsible for supplying local loads of the microgrid and subsequently reduce the power at POI to zero for smooth islanding. Reconnection refers to matching the microgrid voltage, frequency, and phase angle over both sides of the POI circuit breaker to facilitate seamless microgrid reconnection with the main grid. Black start can be defined as the capability of the microgrid to self-start and energize itself in the absence of the main grid.

The microgrid unplanned islanding occurs when the microgrid suddenly disconnects from the main grid due to external fault or abnormal events. Upon unplanned islanding, balancing the difference between available generation and demand in the island, and modification of the control mode of DERs are handled by executing an Emergency Dispatch Order (EDO). EDO is a procedure to match the available generation and load demand and stabilize the microgrid conditions by taking appropriate actions, such as re-dispatching microgrid resources, switching DERs control modes, and load shedding [12].

2.2 Microgrid Controller Communication

Exchanging information and control signals between different microgrid control levels and devices is very crucial to achieve proper operation of a microgrid. A microgrid communication network should be reliable, fast and facilitating bi-directional data exchange. Industrial communication protocols such as DNP3 and Modbus have been used in electrical networks over TCP/IP internet protocol [24], [25]. However, these protocols are based on the master-slave communication model and a failure in the master unit leads to a complete shutdown of the communication system. Furthermore, slave units are

incapable of initiating communications with the master unit, which could result in under-utilization of the resources [26]. On the other hand, the IEC-61850 substation communication standard is widely accepted by the industry and has the potential for use in microgrid communication network implementation [26]. This standard aims to improve reliability, availability, and most importantly interoperability. Next subsection gives a brief description of IEC 61850 standard and Generic Object Oriented Substation Event (GOOSE) messaging protocol used in this thesis.

2.2.1 IEC 61850 Standard for Substation Automation

The International Electrotechnical Commission introduced IEC 61850 as a new international standard for substation automation in the early 2000s [27]. Its capability to facilitate the integration of all substation functions, such as protection and control has brought wide acceptance from the industry. Furthermore, IEC 61850 supports self-description, which enables an Intelligent Electronic Device (IED) to display its content to a client. The IEC- 61850 standard aims to standardize communications for substation automation systems [28] and defined three communication protocols [27], [29]:

- Samples Values (SV) protocol as a publisher/subscriber type communication for continuous transmission of the sampled values of analog signals in regular intervals.
- GOOSE as a publisher/subscriber type communication for communicating data related to regular or irregular events.
- Manufacturing Message Specification (MMS) protocol as a server/client type communication for communicating reports, event logs, etc.

2.2.2 IEC 61850 Modelling

The IEC 61850 hierarchy models IEC 61850 objects in order to organize the data across different brands of IEDs, and it contains the following [28]:

- Physical Devices
- Logical Devices
- Logical Nodes
- Data Classes

The physical device can consist of many logical devices and acts as a proxy or gateway for the logical devices. Logical devices have several logical nodes, which represent an intelligent part of the device such as a circuit breaker. Each logical node has preassigned data classes, allocating a list of data set and their attributes [28]. An IEC 61850 object name hierarchy can be represented as shown in Figure 2-3.

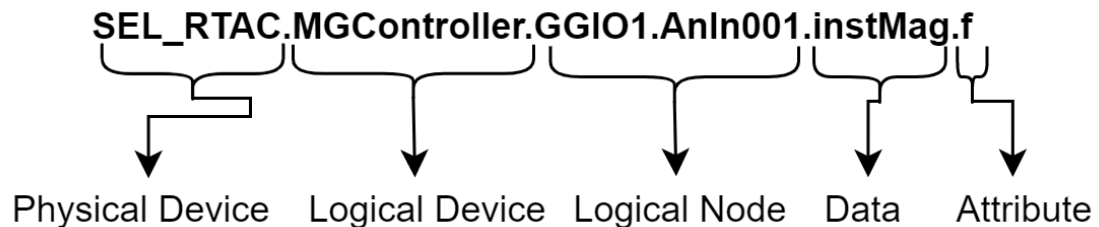


Figure 2-3: IEC 61850 data model.

2.2.3 Generic Object Oriented Substation Event (GOOSE) Messaging

GOOSE is a peer-to-peer messaging service and is usually employed for high-speed control messaging applications. GOOSE model is based on a publish-subscribe communication service model to facilitate exchanging data between several IEDs [30]. The exchanged data is converted to binary signals and transmitted through TCP/IP protocol over the ethernet to

a local network. Furthermore, the GOOSE data object publishes a message multiple times over the network with a fixed pattern until a new message is initiated. This continuous transmission helps to monitor the connectivity and establish a reliable communication link between IEDs [30], [31]. Also, GOOSE data messages can carry both analog and binary values, which makes them suitable for various substation applications such as automation, protection, and monitoring [29].

Each IEC 61850 GOOSE message has unique properties, which include a text identification string, APP ID field, and an Ethernet Multicast Group Address. These properties are used by the IEDs to capture and filter the incoming messages.

2.3 Implementation of Microgrid Controllers

Some systematic framework is required for orderly implementation of microgrid controllers, especially when there is a large number of elements involved in a microgrid. Among various approaches available, Finite State Machines (FSM) is a simple computational model that represents the logic design of many computer and automation applications. It is usually employed in designing the diagram models of sequential logic circuits, such as robots, vending machines and traffic lights [32], [33]. In this research, FSM and decision trees were used to code and represent the proposed PMS.

An FSM consists of multiple states and transitions linking pair of states. The circles denote the states of the machine and are labelled with the name of the state. An arrow linking pair of states represents the transition directly from a state to the destination state. The transitions are labelled with conditions (inputs) that cause the transition to occur. The initial state is marked by an incoming arrow. A double circle state indicates the final state, which

means if the input leads to a final state, the input is accepted by the automata. However, a machine without a final state can accept any input [32], [33]. An example of a state diagram demonstrating an example of FSM is depicted in Figure 2-4.

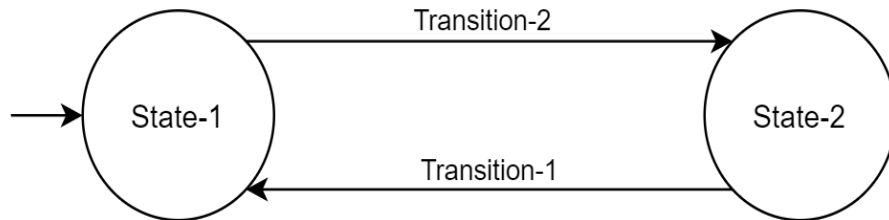


Figure 2-4: State diagram of FSM.

The FSM can be formulated using five tuples $(\Sigma, S, S_0, \delta, F)$, where Σ is a set of finite input symbols, S is a finite set of states, S_0 is the initial state, δ is the transition function from $S \times \Sigma \rightarrow S$, and F is the set of final states [32], [33].

For illustration, the example shown in Figure 2-4 can be demonstrated using five tuples as below:

Σ : {Transition-2, Transition-1}.

S : {State-1, State-2}.

S_0 : State-1.

δ : can be represented using a table that maps the inputs and states as shown in Table 2-1.

F : empty.

Table 2-1: Transition function state.

×	Transition-1	Transition-2
State-1	----	State-2
State-2	State-1	----

Microgrid controllers are typically implemented on Programmable Logic Controllers (PLCs) with adequate capability of communicating with DERs, Circuit breakers, and other devices. A PLC needs to be programmed to represent the microgrid controller. There are many programming languages available for programming PLCs such as ladder logic, continuous flow chart, and structured text. Among them, Structured Text (ST) language provided in IEC 61131-3 standard is one of the most flexible and vendor independent approaches, and therefore adapted in this thesis to program the PLC representing the MGCC.

2.4 Microgrid Control System Testing

To analyze and validate the performance of the deployed strategy in a microgrid controller and evaluate the benefits of the developed control system, the development of testing procedures that accurately evaluate the microgrid control system performance is needed. IEEE 2030.8-2018 outlines specific tests to evaluate the various functions of a microgrid control system [13].

2.4.1 Core Level Functions Testing

The conceptual testing framework proposed in IEEE 2030.8-2018 for dispatch and transition functions is as follows [13]:

- 1) Develop a specific microgrid environment that contains the combination of different DERs and elements applicable for testing a microgrid control system.
- 2) Design several testing scenarios and events to evaluate the core level functions by testing a single function at a time or testing both dispatch and transition functions at the same time, in which the dispatch function commands the transition functions to take the necessary actions to achieve a smooth transition.

2.4.1.1 Transition Function Testing

For transition function testing, a transition scenario is initiated to close or open the breaker at the POI. Transition scenarios are planned islanding, reconnection and unplanned islanding. For planned islanding, based on the command coming from the grid operator, the dispatch function dispatches microgrid assets to adjust the power flow at POI near zero. A disconnection order is then sent to the POI breaker. Reconnection transition results from an order command sent to the microgrid controller. The microgrid control system subsequently synchronizes the microgrid side voltages with grid side voltage. A closing command is then sent to the POI breaker. Unplanned islanding is caused by a fault on the main grid side leading to POI breaker tripping, which is followed by emergency dispatch execution. Tables 3, 4, and 5 in the IEEE 2030.8-2018 provide comprehensive requirements for transition function testing [13].

2.4.1.2 Dispatch Function Testing

Dispatch function testing includes a set of testing scenarios in steady-state conditions under both grid-connected and islanded modes to meet POI interconnection requirements. Tables 1, and 2 in the IEEE 2030.8-2018 detail the requirements for dispatch function testing [13].

2.4.2 Test Metrics

In the testing process, the following metrics should be considered [13]:

- Voltage and frequency transient response of the microgrid. The permissible operating ranges of voltage and frequency are set by the jurisdiction grid code or the interconnection agreement.
- Quality of active and reactive power during transitions and steady-state conditions are within predefined limits specified by the interconnection agreement.

2.5 Operating Modes of Power Converters in Microgrids

The microgrid DERs are usually renewable energy resources or storage units interfaced through VSCs, which has a distinct steady-state and dynamic behaviour [3], [34]. Therefore, several control schemes for converters interfacing DERs can be found in the literature. They are categorized into three groups based on their mode of operation in an AC microgrid following [3], [23], [34], [35]:

- Grid-following inverters
- Grid-forming inverters
- Grid-supporting inverters

2.5.1 Grid-following Inverters

These types of converters are usually associated with non-dispatchable DGs such as wind and PV. Such inverters utilize a Phase-locked Loop (PLL) to track the phase and frequency of the grid voltage waveforms at POI for injecting the correct amount of active and reactive powers. Therefore, the presence of at least one conventional DG or utility grid is required to regulate the voltage and frequency at the POI [3], [36]. An ideal current source in parallel with a high impedance (Z) can be used as a representation for grid-following inverters, exchanging active and reactive power under PQ control mode. It injects constant active and reactive power referenced by the PMS in both grid-connected and isolated modes. Furthermore, these inverters are governed by a current control mode strategy implemented in “dq0” frame not only to achieve a decoupled control behaviour for active and reactive power but also to provide overcurrent protection for the converters against faults, as the output current of the converter is inherently limited [3]. However, injecting a pre-set active and reactive power by a converter makes the power system more susceptible to instabilities, especially when connected in parallel with grid-following converters without a proper management system [23], [35]. Figure 2-5 shows a simplified representation of a grid following inverter, where P^* , Q^* are the active and reactive power setpoints, I^* is the current reference, and C_I is the current controller.

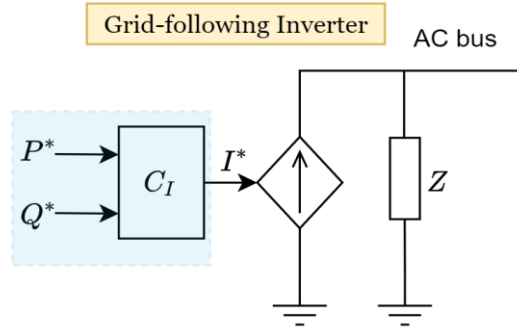


Figure 2-5: Grid-following inverter equivalent representation [36].

2.5.2 Grid-forming Inverters

Grid forming strategy is usually assigned to a fast-acting energy storage, such as batteries. In islanded microgrids, these power inverters are responsible for forming the voltage and frequency of the microgrid to be used as a reference by grid-following converters. A sufficiently large resource with adequate reserve connected to a grid-forming inverter is required for stable operation with the objective to operate as a power balancing slack bus. When connected to a stiff and robust grid, they regulate power and reactive power injected into the AC bus and improve power quality [3], [23]. In islanded mode, their operation can be realized by a voltage control mode equipped with a fast islanding detection algorithm to switch between current control mode and voltage control mode upon islanding [34]. When two or more grid-forming inverters are connected in parallel, a load-sharing strategy between DERs is required. Load sharing is typically governed under a droop control strategy [37]. An ideal voltage source connected in series with a low impedance (Z) can be used as a simple schematic for grid-forming converters as depicted in Figure 2-6, where ω^* , E^* are the frequency and voltage amplitude setpoints, respectively, V^* is the voltage reference, and C_V is the voltage controller.

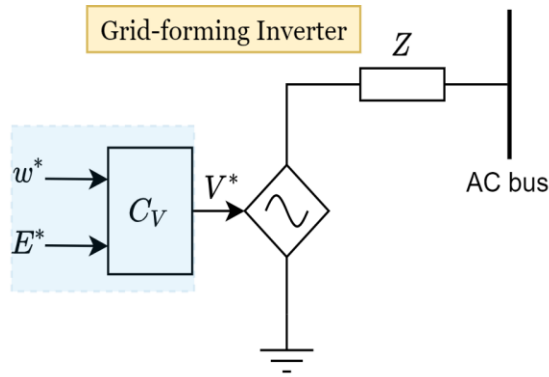


Figure 2-6: Grid-forming inverter representation [36].

The main difference between grid-following and grid-forming inverters is operational. Grid-forming inverters take ω^* and E^* as reference inputs, and regulate the voltage and frequency at the POI at the reference while regulating its output current to facilitate voltage source like operation [36]. On the other hand, grid-following inverter control structure takes P^* and Q^* as reference inputs, and delivers the specified active and reactive power to an energized grid by appropriately controlling the magnitude and phase of the current supplied to the grid [36]. Note that, grid-following inverters may contribute into regulating the network voltage and frequency by adjusting P^* and Q^* settings but can not solely control the voltage and frequency [36].

In the literature, there are two main possible control strategies for grid-forming power converters in islanded microgrids [38]:

- Single master operation.
- Multi-master operation.

2.5.2.1 Single master operation:

In this strategy, a single DG operates as a master unit while other DGs operate as slave units. The master unit regulates the voltage and frequency in the microgrid while the slave units are operated in PQ control mode. The slave units receive their corresponding power sets from the PMS implemented inside the MGCC, whereas the master unit receives voltage amplitude and frequency references as shown in Figure 2-7 [38].

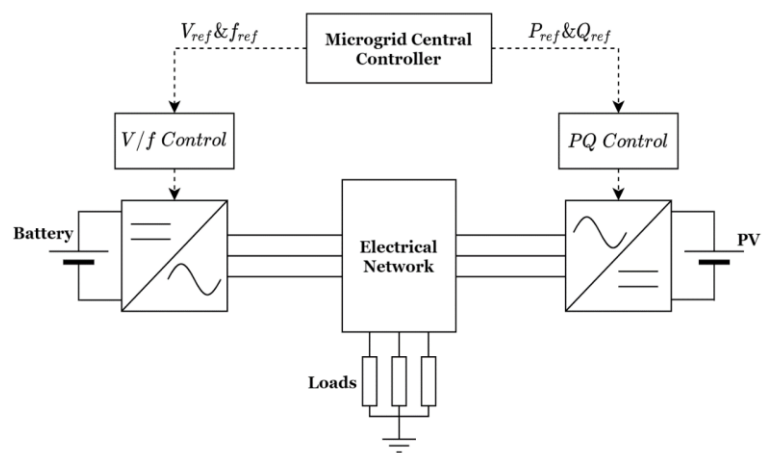


Figure 2-7: Single master operation schematic in islanded microgrid [38].

2.5.2.2 Multi-master operation:

In this strategy, more than one DG behave as masters by adopting V/f control mode. The parallel operation of master units can be realized using a droop strategy to achieve load sharing. For this strategy, the MGCC (PMS) is responsible for defining power setpoints for slave units operating in PQ control mode and activating droop settings for master units. Figure 2-8 shows a general schematic for multi-master operation in an islanded microgrid [38].

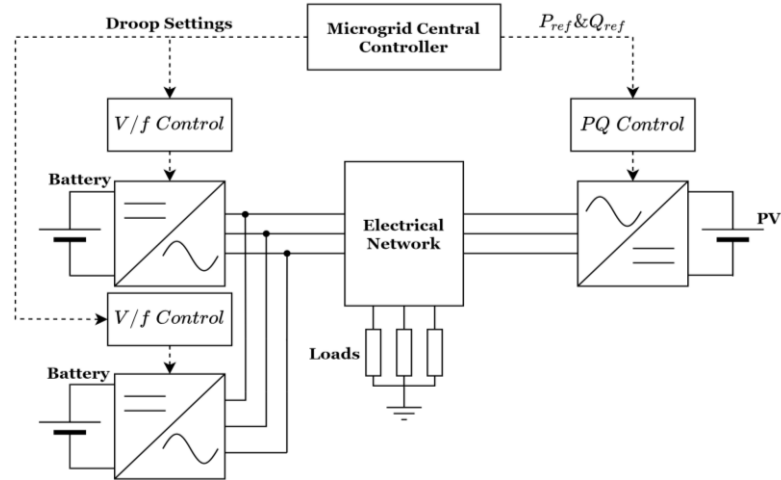


Figure 2-8: Multi-master operation schematic in islanded microgrid [38].

2.5.3 Grid-supporting Inverters

Sometimes another dispatchable DG with grid forming capability is additionally needed to support other inverters in the grid forming task. Such inverters are termed as grid-supporting inverters [23]. Two control modes can be found within grid supporting inverters, which are equivalent to a controlled voltage source or a current-controlled source [39]. In grid-connected conditions, the main objectives of supporting inverters is to supply the load and support voltage and frequency regulation, which improves the power quality and voltage profile of the microgrid [36]. When disconnected from the main grid, these take over the grid forming task along with other grid-forming inverters. Their operation can be realized by a droop strategy. Figure 2-9 shows a simple representation of a voltage-controlled grid supporting inverter, where P , Q are the measured active and reactive power, ω^* , E^* are the frequency and voltage amplitude nominal values, respectively, C_P , C_Q are the droop characteristic coefficients, ω_{ref} , E_{ref} are the frequency and voltage amplitude settings, C_V is the voltage controller, and V^* is the voltage reference.

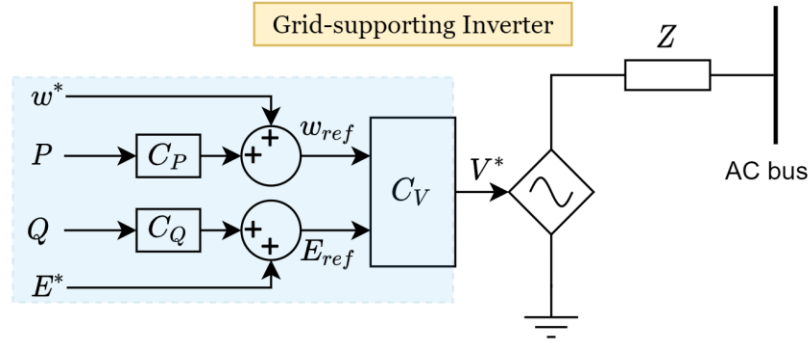


Figure 2-9: Grid-supporting inverter representation [36].

Grid-forming power converters are considered inertia-less inverters, which makes the power system more prone to instabilities. Hence, many researchers worked toward simulating the inertia within the power converter control mechanism to produce the behaviour of a synchronous generator in order to address this issue, leading to the concept of a Virtual Synchronous Generator (VSG) [40], [41]. However, VSG is out of the scope for this thesis.

2.6 Previous Work on Microgrid Controls

One of the main objectives of this research is to develop a PMS for a remote microgrid, containing the core level functions, namely dispatch and transition functions. In the literature search, many power management strategies for standalone systems have been proposed.

In [42], a power management approach for a hybrid PV-Wind-Battery standalone system interfaced through a single-phase inverter is introduced to provide a stable operation under various load and generation conditions. Reference [43], proposed a hierarchical controller to achieve parallel operation for PV-Battery-Hydropower hybrid system. The hydropower acts as a slack bus, whereas the PV-Battery inverter operates in PQ control mode to inject

the required active and reactive power. A centralized microgrid controller for a hybrid PV-Battery system to balance the power flow between the DC and AC loads under different operating conditions and switch smoothly between grid-connected and islanded modes was proposed in [44]. Reference [45] provides a comparative analysis for three different PMS strategies along with different sizing approaches for a DC microgrid in order to find the most efficient sizing for the PMS methods. The authors in [46] introduced a PMS for an islanded microgrid with PV and Hybrid Energy Storage System (HESS) containing a battery and Super Capacitor (SC). The proposed method maintains the SOC of HESS within acceptable limits by limiting PV generation or load shedding. In addition, a virtual impedance is introduced in order to share the load efficiently between HESS resources, where the battery is responsible for supplying steady-state power and the SC provides transient power variations.

The microgrid control can be decentralized through DERs local controls to avoid extensive communication. In [47], a decentralized PMS system is proposed for an islanded microgrid consisting of PV, battery, and hybrid PV-Battery units. A droop strategy taking into account the PV power generation and battery state of charge when sharing the load among the resources is presented. Furthermore, to cover all possible operating events, five distinct different operating modes are developed. In [48], hybrid PV-Battery systems participate in load sharing by deploying an adaptive droop control. The proposed technique maximizes the output power of PV while following load changes and charging the battery with surplus power. Furthermore, if the battery is fully charged, the PV alters its operating point to track the load autonomously by modifying the droop settings.

An event-driven state machine is presented in [49] for isolated DC microgrid consisting of PV, battery, and wind units, in which the battery SOC is used to switch between four different machine states. Similarly [50], [51] discussed a supervisory control layer for a microgrid modelled using FSM computational model. The operation of each unit is divided into distinct modes according to the microgrid conditions. Reference [52], proposed an application of hybrid Petri nets to model and analyze microgrid systems.

Chapter 3

System Configuration, Model and Control

3.1 Introduction

This chapter introduces the modelling of DERs in the considered microgrid study system, including a PV unit, diesel plant and a BESS. This chapter also discusses their associated control systems for both generator support and islanded modes.

3.2 System Description

The microgrid considered for the test system was modeled based on an actual power system in a Northern-Canadian remote off-grid community [4]. The structure of the test grid shown in Figure 3-1 can be described as a PV system connected in parallel with BESS and a diesel plant. The system consists of a 1.2 MW diesel plant, a Li-ion BEES with a DC rating of 600 kW-912 kWh, a 616 kW PV array, and a set of balanced loads. The sizes of the PV system and the BEES have been optimally selected considering the prevailing weather and load patterns, as a retrofit to the original diesel only power system. The diesel plant contains two diesel generators; DIS-1 with a rating of 400 kW and DIS-2 with 800 kW capacity. The PV unit is interfaced to its VSC through a boost converter controlled to facilitate different control modes. The BESS is linked to its VSC using a bidirectional buck/boost converter to regulate the VSC DC-bus voltage and supervise charging/discharging modes. The PV system and the BESS both employ VSCs rated at 0.6 MVA for energy transfer

between the DC and AC sides. The VSCs are controlled using the carrier-based Pulse Width Modulation (PWM) principle. An LCL filter is connected at the output of each VSC to reduce the AC harmonics levels generated by power converters. A simplified representation is used for the 25 kV radial distribution system, and the loads of each category are lumped to reduce the complexity.

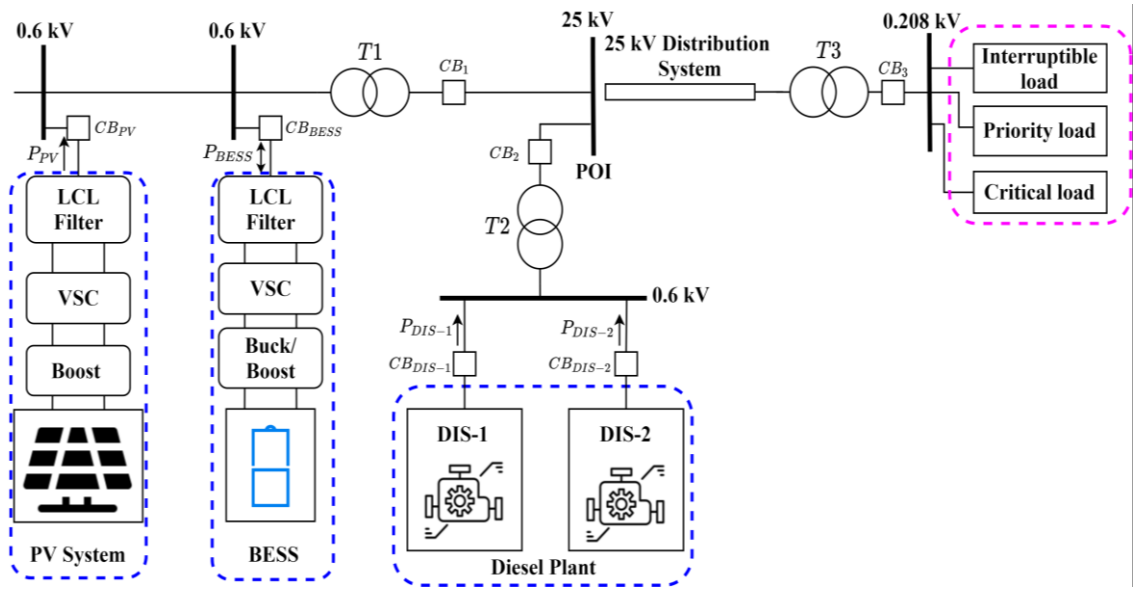


Figure 3-1: Microgrid test system.

The microgrid is supposed to operate in both generator support (GENSUP) and islanded modes based on the status of the breakers CB_{DIS1} and CB_{DIS2} . If at least one of the diesel generators is enabled, the system is considered as operating in the “GENSUP” mode, whereas “islanded” mode is marked by the absence of diesel generators.

The considered system was modelled inside RTDS® digital real-time simulator environment. As the test system is simulated in real-time, Average Value Models (AVMs) were used to represent the power converters to mitigate the required computational resources [53]. This is not a major drawback as the main focus is the low-frequency

dynamic behaviour of the system. Use of DRTS makes it possible to easily modify or expand the microgrid configuration in the test setup for testing various operational scenarios with no added costs.

3.3 Diesel Plant

Diesel generators are commonly used as backup power sources to supply power during power outages or to electrify off-grid remote communities. Diesel generators have the capability to provide ancillary services such as voltage and frequency control [54]. In this research, diesel generators are used in a remote microgrid as grid forming DGs to regulate the voltage and frequency as well as to supply the load. Each diesel generator is modelled as a synchronous generator along with an excitation system, and a diesel engine regulated by a speed governor as shown in Figure 3-2 [55]. The input to the speed governor is the speed reference (w_{ref}) and the measured speed (w_{DIS-n}), and it adjusts the diesel engine valve position to produce a torque that drives the shaft of the synchronous generator. The excitation system is responsible for maintaining the generator terminal voltage (V_{DIS-n}) at a referenced value (V_{ref}) by providing the DC field current (I_{Filed}^{DC}) to the generator rotor windings. The excitation system was modelled using ST5B excitation system model available in RTDS model library. The diesel generator model developed in [55] was used in this thesis.

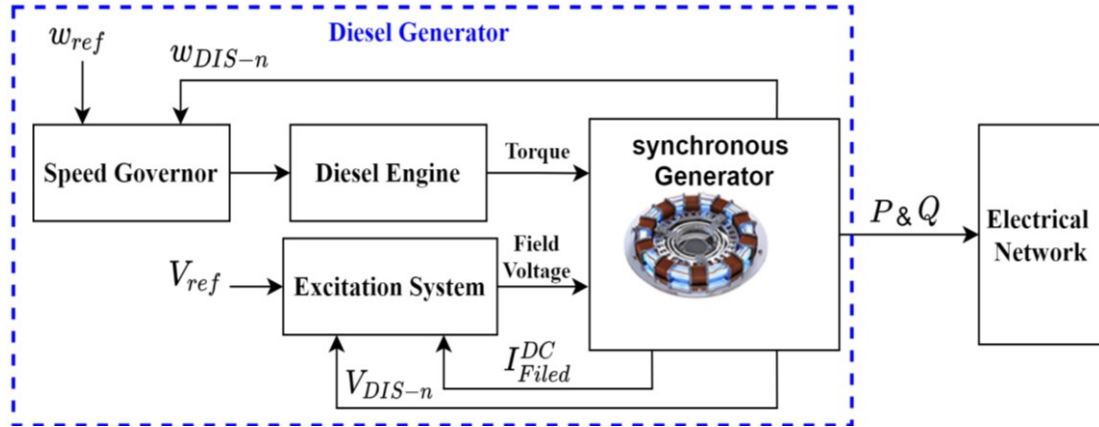


Figure 3-2: Diesel generator model schematic [55].

When both diesel generators are running, a droop control strategy governs the operation of diesel plant to achieve load sharing. However, deploying the droop strategy causes a steady-state deviation in the voltage and frequency, so secondary controllers are used to slowly restore the nominal voltage and frequency of the microgrid. Isochronous mode governs the operation if only one generator is connected, which maintains a fixed voltage and frequency for different load conditions [56], [57]. Next subsections discuss the reference generation for the excitation and speed governor systems operating in both droop and isochronous modes.

3.3.1 Speed Reference Generator

As depicted in Figure 3-3, the speed reference signal (w_{ref}) comprises three components, which are the droop adjustment (w_{droop}), nominal speed (w_n), and the speed secondary adjustment (w_{sec}). The contribution from w_{droop} becomes non-zero only when the both diesel generators are connected (Droop-ON = 1) to share the load between diesel generators, whereas isochronous mode administers the diesel plant operation only if one diesel generator is connected, maintaining constant voltage and frequency. The main tasks

of w_{sec} are to adjust the speed of the diesel generator to synchronize its frequency and phase with the grid when a reconnection command is received and to correct the diesel generator speed to bring the microgrid frequency to the nominal value when operating in droop control mode.

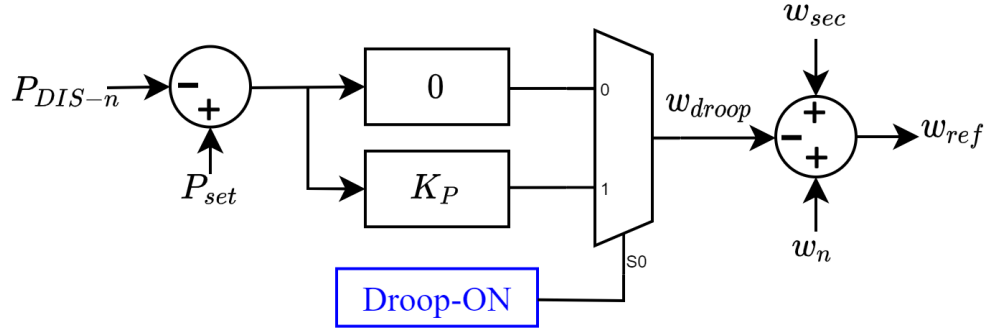


Figure 3-3: Schematic of speed reference (w_{ref}) generator.

The associated droop coefficient (K_P) can be defined using (3.1), which describes the relationship between the output power of the diesel generator and its speed, Where w_{NL} is the no-load speed, and w_{FL} is the full load speed as shown in Figure 3-4 [56], [57].

$$K_P = \frac{w_{FL} - w_{NL}}{w_{NL}} \quad (3.1)$$

For conventional DGs, the $P - w$ droop curve illustrated in Figure 3-4 can be mathematically expressed as in (3.2) [56], [57], where P_{set} is the power reference and P_{DIS-n} is the measured output active power of the diesel generator.

$$w = w_n - K_P(P_{set} - P_{DIS-n}) \quad (3.2)$$

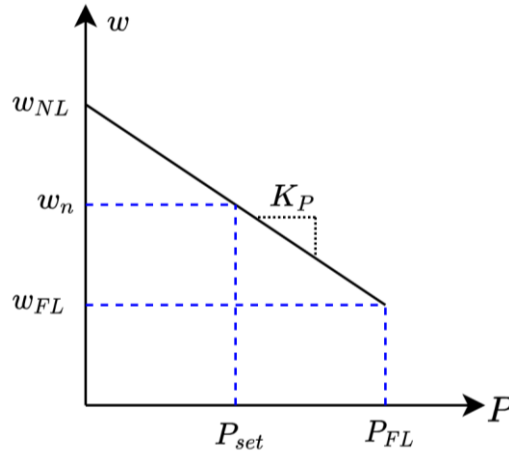


Figure 3-4: $P - w$ (active power – speed) droop curve.

The w_{sec} consists of phase synchronization, and secondary frequency control loops as described in Figure 3-5. The phase synchronization scheme is enabled once the diesel generator receives a reconnection signal ($\text{Synch}^{\text{PMS}} = 1$) from the PMS and is responsible for synchronizing the phase angle of diesel generator terminal voltage (V_{DIS-n}) with the phase angle of the microgrid voltage at the POI (V_{POI}). The phase angles of V_{DIS-n} and V_{POI} are extracted by PLLs and compared to generate an error signal. The error signal is then fed to a PI controller to generate the required synchronization secondary reference (w_{Synch}). On the other hand, speed regulation control is enabled when both diesel generators are connected ($\text{Droop-ON} = 1$) to restore the nominal speed of the diesel generator.

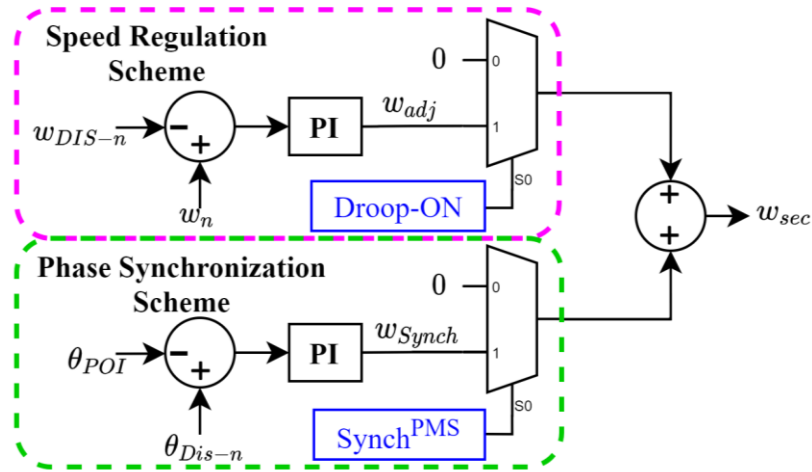


Figure 3-5: Speed reference secondary controllers.

Before disconnecting a diesel generator, the line current of the unit should be reduced to near zero for smooth disconnection. Hence, the P_{Set} will be derived as described in Figure 3-6 to unload the unit, when a disconnection command is received from the PMS ($Disc^{PMS} = 1$).

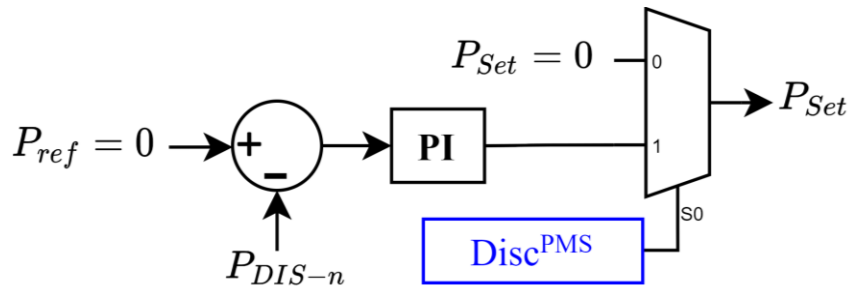


Figure 3-6: Active power reference generator.

3.3.2 Voltage Reference Generator

Similarly, the voltage setting for the excitation system illustrated in Figure 3-7 consists of a droop adjustment (V_{droop}), secondary control (V_{sec}), and the nominal voltage (V_n). V_{sec} consists of two secondary functions, which are the voltage regulation and synchronization control loops.

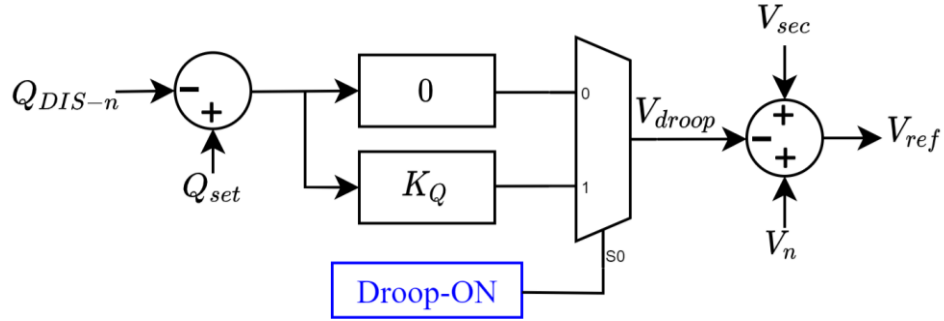


Figure 3-7: Schematic of voltage reference generator.

For conventional DGs, the $Q - V$ droop curve depicted in Figure 3-8 is adopted and can be mathematically expressed as in (3.3) [56], [57], where Q_{set} is the reactive power reference, and Q_{DIS-n} is the measured output reactive power of the diesel generator.

$$V = V_n - K_Q(Q_{set} - Q_{DIS-n}) \quad (3.3)$$

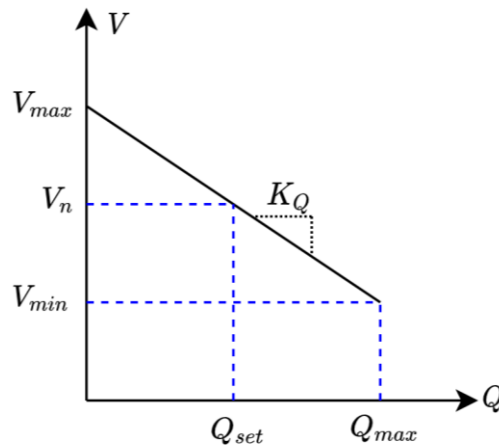


Figure 3-8: $Q - V$ (reactive power – voltage) droop curve.

Figure 3-9 shows the secondary control loops of the excitation system, in which the voltage regulation scheme reduces the steady-state voltage deviation caused by the droop control to zero. Also, the voltage synchronization scheme minimizes the voltage difference across the circuit breaker when $\text{Synch}^{\text{PMS}}$ is acknowledged to facilitate a smooth reconnection.

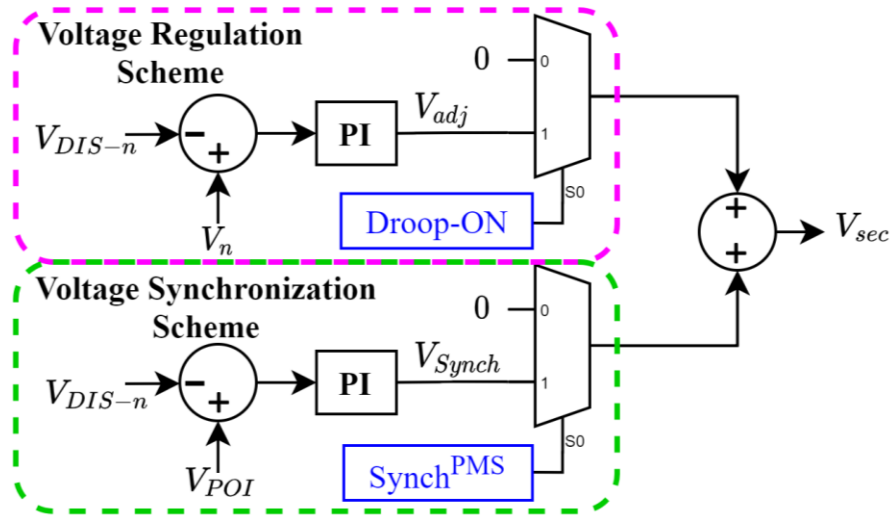


Figure 3-9: Voltage reference secondary controllers.

When a disconnecting request is received ($Disc^{PMS} = 1$), an unloading control scheme is implemented to derive Q_{Set} as depicted in Figure 3-10.

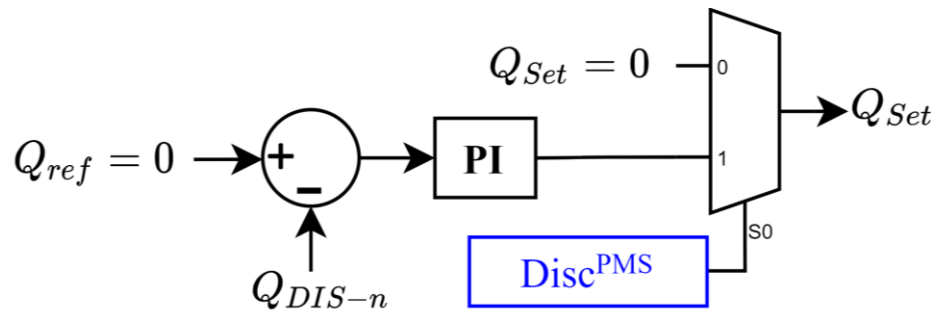


Figure 3-10: Reactive power set generator.

3.4 Photovoltaic System

Figure 3-11 shows a schematic diagram of the PV system. The PV system is rated at 600 kW and consists of a solar array, boost converter, VSC, and an LCL filter. The next subsections describe the modelling and control of the PV system.

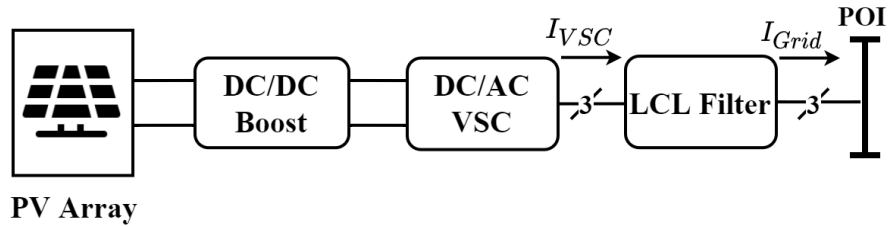


Figure 3-11: Schematic of the PV system.

3.4.1 PV Array Model

The fundamental element of a PV array is the solar cell. Solar cells are made of semiconductor materials that generate electric energy when exposed to sunlight. A PV module is defined as a combination of solar cells connected in series and/or parallel in order to obtain larger voltage and current from the PV module for practical applications. A typical PV module consists of N_{cp} number of parallel connected strings with each string consisting of N_c number of solar cells connected in series. The PV array contains many interconnected modules in series (N_s) and/or parallel (N_p). Figure 3-12 shows the RTDS®/Rscad PV array model.

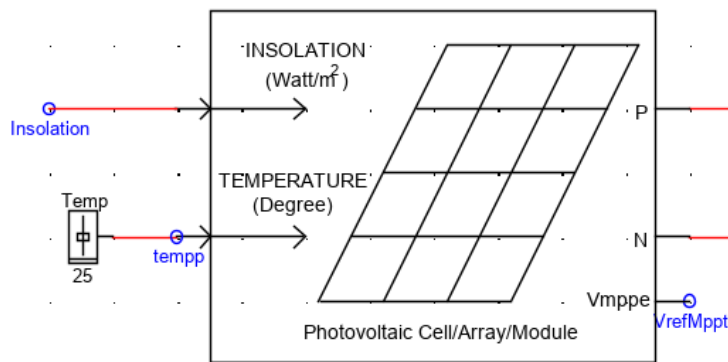


Figure 3-12: RTDS PV array model.

An ideal current source in parallel with a real diode can represent an ideal solar cell with non-linear characteristics between the voltage (V) and current (I). However, a realistic solar cell model need adding a series (R_S) and a shunt (R_{Sh}) resistances [58], [59] as shown in Figure 3-13.

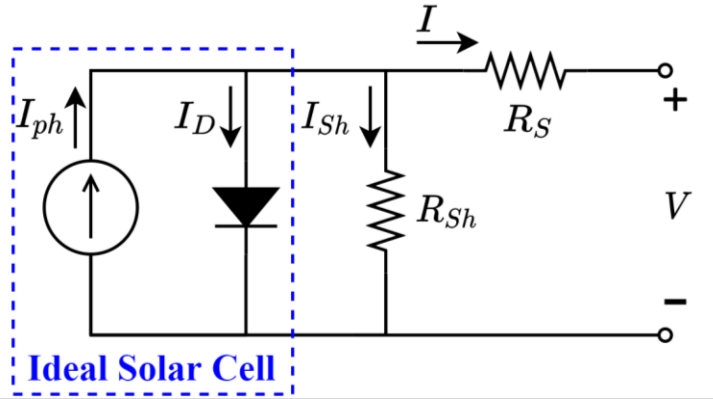


Figure 3-13: Solar cell model.

The solar cell output current can be given as in (3.4) [58], [59].

$$I = I_{ph} - I_D - I_{Sh} \quad (3.4)$$

where I_{ph} is the photocurrent induced by the incident sunlight on the solar panel, I_D is the diode current that forms the nonlinear $I - V$ relationship, and I_{Sh} is shunt resistor current.

The terms I_D and I_{Sh} can be expressed as in (3.5) and (3.6) [58], [59].

$$I_D = I_o \left(e^{\frac{q(V+IR_S)}{nKT}} - 1 \right) \quad (3.5)$$

$$I_{Sh} = \frac{V + IR_S}{R_{Sh}} \quad (3.6)$$

where k is the Boltzmann Constant ($1.3806503 \times 10^{-23}$ J/K), and q is the magnitude of an electron charge (1.602176×10^{-19} C), T is the PV cell temperature in Kelvin, and n is the diode ideality constant. A substitution of I_D and I_{Sh} in (3.4) yields [58], [59]:

$$I = I_{ph} - I_o \left(e^{\frac{q(V+IR_S)}{nKT}} - 1 \right) - \left(\frac{V + IR_S}{R_{Sh}} \right) \quad (3.7)$$

I_{ph} and I_o at any given irradiance G (W/m^2) and temperature (T) in Kelvin can be expressed using (3.8) and (3.9) [58].

$$I_{ph} = I_{ph_{stc}} \left(\frac{G}{G_{stc}} \right) (1 + k_i(T - T_{stc})) \quad (3.8)$$

$$I_o = I_{o_{stc}} \left(\frac{T}{T_{stc}} \right)^3 e^{\left(\frac{qE_g}{nK} \left(\frac{1}{T_{stc}} - \frac{1}{T} \right) \right)} \quad (3.9)$$

where $I_{ph_{stc}}$ is the induced photocurrent at the standard irradiation ($G_{stc} = 1000 \text{ W}/\text{m}^2$) and the standard temperature ($T_{stc} = 25^\circ$), E_g is the bandgap energy of the semiconductor material and k_i is the temperature coefficient of photocurrent [58]. All the constant parameters in the above can be obtained by examining the manufacture's PV module I-V curves, which are usually stated in the PV datasheet at the standard conditions ($G_{stc} = 1000 \text{ W}/\text{m}^2$, $T_{stc} = 25^\circ$). The RSCAD PV model incorporates two distinct methods for cell parameters estimation for the PV array, which are specified as analytical and iterative methods [60].

As depicted in Figure 3-14, the $I - V$ relationship represents various operating points of the PV array depending on the insolation G and T . The knee point is defined as the

Maximum Power Point (MPP) where the PV array outputs the maximum electric power for a given T and G . In this thesis, the PV array model parameters are obtained from ALL-BLACK CS6K-M PV module datasheet.

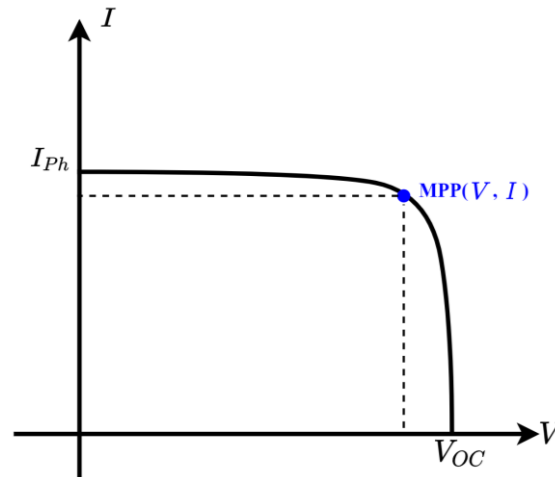


Figure 3-14: Typical I-V characteristics for a solar cell.

3.4.2 Average Value Models (AVMs) of Power Converters

The essence of the average simulation of PWM converters is the substitution of switching components by dependent voltage and current sources to obtain a time-invariant circuit topology. Detailed switched PWM converter models offer detailed dynamic models but require simulating the systems at very small-time steps, which requires more computational resources which are scarce, especially in real-time simulation applications. Therefore, to reduce the required processing power, PWM converters were modelled using AVMs as the main concern is the dynamics that exhibit low frequency attributes. The kind of analysis required in the test application is the decisive factor that determines to whether use detailed switching models. Such detailed models of PWM converters are required for harmonics and dynamic overvoltage studies, which is not the main concern in this thesis [16].

3.4.2.1 Voltage Source Converter Average Model

Figure 3-15 shows the AVM of a VSC. The average of a single waveform over a switching cycle (T_s) can be calculated using (3.10), where $\bar{x}(t)$ is the averaged waveform of $x(t)$.

$$\bar{x}(t) = \frac{1}{T_s} \int_0^{T_s} x(\tau) \cdot d\tau \quad (3.10)$$

The AC side voltage of a VSC can be defined as in (3.11), where V_{DC} is the voltage of the DC-link capacitor.

$$V_{a,b,c} = m_{a,b,c} \frac{V_{DC}}{2} \quad (3.11)$$

Substitution of (3.11) in (3.10) yields:

$$\bar{V}_{a,b,c} = \bar{m}_{a,b,c} \frac{V_{DC}}{2} \quad (3.12)$$

where $\bar{m}_{a,b,c}$ is the averaged modulation indices for three phase sinusoidal voltage waveforms used to generate PWM firing signals for VSC switches, and $\bar{V}_{a,b,c}$ is the averaged AC side voltages. Considering a lossless converter, the power balance technique can be used to calculate the DC side current [2], [4] as in (3.13) to (3.15).

$$P_{DC} = P_{AC} \quad (3.13)$$

$$V_{DC} I_{DC} = V_a I_a + V_b I_b + V_c I_c \quad (3.14)$$

$$I_{DC} = \frac{V_a I_a + V_b I_b + V_c I_c}{V_{DC}} \quad (3.15)$$

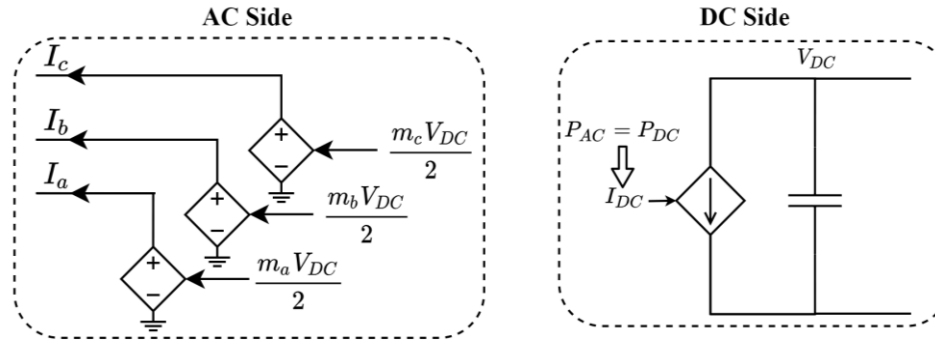


Figure 3-15: AVM of VSC.

3.4.2.2 Boost Converter Average Model

Figure 3-16 shows an ideal boost converter, which will be represented as an AVM. The switching mechanism and ripples will be neglected, only necessary DC and low frequency AC waveforms are modelled. The dependent voltage and current sources can equivalently represent the switching behavior of the DC-DC converters [61], [62]. Deriving the average model for the considered boost converter requires defining the state space s for the inductor (L) and capacitor (C) over the period T_s of the switching signal (g_1) as depicted in Figure 3-17.

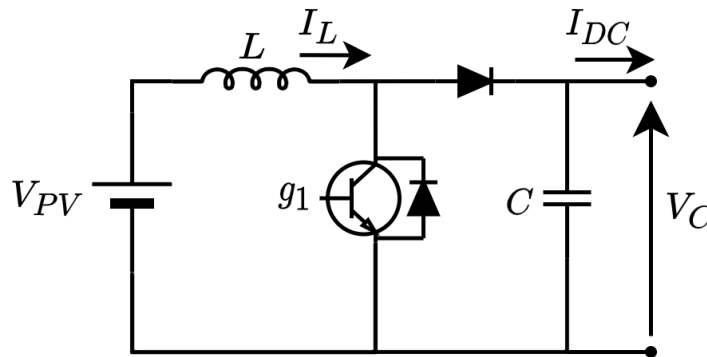


Figure 3-16: Boost converter.

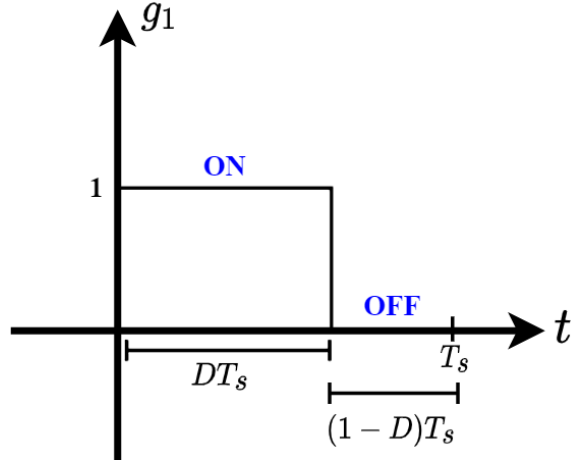


Figure 3-17: one cycle of the switching input (g_1).

For switch ON state, the state space equations can be represented as in (3.16) and (3.17).

$$\frac{dI_L}{dt} = \frac{1}{L} V_{PV} \tag{3.16}$$

$$\frac{dV_C}{dt} = \frac{-I_{DC}}{C} \tag{3.17}$$

For switch OFF state, the L and C differential equations can be given as in (3.18) and (3.19), respectively.

$$\frac{dI_L}{dt} = \frac{1}{L} (V_{PV} - V_C(t)) \tag{3.18}$$

$$\frac{dV_C}{dt} = \frac{I_L(t) - I_{DC}}{C} \tag{3.19}$$

By knowing that $i_L(t), V_C(t)$ are very slow variables and assuming constant input voltage (V_{PV}), the state S for ON and OFF states, can be combined and averaged over a T_s . Below are the averaged state space equations for the boost converter over T_s .

$$\frac{d\bar{I}_L}{dt} = \frac{1}{L}(V_{PV} - V_C(1 - D)) \quad (3.20)$$

$$\frac{d\bar{V}_C}{dt} = \frac{I_L(1 - D) - I_{DC}}{C} \quad (3.21)$$

From (3.20) and (3.21), the AVM for an ideal boost converter can be constructed as depicted in Figure 3-18.

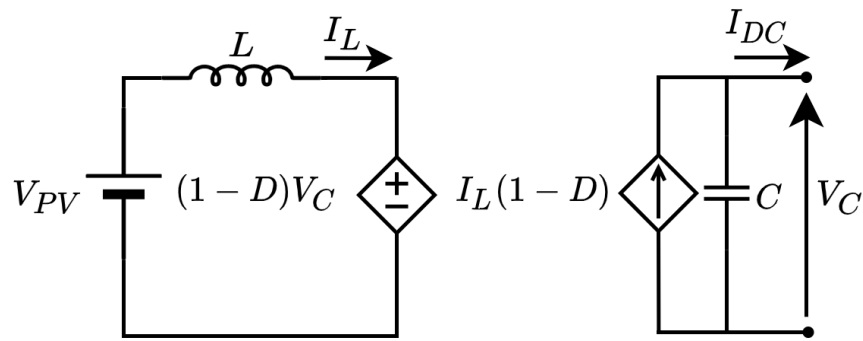


Figure 3-18: AVM of a Boost DC/DC converter.

3.4.3 PV System Control Strategy

Figure 3-19 shows the control strategy of the PV-VSC. It consists of a grid-following mode, and droop control associated with grid-forming mode. Regardless of the diesel plant operation mode, the PV unit operates in grid-following mode. However, BESS failure in maintaining the microgrid voltage and frequency in islanded mode triggers the grid-forming control of the PV system (VSC-Droop = 1). The next subsections detail the PV system controllers.

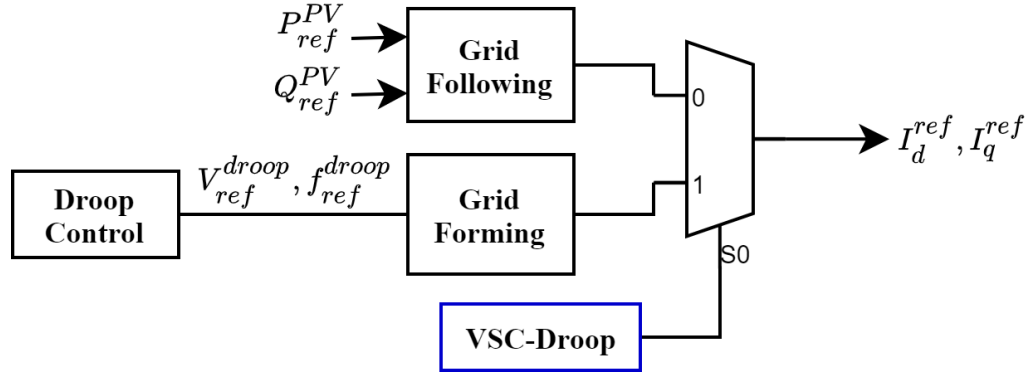


Figure 3-19: PV system control structure.

3.4.3.1 VSC Current Controller

As shown in Figure 3-20, a three-phase current feed-forward control strategy in the d-q rotating frame was adopted to govern the VSCs [13]. The three-phase current and voltage quantities were transformed into DC quantities in the d-q frame by the means of Park transformation. The d-q axis current components (i_d^{VSC}, i_q^{VSC}) were independently regulated with its respective reference commands (i_d^{Ref}, i_q^{Ref}) by deploying ωL_f as a feed-forward term in the control loops, where L_f is the VSC-side filter inductance. Also, V_d and V_q denote the d-q axis components of the voltage at the POI (V^{POI}) [64]. I_d^{Ref} and I_q^{Ref} were derived depending on the adopted operating mode as discussed in subsections 3.4.3.2 and 3.4.3.3 . In steady-state as V_q settles at zero, the PV-VSC output power can be stated as given in (3.22) and (3.23), respectively.

$$P_{VSC} = 1.5V_d I_d \quad (3.22)$$

$$Q_{VSC} = -1.5V_d I_q \quad (3.23)$$

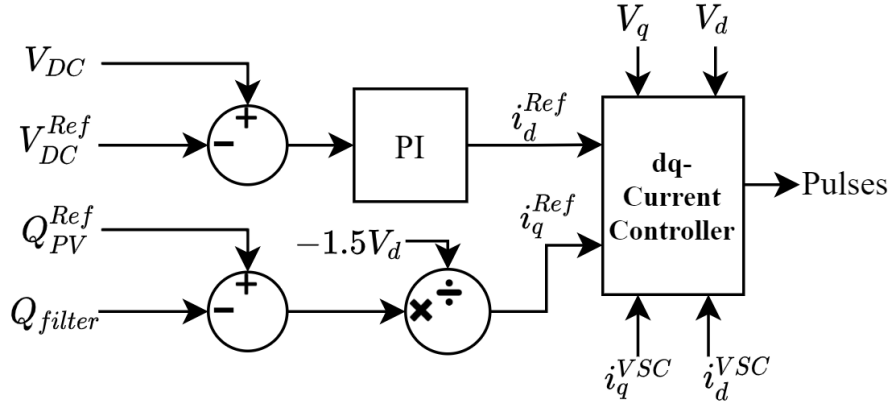


Figure 3-21: PV-VSC power control loop.

3.4.3.3 Grid-forming Mode

The BESS sometimes has a limited amount of energy and might fail to attain the required voltage and frequency assigned by the grid operator (VSC-Droop = 1). So, the capability of operating the PV unit as a grid-supporting inverter [36] can be crucial to maintain stable and reliable operation in such remote areas. Under this strategy, the PV and BESS are assigned to jointly form the grid in a multi-master configuration. The operation of BESS and PV as grid forming sources connected in parallel can be realized by deploying a droop strategy. However, this would impose a constraint on extracting the freely available maximum power of the PV array as the PV-VSC output is driven by AC grid conditions. So, in the long run, it would be inefficient in contrast to the operation discussed in Section 3.4.3.2.

The derivation of inner-current control loop references (I_d^{Ref} , I_q^{Ref}) were modified using two outer-voltage control loops as shown in Figure 3-22, where C_f is the AC side filter capacitance and K_d is the current feed-forward coefficient [66]. In d-q framework, by giving $V_q^{Ref} = 0$, the d-axis is oriented with the voltage vector. So, the regulation of V_d is

adequate in controlling the AC voltage magnitude at the required reference (V_d^{Ref}) [66]. The outer d-q axes voltage control loops to regulate (V_d, V_q) at their corresponding references (V_d^{Ref}, V_q^{Ref}) are shown in Figure 3-22(b) & (c). The incorporation of the feed-forward signals, $C_f w V_q$ and $C_f w V_d$ is expected to reduce the coupling effects on the outer-voltage control [64]. In addition, d-q components of the VSC grid-side current (I_d^{Grid}, I_q^{Grid}) were also incorporated to mitigate the effects of load dynamics on the voltage control task [64].

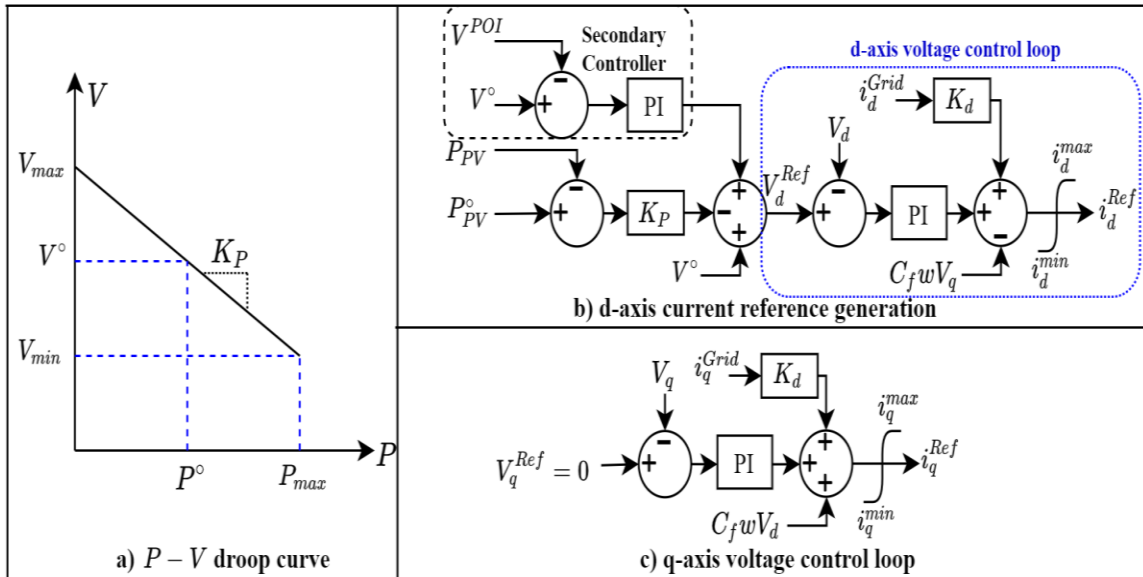


Figure 3-22: PV-VSC voltage control loops.

In remote MV/LV power systems, the grid impedance is mainly resistive. Therefore, in contrast to the $P - f$ and $Q - V$ droop curves used in conventional power systems, $P - V$ and $Q - w$ droop curves were formulated as illustrated in Figure 3-22(a) and Figure 3-23(a) for the PV and BESS operating in grid forming mode. These $P - V$ and $Q - w$ droop curves can be mathematically expressed as in (3.24) and (3.25) [67]:

$$V = V^\circ - K_P(P^\circ - P) \quad (3.24)$$

$$w = w^\circ + K_Q(Q - Q^\circ) \quad (3.25)$$

where V and w represent the voltage and angular frequency outputs of the droop curves, respectively; K_P and K_Q are the real and reactive powers droop coefficients; P° and Q° are the active and reactive power set points and V° and w° are the nominal voltage and frequency values of the grid, respectively. The d-axis voltage reference (V_d^{Ref}) and the frequency reference (w^{Ref}) for the VSC were derived from (3.24) & (3.25), respectively. The droop curves produce a steady-state deviation in the voltage and frequency of the VSC as a function of the real and reactive powers (P, Q) delivered to the grid. Thus, a secondary restoration controller to restore the nominal voltage and frequency of the VSC was implemented.

In islanded mode, the frequency (w^{Ref}) is controlled in an open-loop manner using an oscillator at a fixed frequency (w^{Ref}) [36], [66]. The rated frequency (w°) is provided as a feed-forward term to enhance the dynamic response of the oscillator. Figure 3-22(a) & (b) and Figure 3-23 depict the external droop control loops schemes. Similar outer voltage and droop control loops were implemented in the BESS-VSC during this mode.

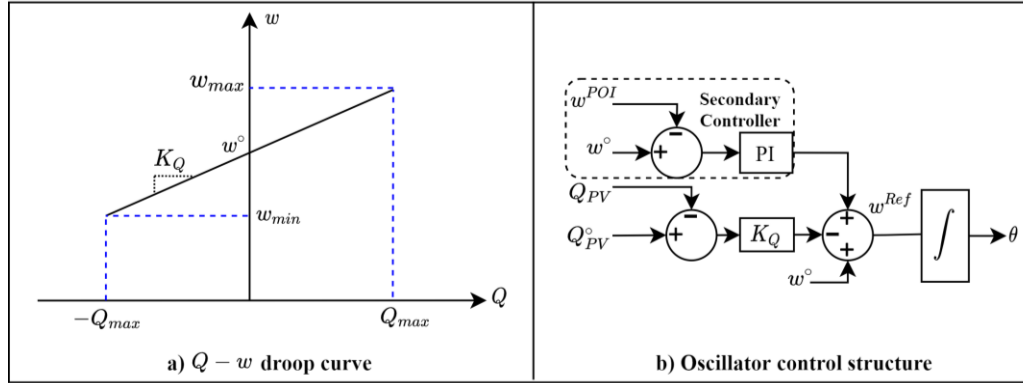


Figure 3-23: Frequency external control loop.

The droop strategy is used to achieve power-sharing between VSCs. However, when a PV-VSC is participating in the droop control, it would be inefficient as the main concern is to harness the available maximum PV power. Also, the stability of the system might get compromised if PV-VSC couldn't satisfy the power requirement assigned by the droop curves. To operate the PV-VSC as a grid-forming source, the PV array should operate at a lower level than its maximum available power, such that the reserved power facilitates forming of the voltage and frequency [68]. To achieve this, an adaptive PV power set point (P_{PV}°) for the $P - V$ droop is introduced. In this scheme, the PV power set point changes continuously to ensure coordinated and effective operation of the PV-VSC along BESS-VSC. Two different modes to derive P_{PV}° were implemented: reserve mode and load-following mode. During reserve mode, the PV unit is pushed to operate near MPP with adequate reserve, which is very crucial for PV grid-forming inverter. This can be obtained by comparing a scaled MPP PV voltage reference (V_{MPPT}) with PV array voltage (V_{PV}) to generate an error signal. The error signal is then passed to a PI controller in order to generate the setpoint P_{PV}° . As it is recommended in reserve mode to operate the PV array at a voltage that is higher than V_{MPPT} [68], the reserve coefficient is set higher than one

($K_{MPPT} > 1$). It is important to note that the scaled MPP voltage reference is limited in order to prevent commanding the PV array to operate at or above the open circuit voltage (V_{oc}^{PV}), which would result in zero PV output power. In load-following mode, this mode is enabled only when both the SOC goes above its maximum value (SOC_{max}) and the PV real power (P_{PV}) is higher than or equal to the measured load power (P_L). Under this mode, P_{PV} is compared with P_L to generate an error signal that is then passed to a PI controller. In the proposed adaptive setpoint, the two modes are switched continuously to provide an effective response for sudden variations in load and solar irradiance. Figure 3-24 shows the control blocks of P_{PV}° generator.

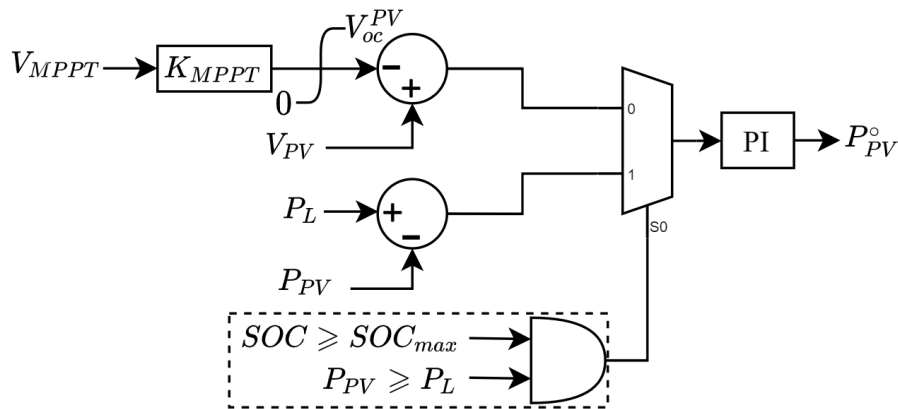


Figure 3-24: PV-VSC power reference generator schematic.

3.4.3.4 PV Array Controller

To extract the freely available maximum power at each operating condition, Maximum Power Point Tracking (MPPT) algorithms were developed in the literature. In this model, a technique called fractional open circuit voltage [69] was used, which gives a voltage reference of the PV array to be tracked by the boost converter in order to utilize the maximum available power. Based on the control strategy used for PV-VSC and BESS SOC, the PV array controlling approach is varied. Three different techniques are devised

namely: MPPT control, limited-power control, and DC-link voltage control. For example, during periods with excess renewable energy, the active power output of the PV unit must be restricted as specified by the PMS usually implemented on the MGCC. The amount of power curtailed will depend on the event that triggered this mode. For the isolated mode of operation, the PV power curtailment is usually triggered by battery overcharge scenarios. If the grid-forming battery unit reaches its overcharge boundary due to a sustained energy surplus period, the supervisory controller initiates the power curtailment mode (Limited-power = 1 and Grid-forming = 0). During this mode, the solar PV array's reference power is determined by the supervisory controller, and the PV voltage will fall between the MPP PV voltage and the open-circuit voltage. In MPPT mode (Limited power = 0 and Grid-forming = 0), the MPPT voltage reference is tracked by the boost converter to harness the maximum available power. In islanded mode (Grid-forming = 1), the boost converter was controlled to maintain the DC-link voltage at its desired reference. Note that, (Limited-power = 1 and Grid-forming = 1) is not an acceptable option. Figure 3-25 demonstrates the control block of the boost converter.

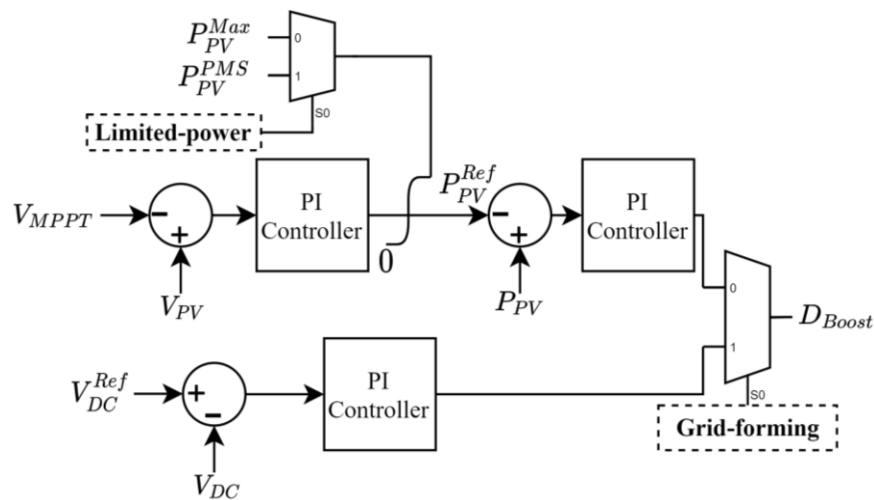


Figure 3-25: PV array controller.

3.5 Battery Energy Storage System

Figure 3-26 shows the schematic diagram of the BESS system. The BESS system is rated at 600 kW and consists of a Li-ion battery array with a DC rating of 600 kW, 912 kWh, buck/boost converter, VSC, and LCL filter. The BESS structure is identical to the PV system except for the buck/boost converter to facilitate bi-directional power flow.

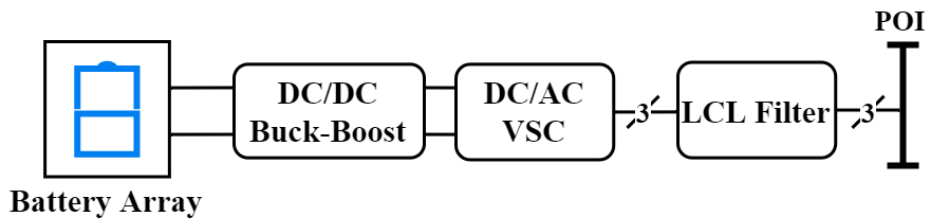


Figure 3-26: BESS system

3.5.1 Battery Array Model

RTDS battery model properties were obtained from a real commercial Li-ion polymer battery product (TCL-PL-383562) from TCL Hyperpower Batteries Inc. Figure 3-27 presents the circuit of the adopted battery array model. This model only focuses on modelling the voltage and current characteristics of the battery and ignores the long-term characteristics, such as self-discharge and thermal dependency. The R_S and C_S represent the behaviour the short-term transient of the model, whereas R_L and C_L models the long-term transients. The battery model parameters (R_S , C_S , R_L , C_L , R_{se} , V_{oc}) are functions of SOC. More Details about the model can be found in [60].

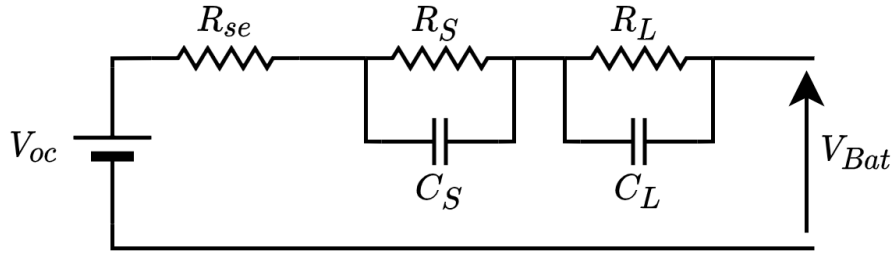


Figure 3-27: Battery model equivalent circuit.

3.5.2 Average Value Models of Power Converters

The VSC AVM detailed in Section 3.4.2.1 was used for the BESS-VSC. Similar derivation as explained in Section 3.4.2.2 was carried out to obtain the AVM for the buck/boost converter shown in Figure 3-28.

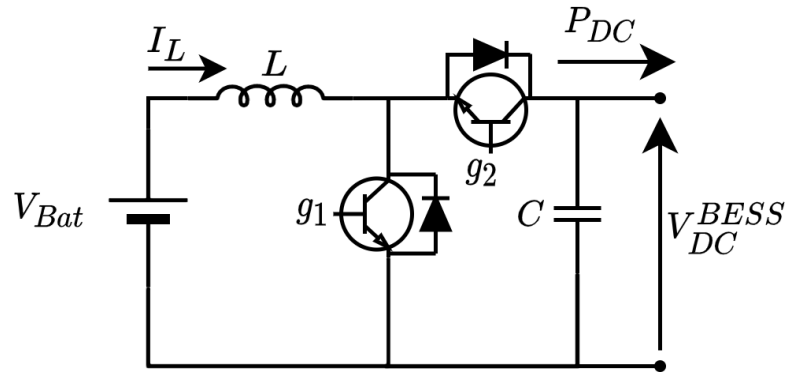


Figure 3-28: Buck/boost converter circuit used in BESS

Figure 3-29 shows the average value model of the buck/boost converter used in BESS.

When the boost converter mode is on (g_1 is active), the battery is discharging, for which V' and I' can be mathematically expressed as in (3.26) and (3.27), where D_{g_1} is the averaged waveform of the switching input (g_1).

$$V' = (1 - D_{g_1})V_{DC} \quad (3.26)$$

$$I' = (1 - D_{g_1})I_L \quad (3.27)$$

On the other hand, V' and I' can be obtained from (3.28) and (3.29) when the buck converter mode is on (g_2 is active), to allow the battery to charge, where D_{g_2} is the averaged waveform of the switching input (g_2).

$$V' = D_{g_2} V_{DC} \quad (3.28)$$

$$I' = -D_{g_2} I_L \quad (3.29)$$

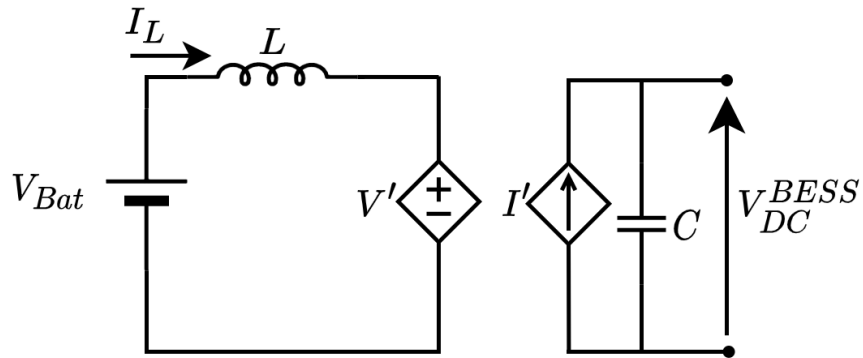


Figure 3-29: Buck/boost AVM equivalent model.

3.5.3 BESS Control Strategy

3.5.3.1 VSC Control System

Figure 3-30 describes the deployed control structure for the BESS-VSC, where grid-forming and grid-following control modes are determined based on the operation of the diesel plant. When the diesel plant is on ($GENSUP = 1$), the BESS-VSC is set to operate in grid-following control by adopting PQ control mode, injecting a predefined active and reactive power (P_{ref}^{BESS} , Q_{ref}^{BESS}) reference by a higher-level controller, such as PMS. Whereas in grid forming control ($GENSUP = 0$), the BESS is set to solely regulate the voltage and frequency of the microgrid in a single master-slave configuration or jointly form the grid with the PV system in a multi-master configuration according to the control

action VSC-Droop, which is triggered by the BESS failure in maintaining the voltage and frequency within prescribed limits.

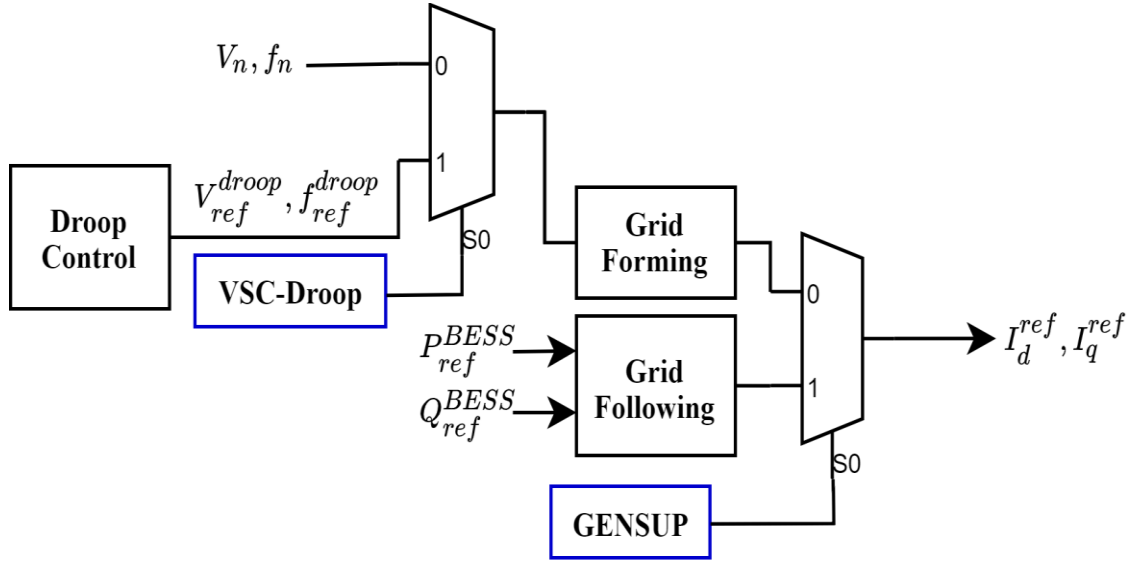


Figure 3-30: Schematic of BESS control strategy.

In islanded mode ($GENSUP = 0$), voltage and droop control loops similar to those detailed in Section 3.4.3.3 governs the BESS-VSC operation. In normal mode ($VSC-Droop = 0$), the PV system is governed under grid-following control synchronized to the grid formed by the BESS operating in grid-forming mode. During normal mode, the d-q axis voltage control loops are provided with nominal voltage and frequency reference values (V_n, f_n). On the other hand, droop grid forming control ($VSC-Droop = 1$) facilitates cooperative regulation of the voltage and frequency by the BESS and PV, which is enabled when BESS fails in maintaining the voltage and frequency within predefined limits.

3.5.3.2 Grid-following Mode

The main purpose of PQ mode is to keep the active power and reactive power output of the converter at specified values, referenced by the PMS ($P_{ref}^{BESS}, Q_{ref}^{BESS}$). From (3.22) and

(3.23), the dq current references (I_d^{ref}, I_q^{ref}) in steady-state can be derived as given in (3.30) and (3.31)

$$I_d^{ref} = P_{ref}^{BESS} / 1.5V_d \quad (3.30)$$

$$I_q^{ref} = -(Q_{ref}^{BESS} - Q_{filter}) / 1.5V_d \quad (3.31)$$

3.5.3.3 Battery Controller

According to Figure 3-31, the buck/boost converter shown in Figure 3-28 regulates the DC-link voltage of the BESS (V_{DC}^{BESS}) while facilitating the charging and discharging modes of the battery array. The V_{DC}^{BESS} is compared with its corresponding reference (V_{DC}^{REF}), which is set to 1.1 kV, to generate the required duty cycle for the buck/boost converter. The duty cycle is then passed to the average value model detailed in Section 3.5.2 to calculate V' and I' associated with the enabled mode of the converter. Based on the measured output DC link power (P_{DC}) shown in Figure 3-28, the mode of the converter is selected.

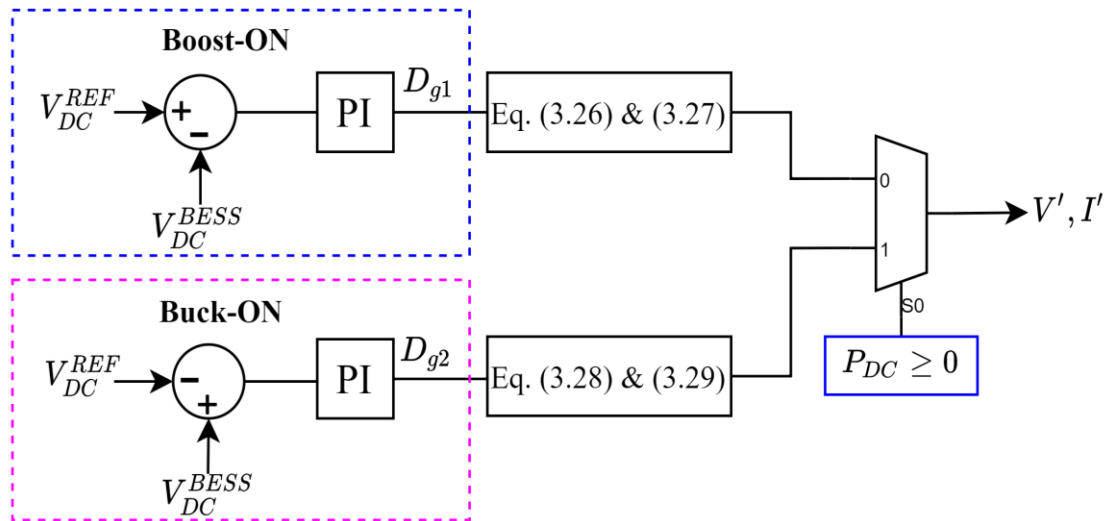


Figure 3-31: Battery controller schematic.

3.6 Results and Discussion

The remote microgrid configuration depicted in Figure 3-1 and the control strategies described were simulated on RTDS® real-time simulation environment. The results obtained under the GENSUP and islanded modes are discussed in the following subsections.

3.6.1 GENSUP mode

As discussed in Section 3.2, under GENSUP mode, the diesel plant supplies power and regulates the voltage and frequency of the microgrid. The PV and BESS operation modes are governed by grid-following control as current-controlled resources as described in Sections 3.4.3.2 and 3.5.3.2. In the scenario shown in Figure 3-32, DIS-1 is enabled from the diesel plant and supplying 0.067 MW, the PV system is injecting 0.285 MW corresponding to an irradiance of 500 W/m², and the BESS is charging at -0.05 MW. Following a sudden load increase around 35 s, DIS-1 increases its active power, providing the required power slack. At 45 s, the irradiance suddenly drops to 300 W/m². The PV MPPT control then tracks the MPPT reference and settles at 0.162 MW. In response to the PV generation drop, DIS-1 provides the required slack power. The voltage and frequency also depict a stable response as shown in Figure 3-32. This scenario presents extreme scenarios to test the stability of the model under sudden load and irradiance changes.

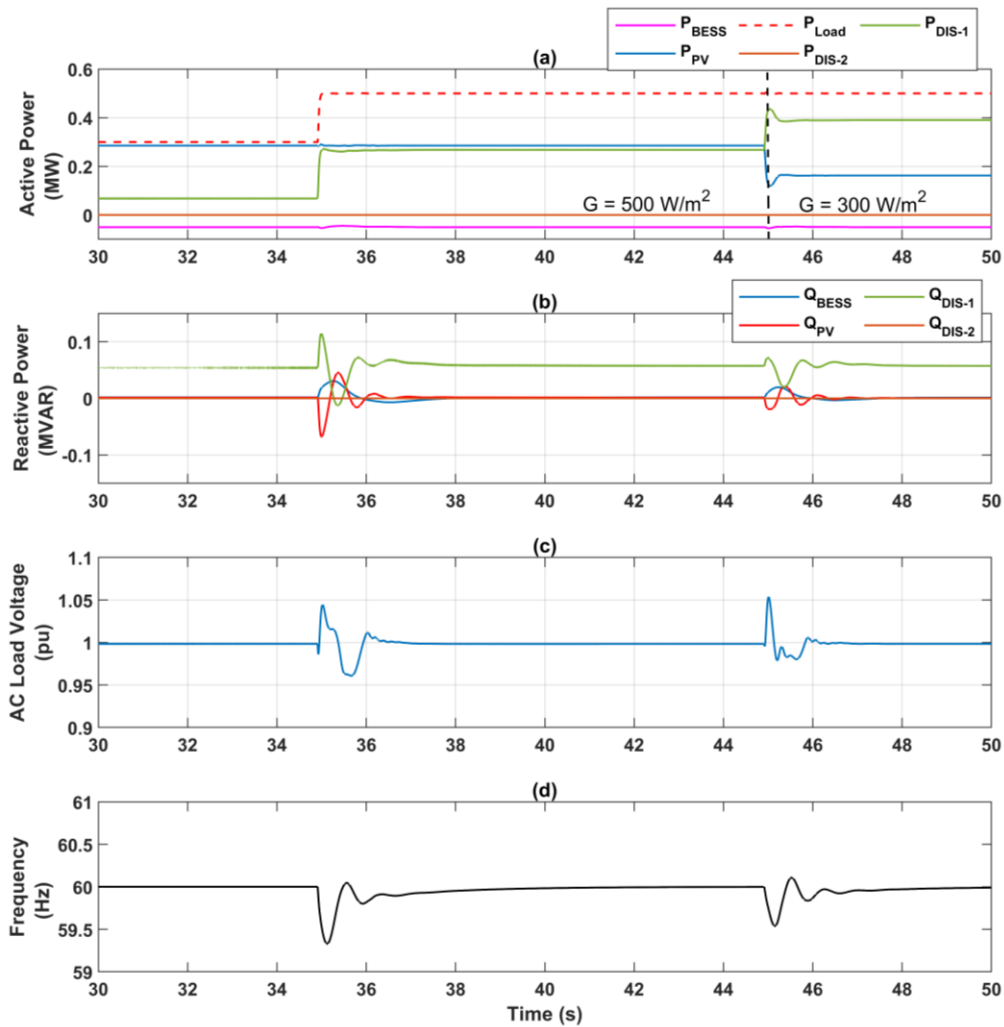


Figure 3-32: GENSUP mode: (a) Active power, (b) Reactive power, (c) AC voltage, and (d) Frequency.

In the scenario showcased in Figure 3-33, the power system is initially supplying a load of 0.5 MW at a unity Power Factor (PF). From the diesel plant, only DIS-1 is supplying active power at 0.22 MW. The PV system is injecting 0.47 MW following the command reference by the MPPT controller for an irradiance level of 800 W/m^2 ($G = 800 W/m^2$), and the BESS is charging at -0.2 MW following the reference command given by the EMS. Also, the PV and BESS are set to operate at unity PF. The reactive power requirement of the lines and the transformers are supplied by DIS-1.

Starting from 15 s, the irradiance gradually decreases and settles at 500 W/m^2 . The PV system tracks the MPPT reference to harness the maximum available PV power and settles at 0.285 MW. Following the PV power change, DIS-1 balances the active power. The PV active power increases responding to a gradual increase in the irradiance initiated at 25 s and settles at 0.34 MW, and DIS-1 provides the required active power slack. The BESS charging power remains stable at its corresponding reference during the periods of irradiance change. Around 30 s, a gradual increase in the BESS reference command is initiated. The BESS shifts its operation into discharging mode and settles at 0.1 MW. DIS-1 subsequently reduces its output power according to the new microgrid conditions. Starting from 40 s, the BESS active power shifts downward following the new reference command, whereas DIS-1 provides the required power balance. The PV system depicts a stable response while changing the BESS reference command. A load decrease initiated around 50 s, followed by DIS-1 power reduction. The PV and BESS active power remains constant as expected during the period of load change. The reactive power response of the PV and BESS depicts a slight change from its nominal value of zero during periods of active power change due to the slight frequency deviation and presence of small coupling between the active and reactive power. However, once the active power settles, the reactive power gets closely regulated at its nominal value. In all demonstrated scenarios, the frequency and AC voltage showcase a stable response. The frequency deviations remain within $\pm 0.5 \text{ Hz}$, which should be acceptable for an isolated grid, and the somewhat slow governor response of diesel generators is also evident from Figure 3-33.

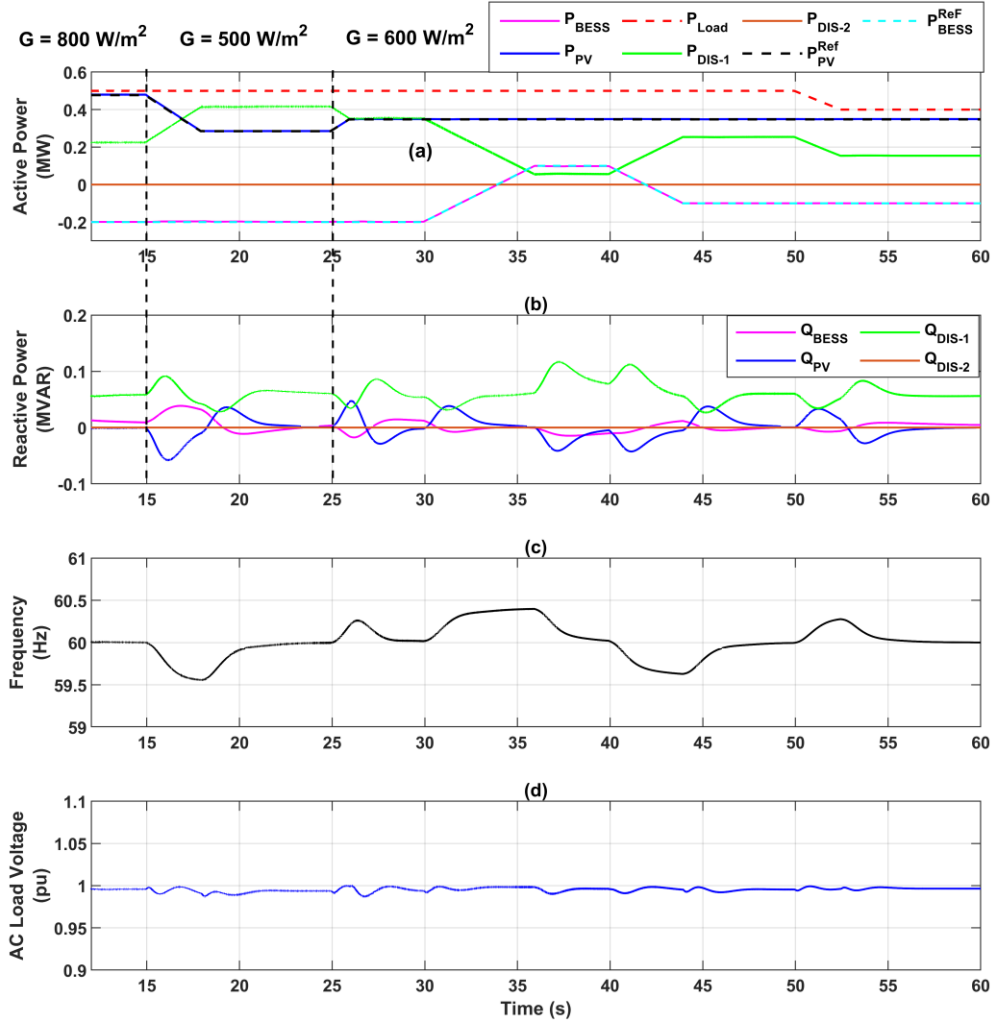


Figure 3-33: GENSUP mode: (a) Active power, (b) Reactive power, (c) Frequency, and (d) AC voltage.

Figure 3-34 demonstrates a case where the diesel plant is governed under droop control. The DIS-2 unit is initially supplying an active power around 0.4 MW under isochronous mode. Also, the required reactive power is supplied by DIS-2 unit. Around 12 s, reconnection of DIS-1 is initiated. Therefore, the diesel plant switches its operation into droop mode to share the load between DIS-1 and DIS-2 units. At 18 s, the load gradually increases and settles at 0.7 MW. This change in load is shared between DIS-1 and DIS-2 units based on their ratings. Starting at 33 s, a decrease of load active power demand takes place. The diesel units subsequently decrease their active power to balance the generation

and load demand. Around 48 s, DIS-1 unit receives a disconnection command and responding to it, DIS-1 unit decreases its active and reactive power by adjusting the power set point of the droop curves as discussed in Section 3.3 to facilitate smooth disconnection. DIS-2 supplies the required power to meet the load demand during the period of DIS-1 unloading. The frequency response depicts a slight change from the nominal value as a result of deploying the droop control. However, once the load settles, the frequency gets close to the nominal value due to the deployment of the speed regulation control loop discussed in Section 3.3.1. Also, the frequency excursions are smaller in this case due to the presence of Dis-2, the larger of the two diesel generators, or both of the diesel generators connected to the grid. In the demonstrated scenarios, the AC voltage exhibited a stable response.

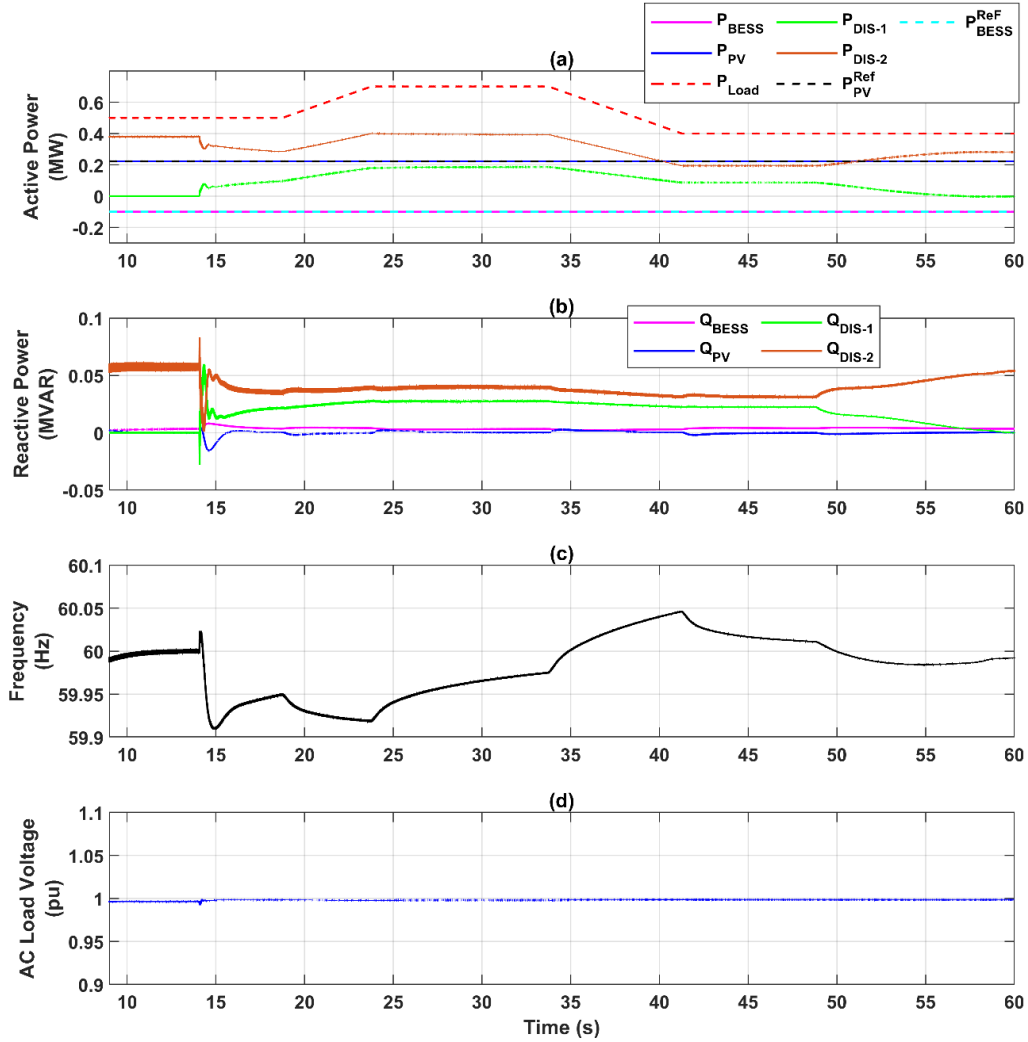


Figure 3-34: Diesel plant control: (a) Active power, (b) Reactive power, (c) Frequency, and (d) AC voltage.

3.6.2 Islanded mode

As discussed in Section 3.4.3, under the grid-following control in islanded mode, PV unit operates as a current source synchronized to the AC grid formed and regulated by the BESS controls. In the scenario showcased in Figure 3-35, the power system is initially supplying a load of 0.3 MW at a unity PF. The PV unit active power output is following the commanded reference value for an irradiance level of 100 W/m^2 . Also, the PV reactive power output is regulated at zero. Due to the lower PV power availability, BESS supplies

most of the required active power to balance the grid. Also, the reactive power requirement of the lines and transformers are supplied by the BESS at a value of 0.06 MVAR.

Starting from 15 s irradiance gradually increases and settles at 800 W/m^2 . The MPPT controller changes the PV power reference to harness the maximum available power, and the PV output closely follows this reference. When the PV power output exceeds the load demand, the BESS balances the active power by moving its operation into the charging mode. The PV active power reference reduces following a gradual irradiance reduction initiated at 23 s. The PV output settles in a new steady-state condition at 0.19 MW and the BESS-VSC provides the required active power slack. Starting at 28 s, a load change takes place, increasing both active and reactive power demand. The BESS increases its output power to balance the modified load demand while the PV unit continues its operation in the MPPT mode at a unity power factor. In all demonstrated system changes, the frequency and AC voltage variations showcase a stable response.

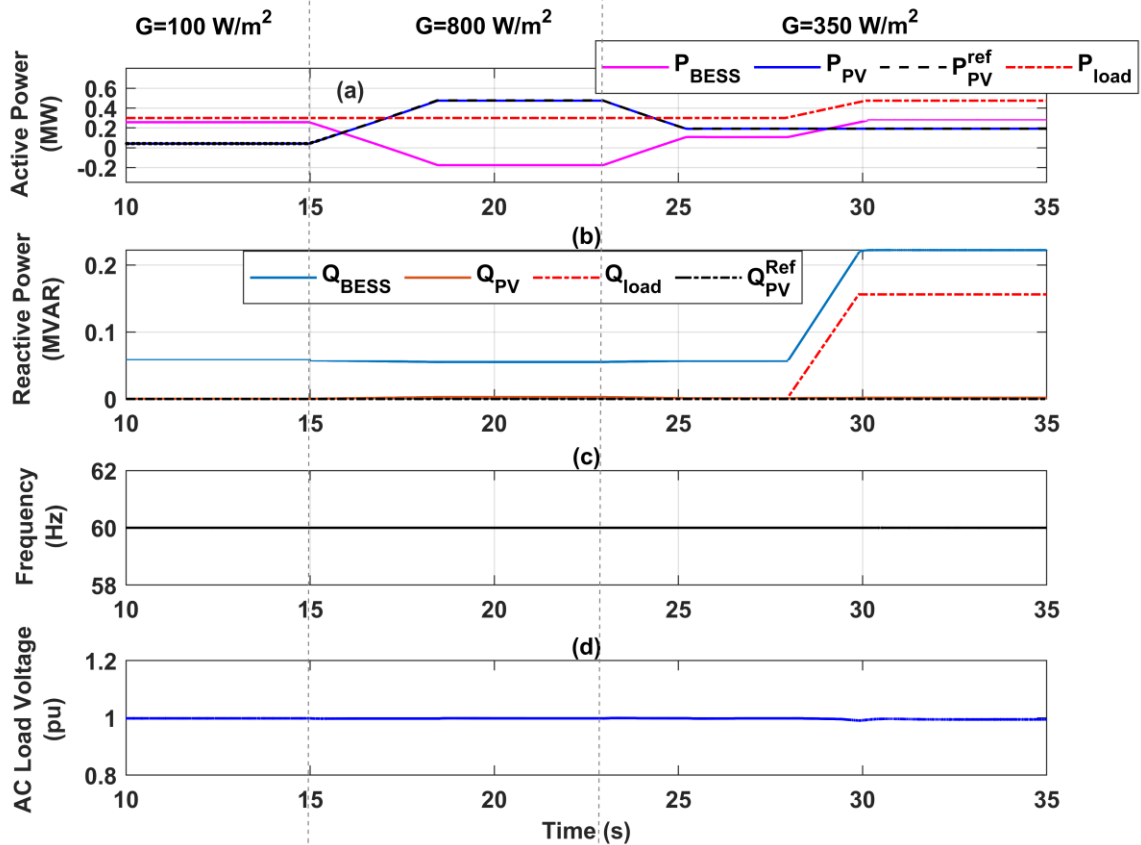


Figure 3-35: Islanded mode: (a) Active power, (b) Reactive power, (c) Frequency, and (d) AC voltage.

Figure 3-36 depicts the response of controls imposed under the limited power mode discussed in Section 3.4.3.4. Initially, the PV output is controlled around 0.1 MW under the MPPT control, and the BESS supplies the balance of power, operating in the discharging mode. Around 15 s a gradual increase in the irradiance initiates an upward change in the PV power reference. The PV output settles at 0.47 MW while the BESS shifts its operation into charging mode. Anticipating a possible overcharge condition, the supervisory controller initiates the PV limited power mode to move the grid-forming BESS into the discharging mode of operation. As shown in Figure 3-36(a), this allows the BESS to continue the grid-forming task while avoiding the violation of its overcharge limit. The depicted power curtailment causes a deviation from the PV MPPT operation as reflected

in the PV output voltage variation as shown in Figure 3-36(b). Around 25 s, the irradiance starts to decrease and settles at a value of 300 W/m^2 . This change in irradiance reduces the PV active power reference and shifts its operation out of the limited power mode and back into the MPPT mode.

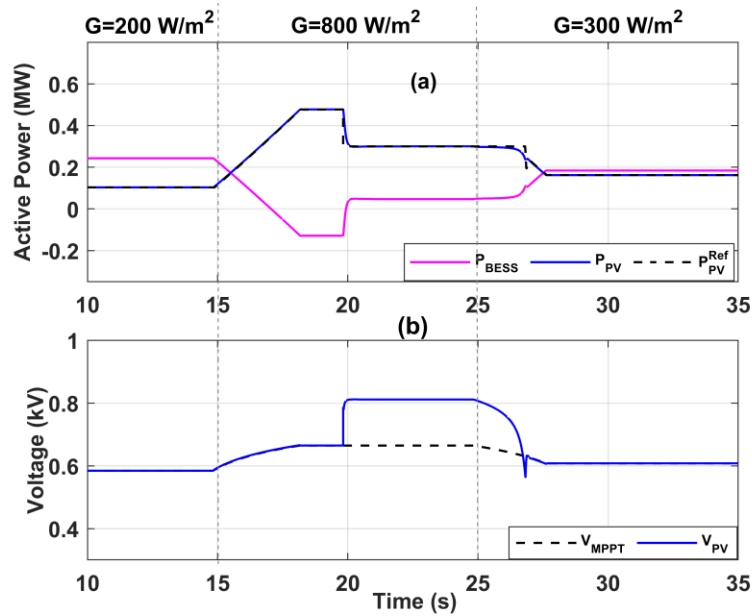


Figure 3-36: PV limited power mode: (a) Active power, and (b) PV voltage.

3.6.3 PV-BESS Joint Grid-forming

In this mode, both PV system and BESS are contributing for grid-forming functions, governed by the external droop control loops as explained in Section 3.4.3.3. The PV unit was configured to operate near MPPT with adequate reserve under normal conditions and to take over the load-balancing task in the event of a BESS failure. Figure 3-37 depicts a scenario where both units are contributing to the grid-forming task. Initially, the system is supplying a load close to 0.4 MW at unity PF. PV-VSC active power is regulated at the maximum power value corresponding to an irradiance level of 500 W/m^2 . The BESS-VSC is supplying the remaining active power at a power level close to 0.13 MW. The reactive

power requirement of the lines and transformers is shared between the BESS and PV VSCs as shown in Figure 3-37(b).

Around 15 s, the load increases to a value of 0.5 MW. PV-VSC continues its operation providing the maximum power and the BESS-VSC increases its active power to balance the grid. The irradiance starts to increase around 20 s and settles at a value of 1000 W/m². BESS moves into the charging mode to balance the grid by absorbing the excess energy. Under all simulated system changes the reactive power outputs from the two VSCs showcase a stable response. Also, the AC voltage and system frequency are maintained at their nominal values. The BESS fails close to 25 s causing the PV-VSC to move away from its MPPT operation and starts to solely form the grid while balancing the active and reactive power. The sudden change of controls initiates a small transient period, and the system recovers to a steady-state within 0.4 s. At 30 s, the load starts to decrease and settles at 0.3 MW. The PV-VSC reduces its output power according to the updated grid conditions and the system runs smoothly.

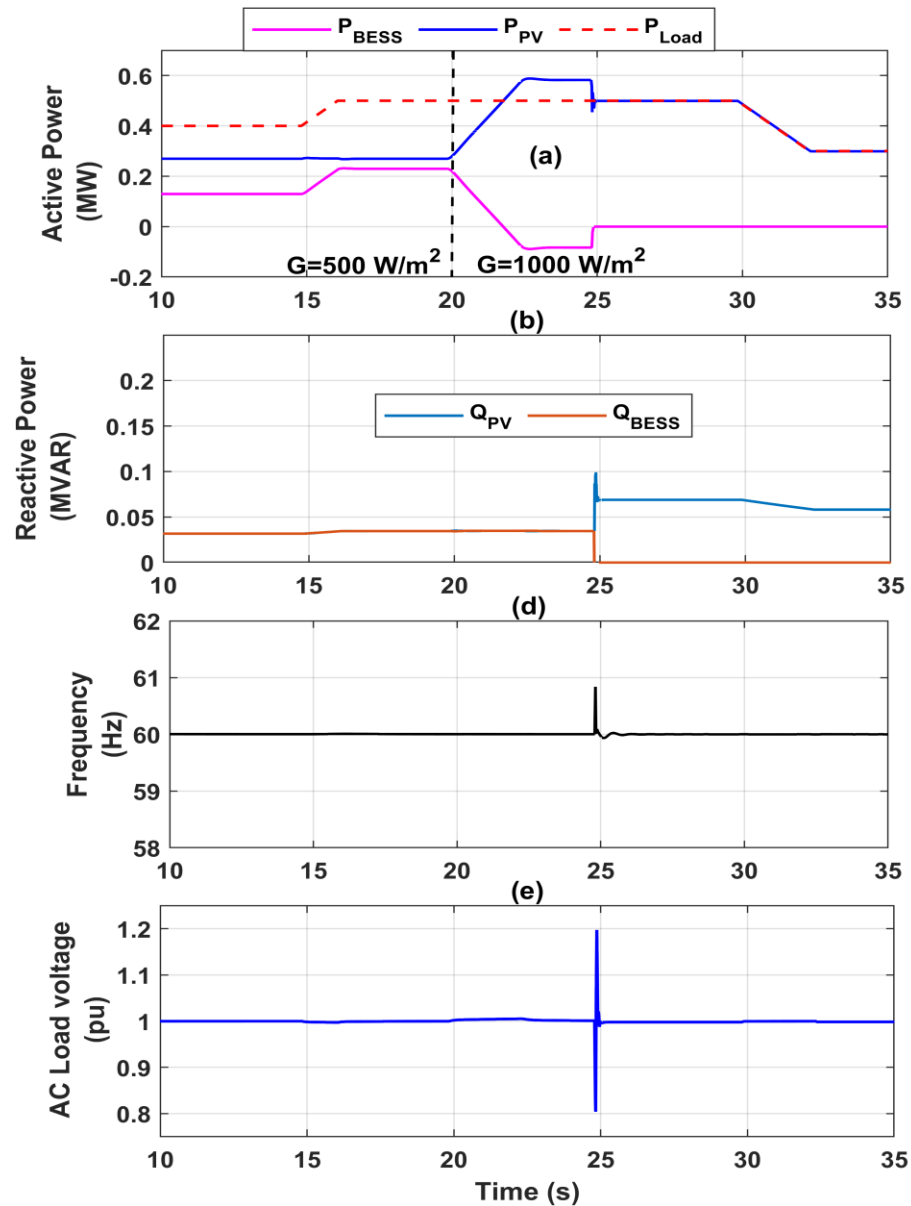


Figure 3-37: PV-BESS joint grid-forming: (a) Active power, (b) Reactive power, (c) Frequency, and (d) AC voltage.

Figure 3-38 depicts the response of control imposed under limited power mode. Initially, the PV output is controlled around 0.45 MW under MPPT control, and the BESS supplies the balance of power operating in the discharging mode. Around 14 s, the battery reaches its upper SOC limit (SOC_{max}), which is defined to be 90% in this case as shown in Figure 3-38(b). The supervisory controller anticipates an overcharging scenario and initiates the

PV limited-power mode to shift the grid-forming BESS into an idle state as detailed in Section 3.4.3.3. Around 19 s, The PV output power increases following a load increase keeping the BESS at an idle state. A load change starting at 28 s increases the active power demand. The BESS starts discharging while the PV unit shifts to MPPT control mode. Close to 38 s, the irradiance starts to decrease and settles at a value of 500 W/m^2 . This change reduces the PV active output power while the BESS active output power shifts upward to balance the load demand. As shown in Figure 3-38(a) and (b), this allows the BESS and PV to jointly form the grid while avoiding overcharging scenario.

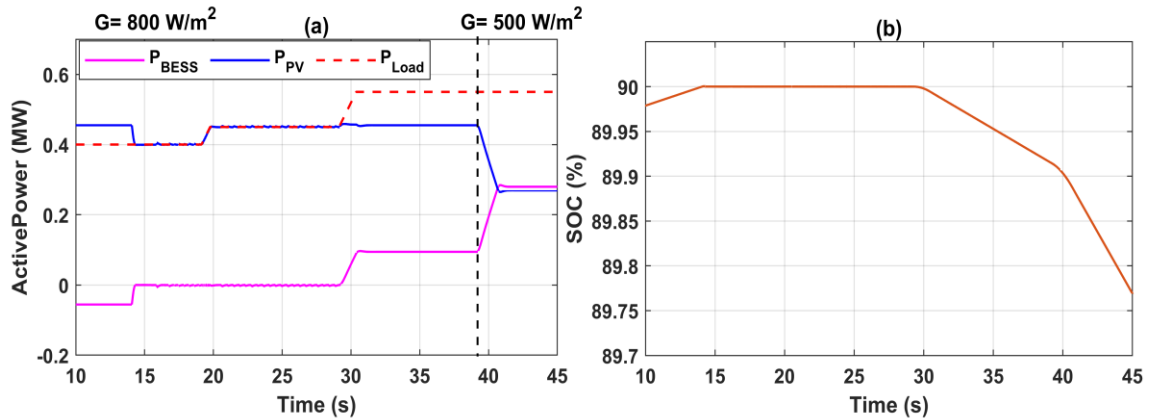


Figure 3-38: VSC droop limited power mode: (a) Active power, and (b) SOC.

3.7 Summary

Chapter 3 presented the modelling details of the considered microgrid system. Detailed descriptions about the control loops of each DER were also provided. Finally, results for validating the performance of microgrid DERs under the discussed modes were also presented.

Chapter 4

Power Management System

4.1 Introduction

This chapter presents the development of dispatch and transition functions of the PMS for the considered microgrid, following the guidelines provided in IEEE 2030.7-2017 standard.

4.2 Power Management System Core Functions

4.2.1 Dispatch Function

A dispatch rule for the considered microgrid shown in Figure 3-1 is formulated under the guidance of the IEEE 2030.7-2017 standard. The designed dispatch strategy integrates the optimum control signals coming from an optimization framework employed in the EMS control layer provided in [70]. The EMS control signals contain start/stop signals for the diesel generators (U_{DIS-1}^{EMS} , U_{DIS-2}^{EMS}) and BESS power reference (P_{BESS}^{EMS}). On the other hand, the PMS dispatch strategy is based on a set of criteria summarized in Table 4-1. The main task of the developed dispatch strategy is to provide the local controller of DERs with the appropriate optimum power commands suggested by the EMS while being subjected to the set of criteria outlined in Table 4-1. Finite State Machine (FSM) concept was utilized when

programming the flowcharts provided under GENSUP and islanded dispatch modes. Also, a blue colour code is used to mark the EMS signals in the next subsections.

Table 4-1: Constraints of dispatch function.

Parameters	Criteria
BESS	SOC Limitations: $SOC_{min} \leq SOC \leq SOC_{max}$ Active Power Limitation : $P_{BESS}^{min} < P_{BESS} < P_{BESS}^{max}$
Diesel Plant	Active Power Limitation: $0.3P_{DIS-n}^{rated} \leq P_{DIS-n} \leq P_{DIS-n}^{rated}$
Reserve Generation Capacity (RGC)	Reserve Power Limitation: $P_{RGC} \geq P_{Available} - P_{Load}$

4.2.1.1 GENSUP Dispatch

Figure 4-1 describes the deployed dispatch strategy in GENSUP mode. GENSUP mode is detected by the status of the breakers of the diesel plant, where the PV and BESS operate in grid-following mode as discussed in Chapter 3. Based on the constraints mentioned in Table 4-1, the GENSUP dispatch strategy can be illustrated in three distinct cases marked by the numbers inside red circles shown in the flow chart of Figure 4-1. The developed strategy considers a deadband for each condition to prevent frequent switching between conditions.

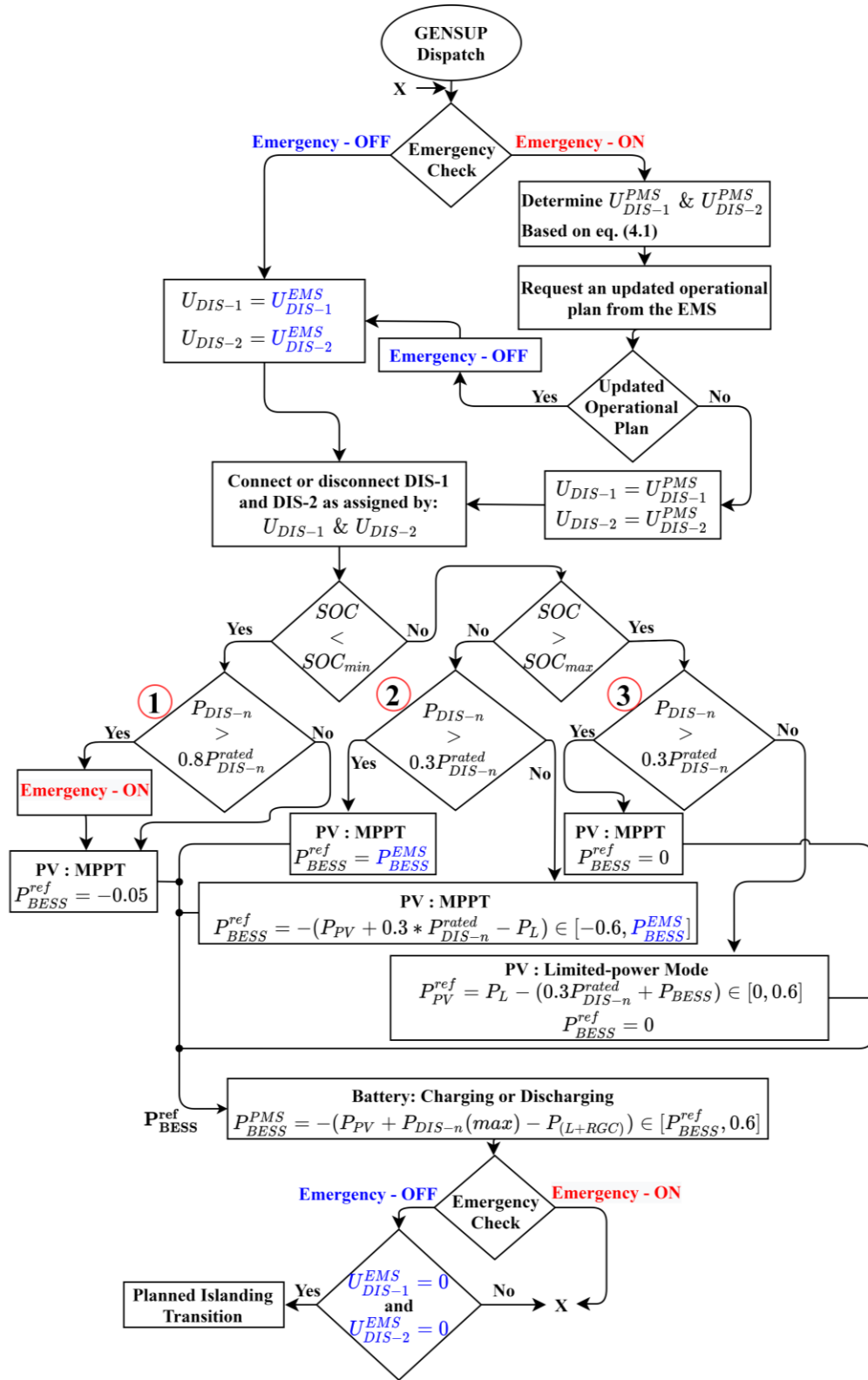


Figure 4-1: GENSUP dispatch strategy.

Case-1: This case appears when the SOC of BESS reaches its minimum value (SOC_{min}). In response, the PMS instructs the BESS to start charging at very low power. during this case, if the diesel plant loading is higher than 80% of the rated value, the PMS commands an emergency transition, in which the PMS connects the required diesel units to satisfy the condition in (4.1), where ($n = 1, 2, 1 + 2$) represents the diesel units, and L refers to the load. Note that during emergency mode, the PMS actions override the diesel plant EMS signals and request for updated signals from the EMS to turn off emergency mode. The required RGC can be calculated as in (4.2).

$$P_{DIS-n}^{rated} \geq P_{L+RGC} + 0.05 - P_{PV} \quad (4.1)$$

Case-2: This case comes into effect when the diesel plant fails in meeting the minimum load demand (30% of rated power) to avoid low fuel efficiency [71]. Therefore, the P_{BESS}^{ref} is adjusted to charge the BESS at a higher power in order to maintain the minimum loading of the diesel plant. Otherwise, the P_{BESS}^{ref} follows the EMS reference command ($P_{BESS}^{ref} = P_{BESS}^{EMS}$).

Case-3: This case appears when the SOC reaches its maximum value (SOC_{max}). Therefore, the battery is shifted into idle state and PV becomes responsible for maintaining the minimum loading demand of the diesel plant. During this case, the PV system operates under limited-power mode, if the diesel plant power is less than the minimum demand.

Note that under emergency off, the system inspects the EMS transition signals (U_{DIS-1}^{EMS} , U_{DIS-2}^{EMS}) at each loop to enable/disable a diesel generator or perform islanding transition

($U_{DIS-1}^{EMS} = 0, U_{DIS-2}^{EMS} = 0$). Also, the P_{BESS}^{ref} is determined according to the SOC of the BESS as explained in the above three cases. The derived P_{BESS}^{ref} is then used to obtain the P_{BESS}^{PMS} , which is fed to BESS. P_{BESS}^{PMS} is derived to maintain an adequate reserve and prevent overloading of the diesel plant, and therefore dealing with the random nature of the PV power and load. The formula to derive the RGC is shown in (4.2).

$$P_{RGC} = K_L P_L + K_{PV} P_{PV} \quad (4.2)$$

where P_{RGC} is the required reserve power; K_L and K_{PV} are the reserve coefficients of the load and PV, respectively; P_L and P_{PV} refers to the active power demand and PV system active power generation, respectively.

4.2.1.1.1 Application of FSM Computational Model

FMS are used when programming the PMS to represent distinct states of the program. The use of FSM makes it easy to assemble deadbands between the states, which prevents frequent switching between different cases. Figure 4-2 shows an example of a decision tree represented using FSM computational model, considering 1% deadband.

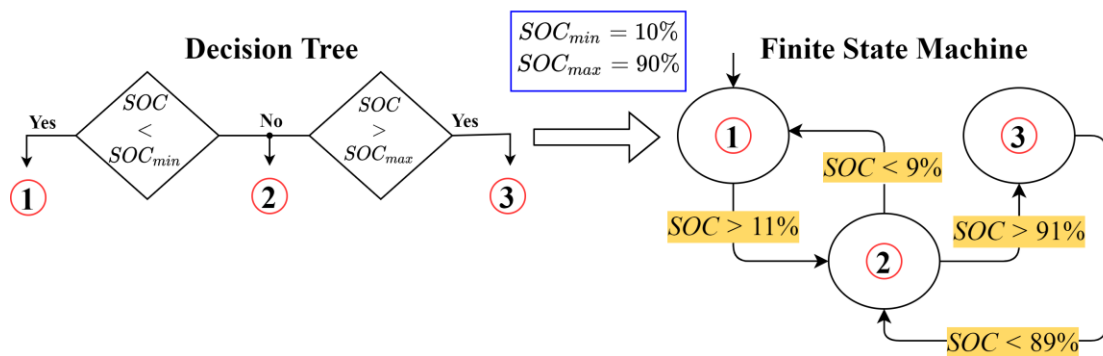


Figure 4-2: Decision tree to FSM conversion.

To illustrate, a Pseudo code is shown below to describe how the FSM algorithm works.

Case State

1:

/Lines below are executed if State equals one./

MPPT = 1

P_BEES = -0.05

IF P_Diesel > 0.8 P_rated

Emergency = 1

Else

Emergency = 0

END-IF

IF SOC > 11

State = 2

END-IF

2:

/Lines below are executed if State equals two./

Statement-1

...

IF SOC > 91

State = 3

ELSEIF SOC < 9

State = 1

END-IF

3:

/Lines below are executed if State equals three./

Statement-1

...

IF SOC < 89

State = 2

END-IF

4.2.1.2 Isolated Dispatch

Figure 4-3 depicts the isolated dispatch strategy where the PV and BESS are operating in the absence of diesel generation. The BESS operates in grid-forming mode, regulating the voltage and frequency of the microgrid, whereas the PV system is governed under grid-following control synchronized to the grid formed by the BESS. Note that, a deadband for conditions is considered when developing the isolated dispatch strategy.

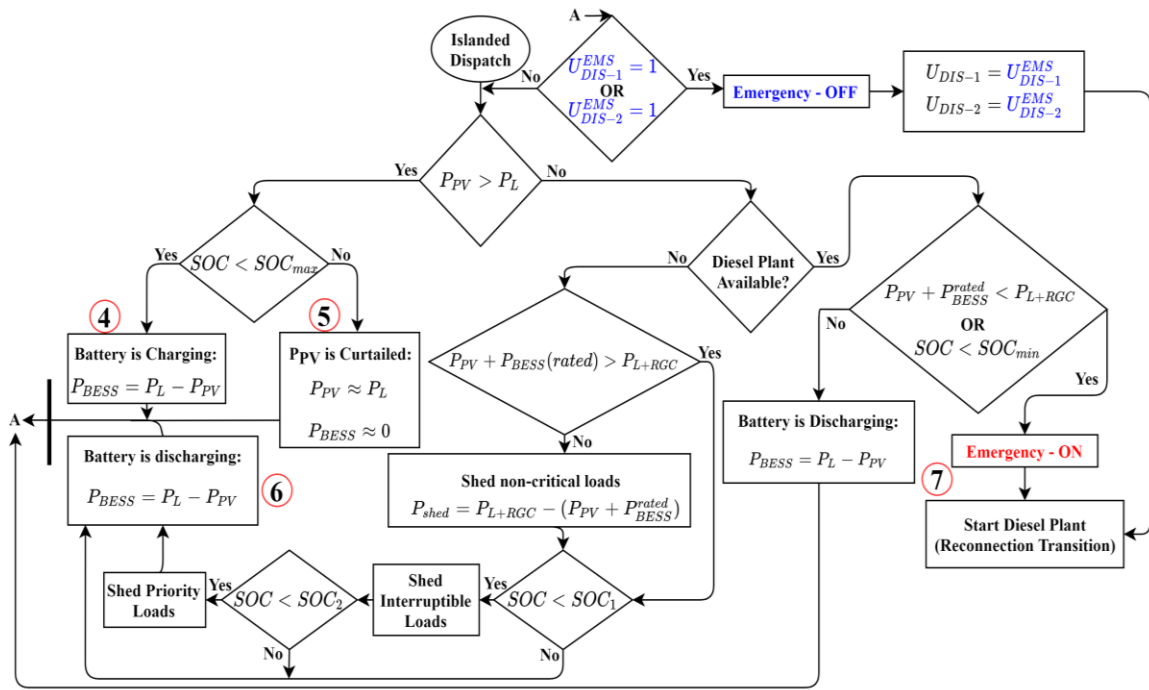


Figure 4-3: Dispatch strategy in isolated mode.

Based on the constraints mentioned in Table 4-1, isolated dispatch strategy can be divided into four different distinct cases.

Case-4: In cases of surplus PV power and BESS SOC is not fully charged, the battery operates as a slack bus, balancing the load and generation by absorbing the extra power generated from the PV unit. As a result, the battery is charging, and PV continues to operate in MPPT mode.

Case-5: This case is a result of excessive PV generation and low load over a long period of time, causing the battery to fully charge. Therefore, the PV operation is shifted to limited-power generation to track the connected load ($P_{PV} \approx P_L$) and consequently, the battery is pushed into idle state ($P_{BESS} \approx 0$).

Case-6: In this case, a high load and relatively lower PV generation, causing the battery to discharge and since the diesel plant is out of service in this case, power and energy reserve schemes are applied. For power reserve, the system must maintain an adequate reserve to deal with uncertainties as discussed in Section 4.2.1.1. For energy reserve, the system is set to disconnect non-critical loads based on their priority if the SOC falls below a certain value to prolong the system operation.

Case-7: In cases where the diesel plant is available and load exceeds the PV generation, the BESS is discharging. If a sustained period of high load caused the SOC to fall below SOC_{min} or the BESS didn't have enough energy to supply the deficit, the PMS commands the diesel plant to be connected based on criteria in (4.1). As a result, the system switches to GENSUP dispatch under emergency condition (Emergency - ON).

Note that at each loop the system checks EMS transition signals (U_{DIS-1}^{EMS} , U_{DIS-2}^{EMS}) to determine the dispatch mode for the next period.

4.2.2 Transition Function

4.2.2.1 Planned Islanding

Planned islanding occurs when EMS requests the diesel plant to disconnect from the microgrid ($U_{DIS-1} = 0$, $U_{DIS-2} = 0$). To realize smooth and safe disconnection, planned islanding is made of three steps as shown in Figure 4-4.

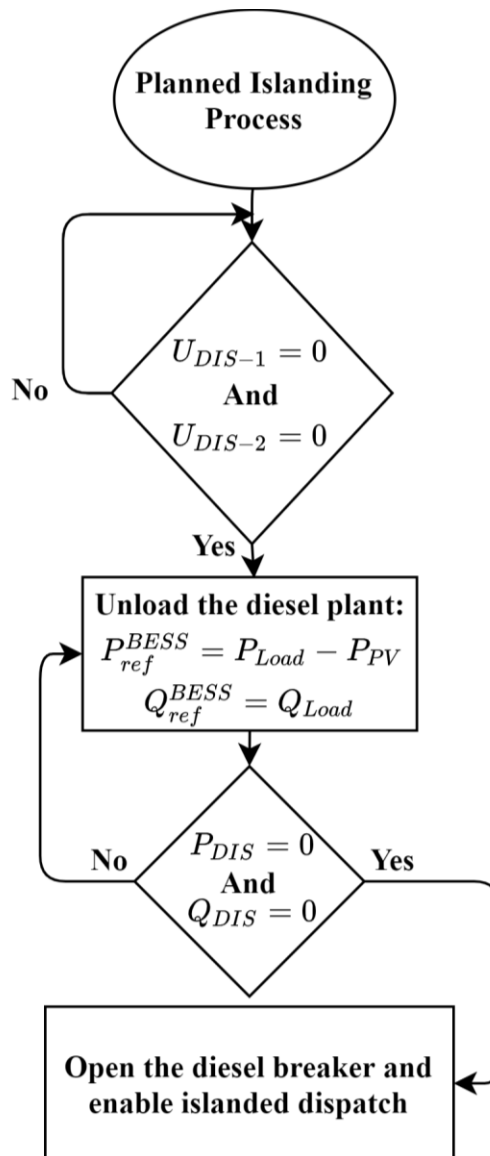


Figure 4-4: Planned islanding transition process.

4.2.2.2 Reconnection

According to IEEE 1547-2018 standard, before reconnecting a diesel generator with the grid its voltage, frequency and phase angle should match with the grid and be within specified limits. The recommended reconnection limits as stated in IEEE 1547-2018 are shown in Table 4-2 [2].

Table 4-2: Synchronization parameters limits [2].

Aggregate rating of DER units (kVA)	Frequency difference (Δf , Hz)	Voltage difference (ΔV , %)	Phase angle difference ($\Delta\theta$, °)
0 – 500	0.3	10	20
500 – 1500	0.2	5	15
1500 – 10000	0.1	3	10

To illustrate, once a reconnection command from the EMS or PMS is acknowledged ($U_{DIS-1} = 1$, $U_{DIS-2} = 1$), the PMS turns on the active synchronization scheme of the diesel plant discussed in Chapter 3. Once the frequency, voltage and phase angle differences across the circuit breaker are within the limits, the diesel generator breaker is closed. After reconnection, the GENSUP dispatch strategy is enabled, and BESS will be switched to grid-following control mode. Figure 4-5 presents the reconnection process of the diesel plant. Synchronization parameters provided by the standard are usually used for microgrid systems connected to a stiff grid. However, when reconnecting a diesel generator in an isolated microgrid, a smaller phase angle difference is recommended. In this case, a

phase angle difference of 0.5° is used to ensure stable dynamics and avoid voltage spikes when reconnecting a diesel generator.

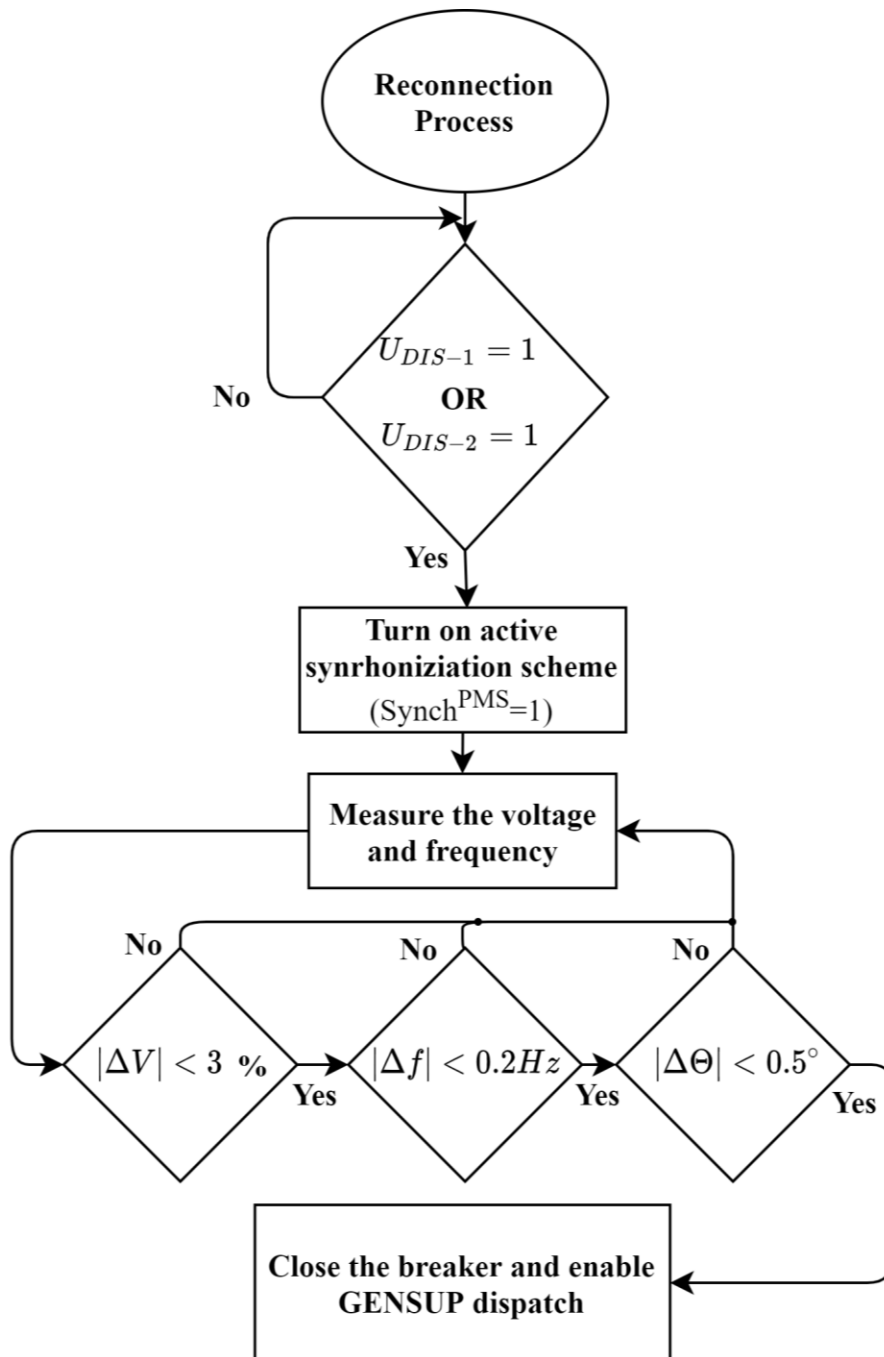


Figure 4-5: Reconnection process scheme.

4.2.2.3 Unplanned Islanding

In this study, unintentional islanding events are detected by inspecting the status of diesel plant breakers. Upon unintentional islanding, an emergency dispatch strategy is adopted to stabilize the microgrid voltage and frequency. The emergency dispatch order is performed as follows:

- Shed non-critical loads (P_{Shed}) determined by (4.3) based on the load priority to avoid unnecessary load shedding. To promote resiliency during unplanned islanding transition, higher reserve coefficients are used in (4.3).

$$P_{Shed} = P_{L+RGC} - (P_{PV} + P_{BESS}^{max}) \quad (4.3)$$

- Switch the BESS control strategy to grid-forming strategy.
- Switch to islanded dispatch strategy.

4.3 Summary

In this chapter, the development of the microgrid controller functions (PMS) namely, dispatch and transition functions are presented. A dispatch rule strategy considering a set of constraints is used to derive the dispatch model for GENSUP and islanded modes. The integration of EMS control signals into the PMS functions to obtain the optimal operation of the considered microgrid is also described. Furthermore, the applicability and importance of power and energy reserve schemes for isolated microgrid is discussed. Moreover, a transition function to guide the system for smooth and safe transition such as reconnection, planned islanding and unplanned islanding is demonstrated.

Chapter 5

Microgrid Testbed

5.1 Introduction

This chapter introduces the test setup developed at the intelligent power grid laboratory of the University of Manitoba to evaluate the performance of the microgrid control system. The functionality of the proposed PMS is demonstrated through CHIL simulations. The structure of the testbed, the development and coordination of the hierarchical control levels, and the integration of the IEC-61850 communication protocol are discussed.

5.2 Elements of the Microgrid Testbed

A laboratory setup that employs CHIL simulations to test the microgrid control system was constructed. In CHIL simulations, the controller under test is interfaced to a DRTS in order to perform closed-loop real-time testing. The controller typically exchanges low voltage signals with DRTS through a data exchange interface, which can be facilitated using analog and digital I/O cards and/or via Ethernet-based communication protocols. This interface should resemble as much as possible to the interface expected in the field application for properly testing the functionalities. The communication interface is required to provide fast and reliable communication as well as transmission of large sets of data, which are very crucial for a closed-loop CHIL testing setup.

The schematic of the experimental setup is shown in Figure 5-1. The microgrid virtual system and its associated primary control loops discussed in Chapter 3 were established inside the DRTS. A SEL RTAC-3350 digital automation controller and a desktop computer running MATLAB® were employed in the HIL testbed as the microgrid control system. The goal of this setup is to evaluate the performance of the microgrid control system implemented on the SEL RTAC-3350 digital controller. The testbed setup specifications and requirements were developed following the new IEEE 2030.7-2017 Standard that outlines the microgrid controller specifications.

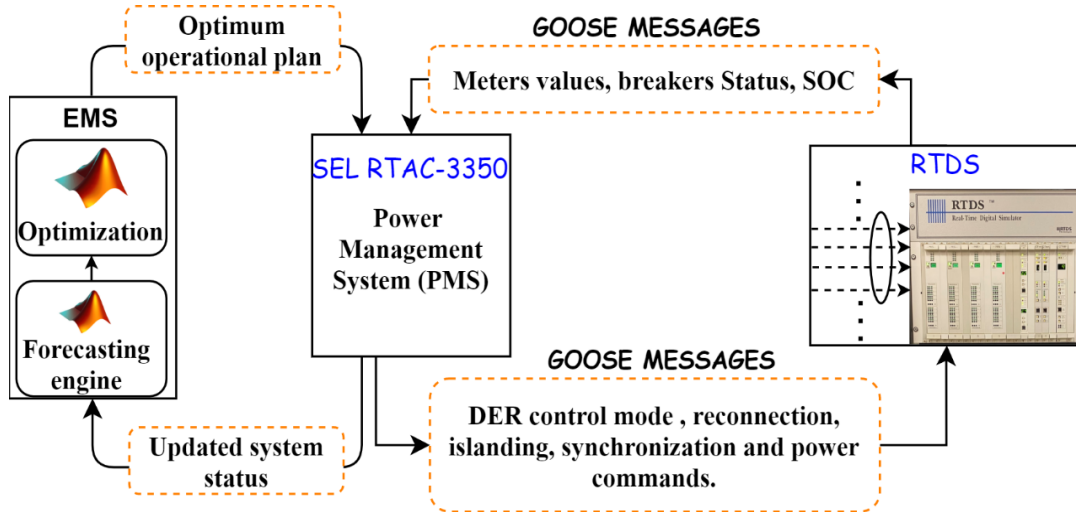


Figure 5-1: CHIL testbed testing platform.

Figure 5-2 is a photo showing the setup in the lab. The image shows the PC, SEL RTAC, and RTDS® devices that are connected via the network switch.

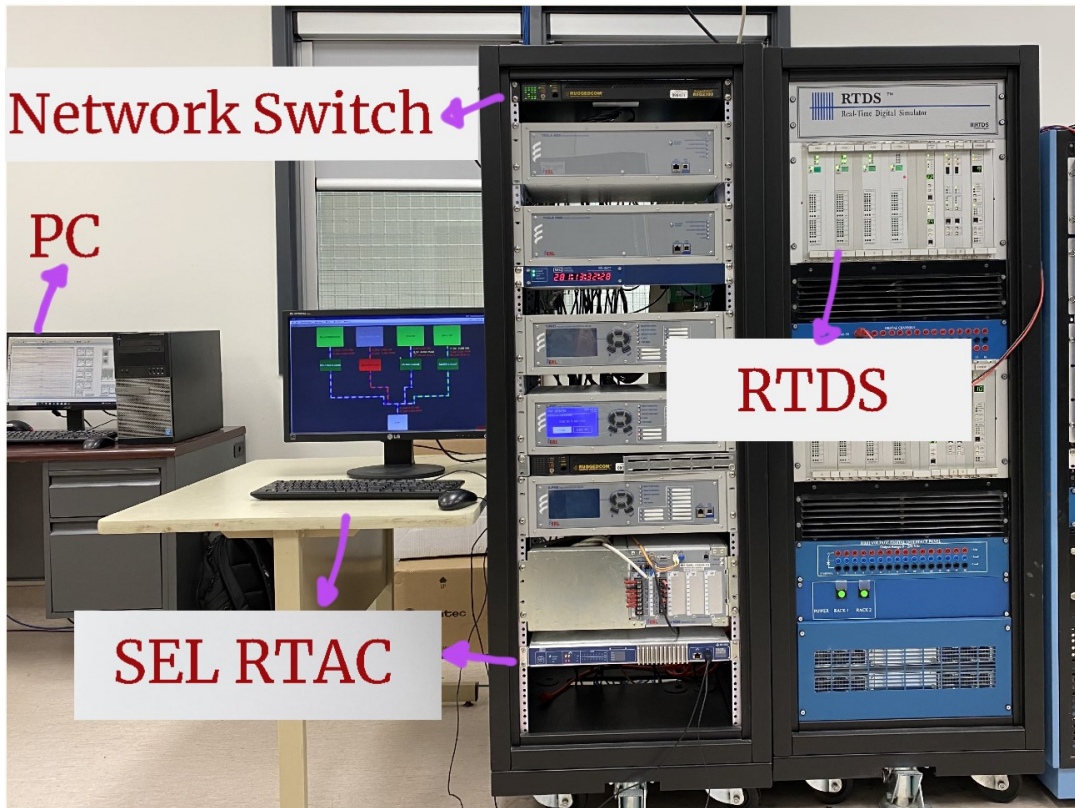


Figure 5-2: Laboratory setup.

5.2.1 Energy Management System

To achieve an optimal operation of the system, an EMS was designed in MATLAB software environment. The EMS was deploying a day-ahead operational planning algorithm, as well as a model predictive control based uncertainty handling algorithm to determine the commitment status of diesel generators, their real power setpoints and the setpoints for the BESS on an hourly basis. These algorithms have been developed through the previous research at the intelligent power grid laboratory of the University of Manitoba and presented in [70] and [10].

5.2.2 Power Management System

The PMS detailed in Chapter 4 was implemented in the SEL RTAC-3350 automation controller. The RTAC is a real-time automation controller with customizable functions and configurations. The features of this product include 1 ms execution time, built-in Human Machine Interface (HMI), support of several communication protocols, including Modbus, DNP3, IEC 61850, etc., and programmability using IEC 61131-3 logic engine. The proposed PMS detailed in Chapter 4 was programmed using the standard structured text language defined in IEC-61131-3 standard. The PMS on SEL RTAC-3350 interacts with both the EMS running on the PC and the microgrid simulated in DRTS to achieve a coordinated operation between the primary level control layer and the EMS control layer.

5.2.3 Communication Links

The communication link between the RTDS® rack and the SEL RTAC-3350 was established using the IEC-61850 protocol. It allows exchanging measurements data and breaker signals through GOOSE messages, thus developing a closed-loop testing setup. Based on the update time of the PMS, the requirements for communication interfaces such as latency and bandwidth are determined. From stability perspective, the round-trip signal latency should be shorter than the update time of the PMS. The recommended execution cycle time for the PMS as reported in [72] should be in the range of 100-500 ms. In this study, 100 ms execution cycle interval is set. Although GOOSE messaging is intended for communicating events, 100 ms execution interval allowed using Analogue GOOSE messages for transferring both measurements and status signals, avoiding use of multiple protocols [73].

A complete description of the measurements, control and status data exchanged among different components in the system is given in Tables A-1 and A-2 of Appendix. A.

5.2.4 Human Machine Interface (HMI)

An HMI that can be used to visually monitor and track the real time status of the microgrid, and to input manual control commands is programmed. The designed HMI comprises a single line diagram, displaying information for users to view, such as meter measurements and status of circuit breakers. Figures 5-3, 5-4, and 5-5 show some snapshots of the developed testbed HMI.

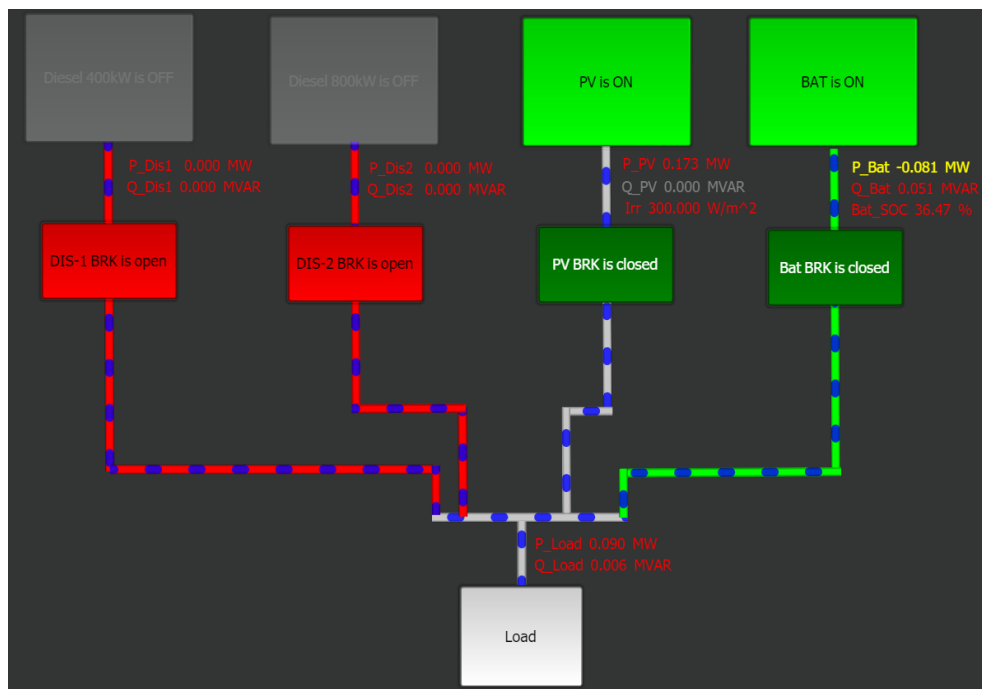


Figure 5-3: Single line diagram of the HMI.

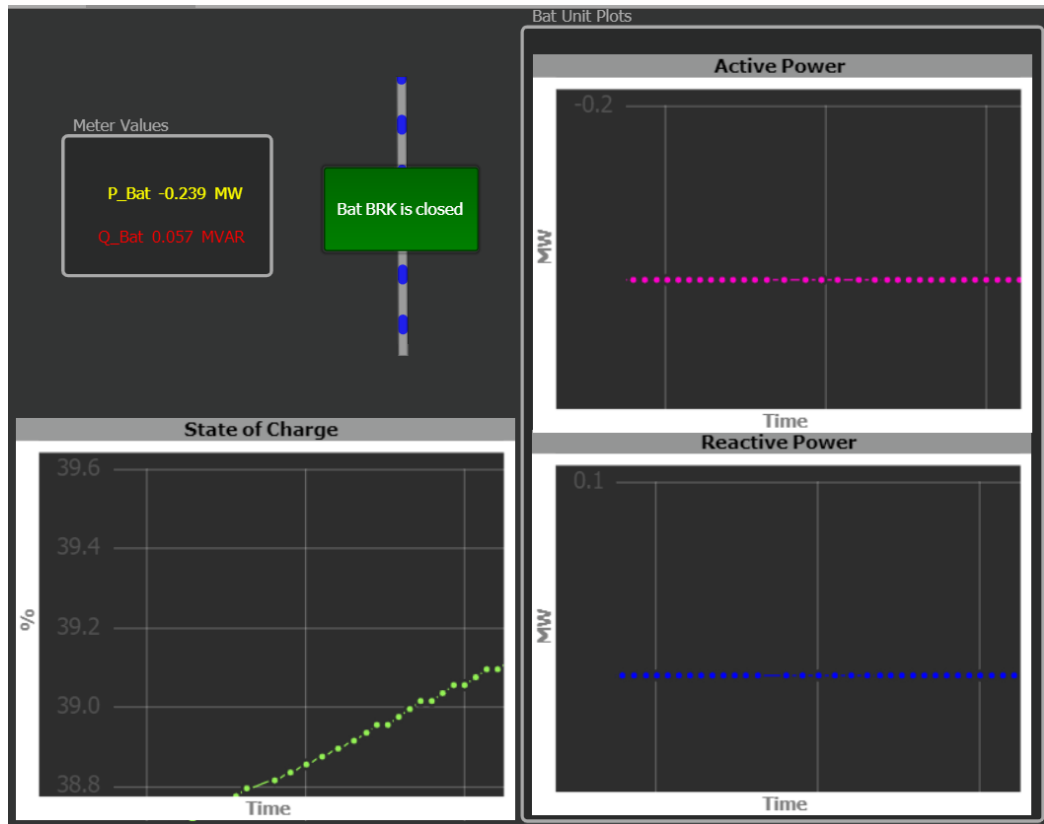


Figure 5-4: BESS HMI dashboard.

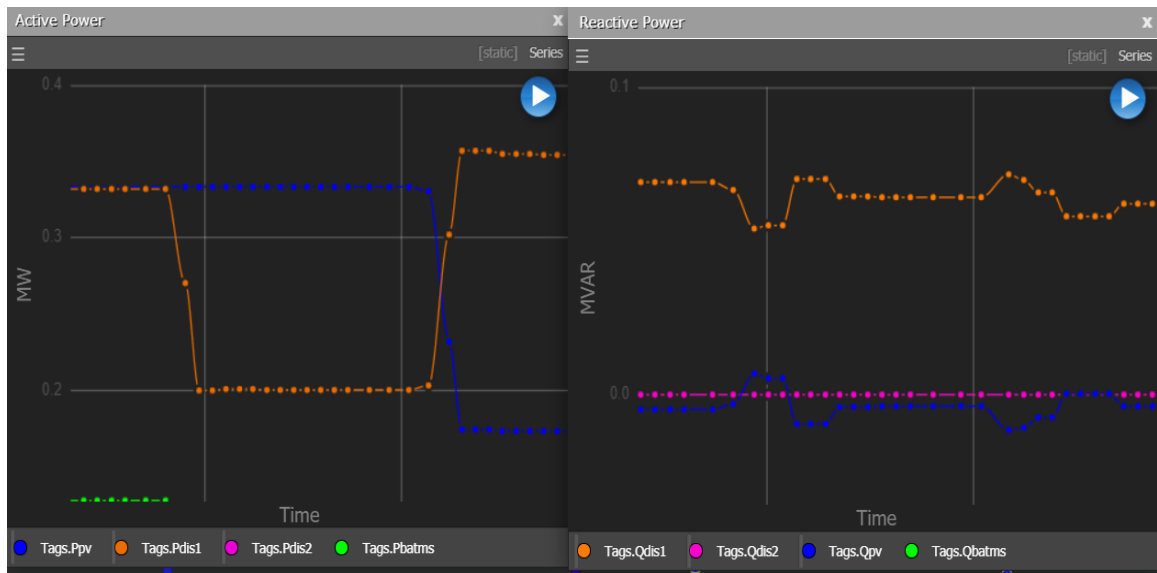


Figure 5-5: Active and reactive power trends.

5.3 Performance Testing

The developed CHIL simulation testbed was used to demonstrate the applicability of the microgrid operation considering a daily control horizon while highlighting the execution of important dispatch and transition functions. The test scenarios and cases were developed conforming to the IEEE 2030.8-2018 standard for testing of microgrid controllers. Furthermore, CHIL simulation tests were conducted in accordance to a laboratory benchmark CHIL testing procedure [16].

5.3.1 Results – PMS Functions

Figure 5-6 presents a scenario, where initially DIS-1, PV and BESS are supplying a load of 0.63 MW. The PV system output is 0.18 MW referenced by the MPPT controller corresponding to an irradiance of 300 W/m^2 . The BESS is discharging at 0.1 MW as commanded by the EMS and DIS-1 is supplying the power deficit. During this scenario, the SOC hits its minimum, which is set to 10%. Violation of the minimum SOC triggers loading check of DIS-1 and consequently, an emergency transition is initiated. Emergency transition enables DIS-2 with 800 kVA rating and then unloads DIS-1 with 400 kVA rating for smooth disconnection. In response to the emergency conditions, the BESS charges very slowly at -0.05 MW, and the PMS requests an updated operational plan for the system, considering the updated conditions. The frequency and voltage variations show a stable response.

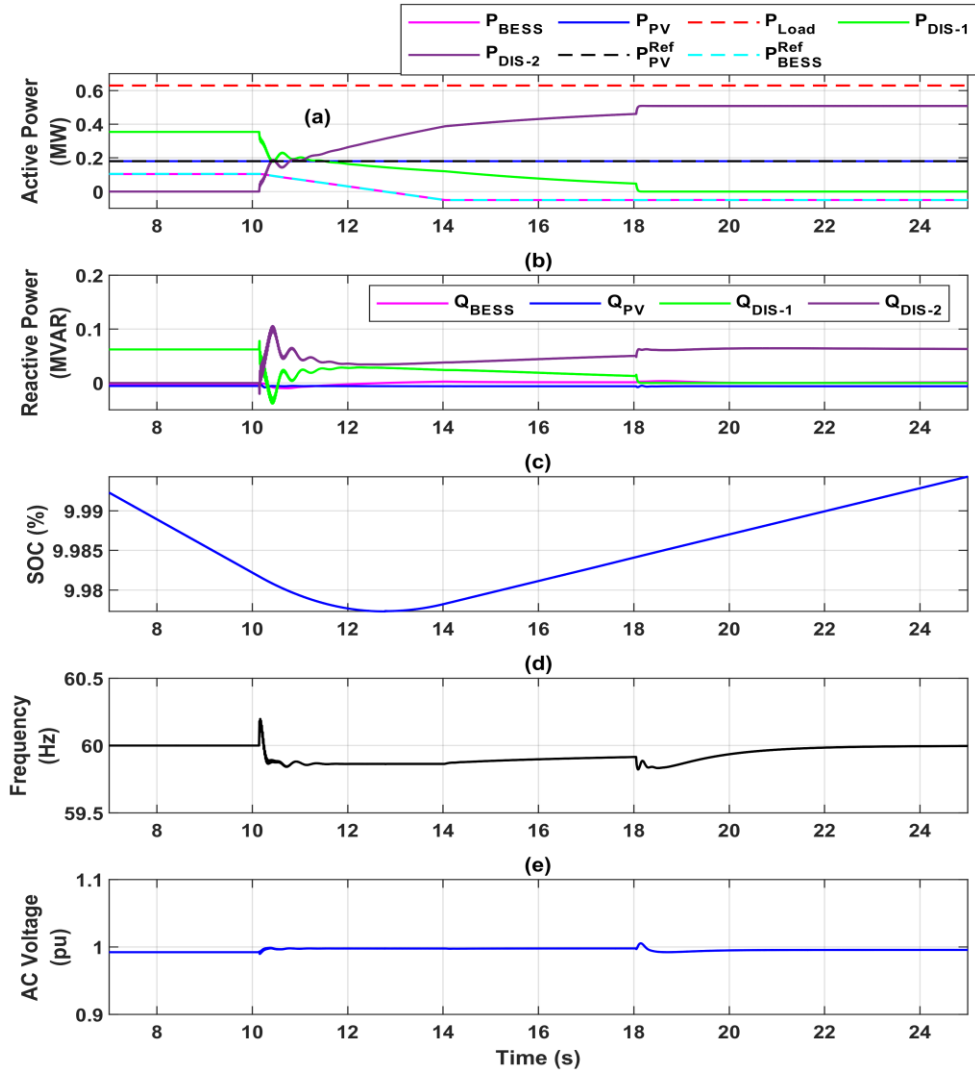


Figure 5-6: Emergency diesel generator transition during the GENSUP operation: (a) active power, (b) reactive power, (c) SOC, (d) frequency, and (e) AC voltage.

Figure 5-7 presents a case where DIS-1, BESS and PV are contributing to supply a load of 0.4 MW. Around 10 s, the SOC goes below its minimum value (10%) causing the PMS to check the loading of DIS-1. In contrast to the previous scenario, the loading of DIS-1 will be less than 80% of its rated value, and therefore the battery charges at -0.05 MW without enabling emergency condition. The voltage and frequency show a stable response.

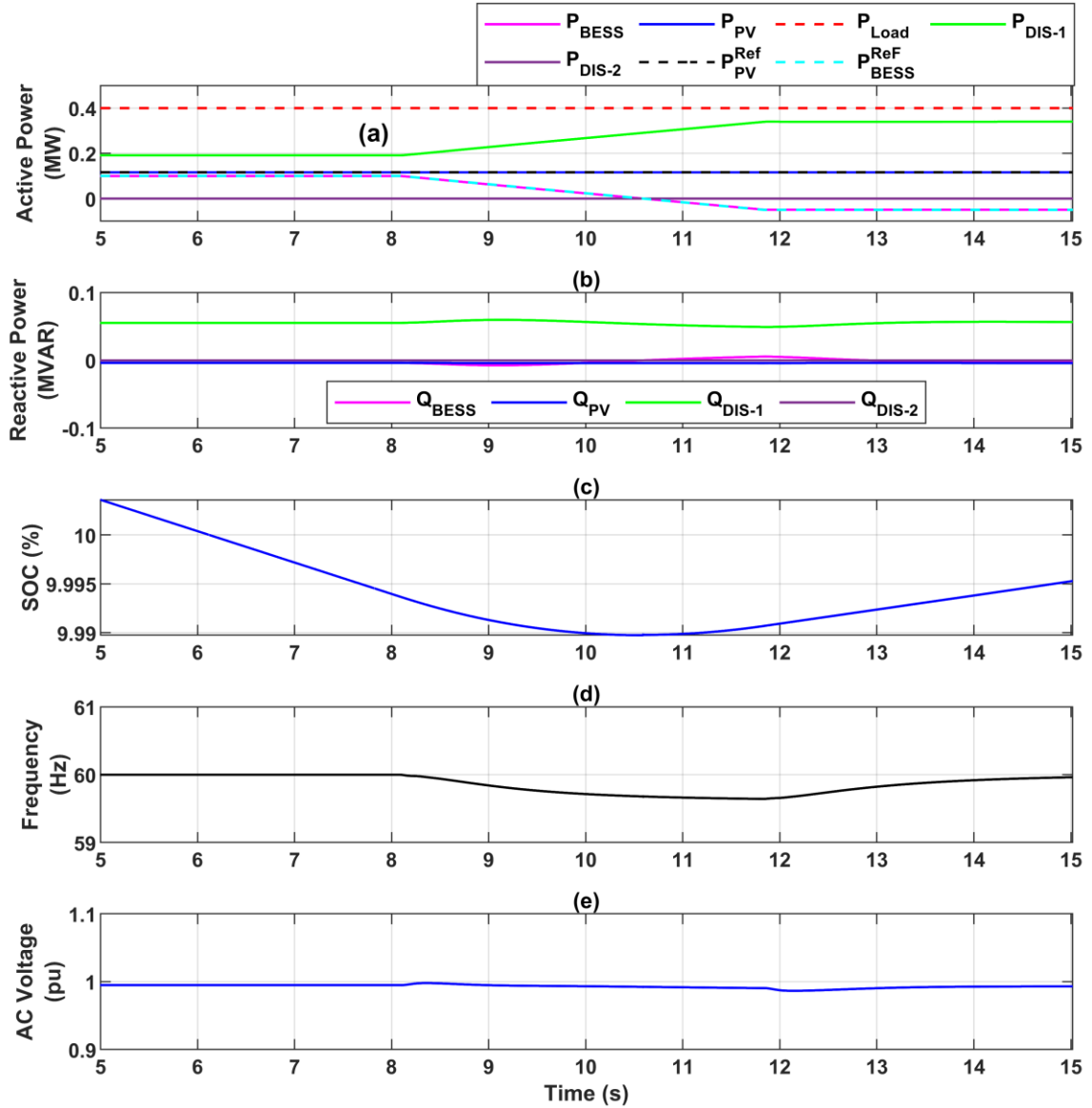


Figure 5-7: Power management when BESS reaches minimum SOC while in GENSUP mode: (a) active power, (b) reactive power, (c) SOC, (d) frequency, and (e) AC voltage.

Figure 5-8 presents a scenario, where the diesel plant is out of operation (Islanded mode), where the BESS operates in grid-forming mode and the PV is governed in grid-following control. The PV is supplying 0.28 MW under MPPT control for an irradiance of 500 W/m^2 and the BESS provides the required slack power. Around 4 s, the BESS SOC hits its minimum value, which is set to 10%. As a result, the PMS starts an emergency transition,

resulting in the connection of DIS-1. The dispatch strategy then turns from islanded to GENSUP mode and the battery charges slowly at -0.05 MW. Responding to the emergency situation, the PMS asks for an updated operational plan from the EMS control layer. The frequency shows a small deviation due to the connection of DIS-1 that settles at the nominal value at steady-state.

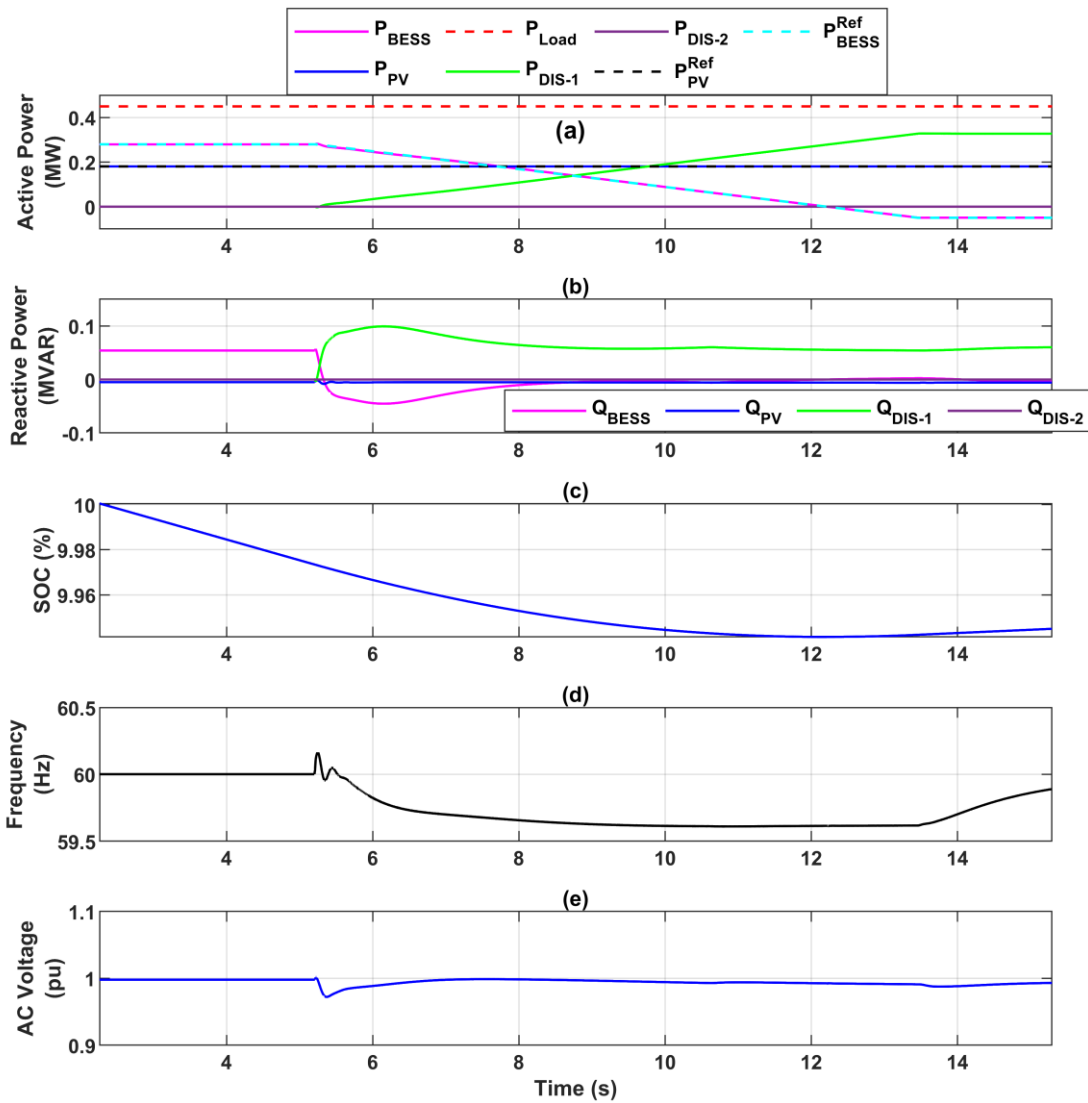


Figure 5-8: Emergency connection of a diesel generator in islanded mode (a) active power, (b) reactive power, (c) SOC, (d) frequency, and (e) AC voltage.

Figure 5-9 presents a case where the PV is initially supplying 0.18 MW at an irradiance of 300 W/m^2 , and BESS operates as a slack bus in grid-forming mode. For this scenario, the diesel plant is out of service and the battery keeps discharging for a sustained period of time due to persistent high load and low irradiance. Therefore, to prolong the system operation, and delay or prevent system blackout, an energy reserve scheme is applied. This scheme disconnects non-critical loads based on the priority, if the SOC of the battery is under a certain value. Around 280 s, a non-critical load disconnection occurred followed by another disconnection close to 1650 s as the SOC is getting very low as shown in Figure 5-9(a) and (c).

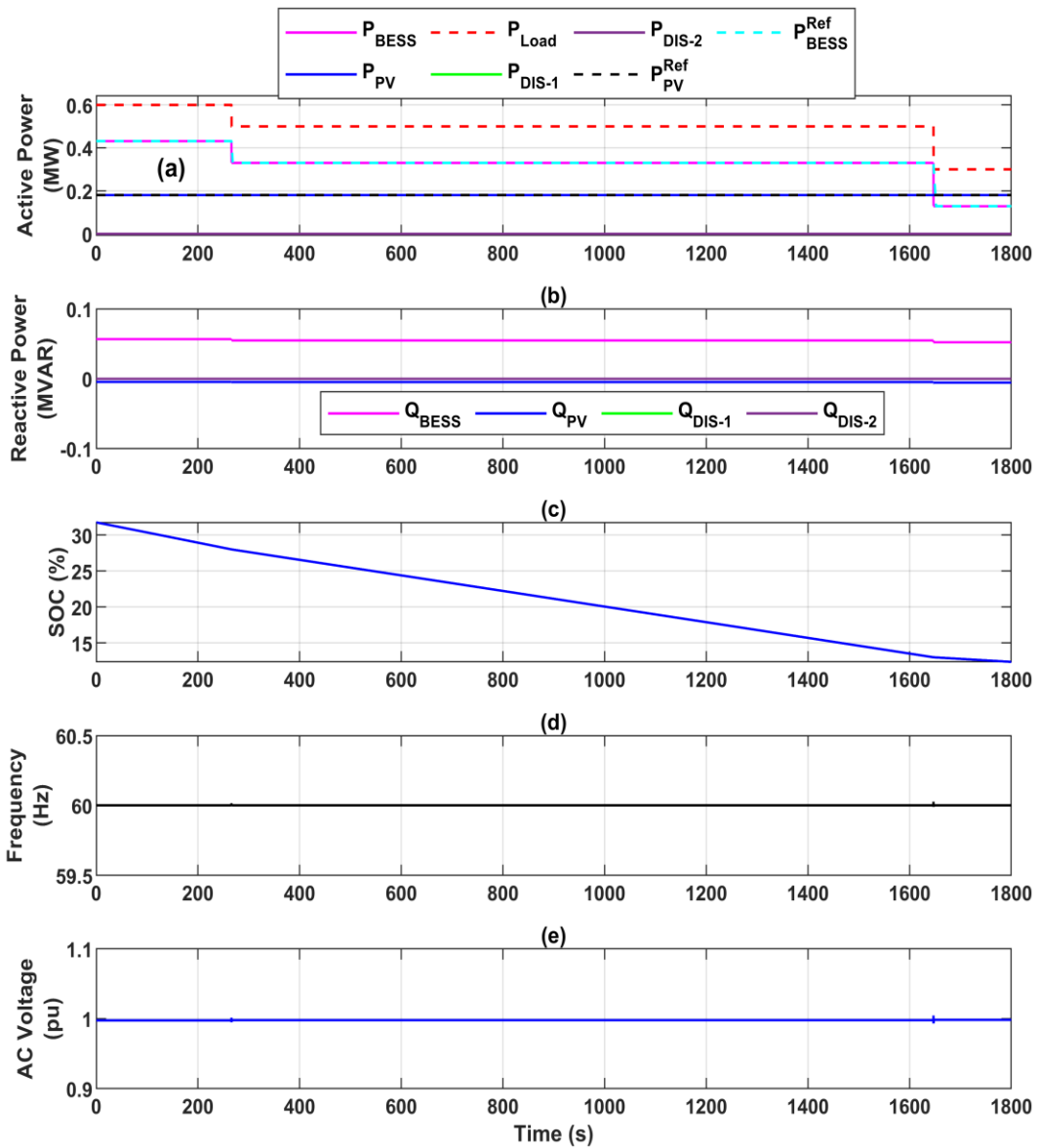


Figure 5-9: Islanded energy reserve scheme: (a) active power, (b) reactive power, (c) SOC, (d) frequency, and (e) AC voltage.

Figure 5-10 presents a scenario where DIS-1 is initially supplying around 0.35 MW, the BESS is discharging at 0.23 MW, and the PV follows the MPPT reference power at 0.18 MW for an irradiance of 300 W/m^2 . In response to DIS-1 sudden tripping close to 14 s, some of the loads are shed based on the priority, considering a higher reserve margin

during unplanned islanding transition to promote resiliency. Also, the BESS instantly switches to grid-forming mode. Around 43 s, some of the shed loads are restored, maintaining the required reserve by the islanded dispatch strategy. The frequency and voltage showcase depict a stable response during this event.

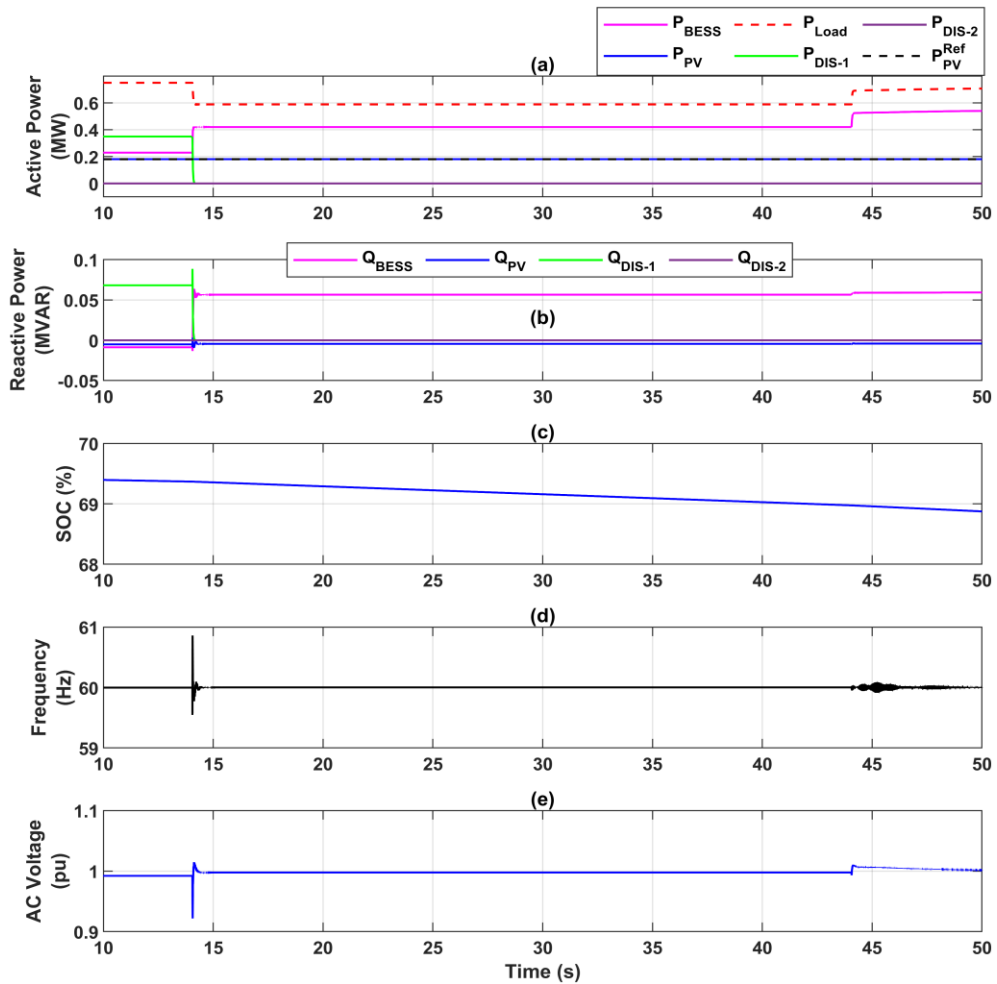


Figure 5-10: Unplanned islanding: (a) active power, (b) reactive power, (c) SOC, (d) frequency, and (e) AC voltage.

5.3.1.1 Results – EMS Functions

Figure 5-11 presents the forecasts and optimum operational setpoints generated by the EMS for the first hour of each look-ahead window for the entire 24-hr horizon. Figure 5-11 also shows the expected variation of BESS SOC under the forecasted load and solar irradiance, and the scheduled dispatch. The actual operational trajectory of the power system under the derived set-points is depicted in Figure 5-12. When analyzing Figure 5-11 and Figure 5-12, a good agreement can be seen in between the suggested optimum operational routine and the actual power system operation. No unstable system conditions that would obstruct the logical progression of the system operation were detected. This further confirms the competence of the proposed PMS in stably navigating the actual system operation while acting as an interface in between EMS and primary control layers. In the discussion that follows, the competence of the PMS will be assessed further considering specific test conditions detected during the daily operation.

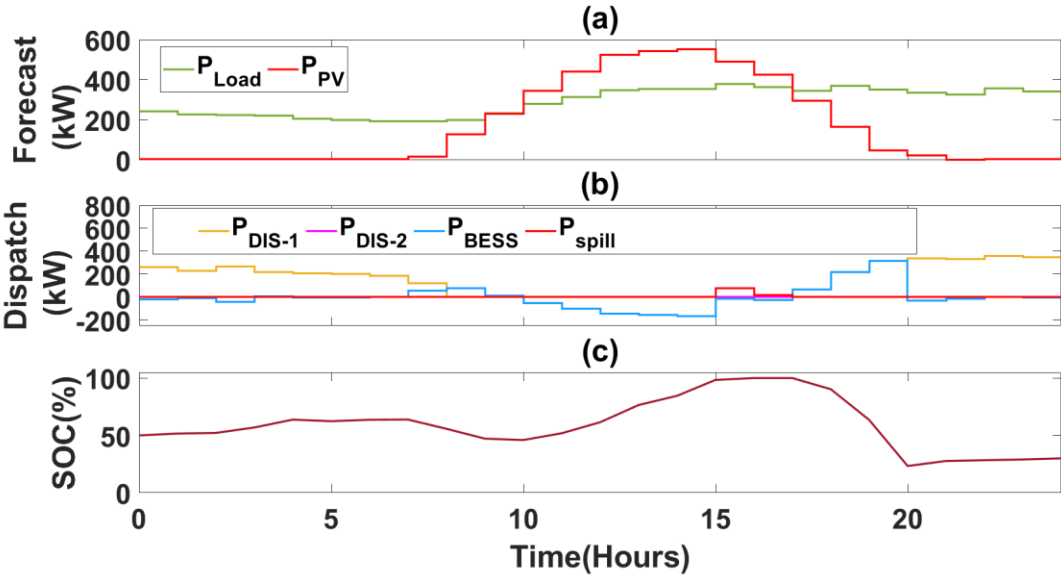


Figure 5-11: Optimum operational routine: (a) Forecasts, (b) dispatch, and (c) SOC.

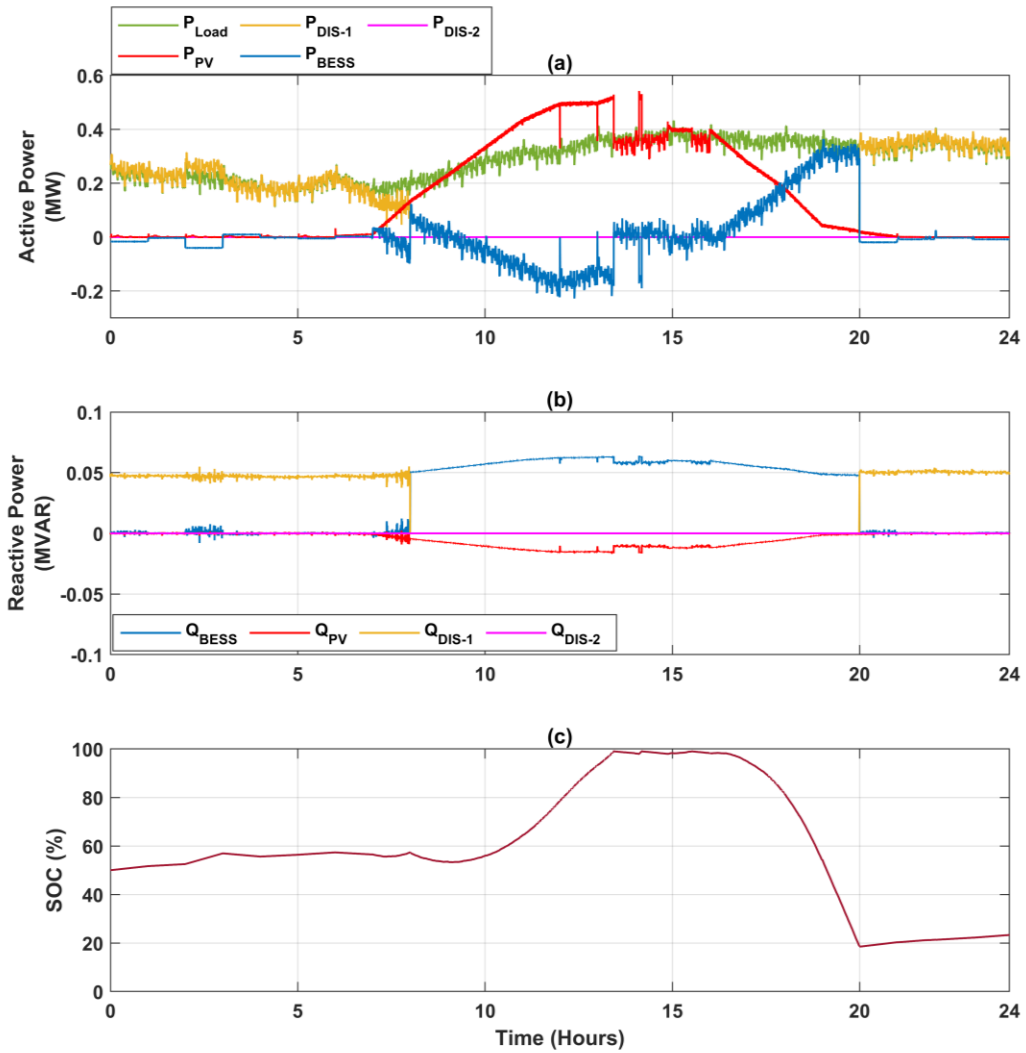


Figure 5-12: System actual operation: (a) active power, (b) reactive power, and (c) SOC.

Figure 5-13 shows the 8th hour of the day, where the DIS-1 active output power is around 0.14 MW, while the BESS is discharging at 0.034 MW following the EMS level control command (P_{BESS}^{EMS}), and the PV power is shifting upward following the increase in irradiation levels. The fluctuating nature of the load around 0.2 MW and the increase in PV power during this hour caused the DIS-1 to violate its minimum power requirement, which is 0.12 MW. Therefore, the PMS modifies the BESS power reference command to maintain the DIS-1 minimum power limit.

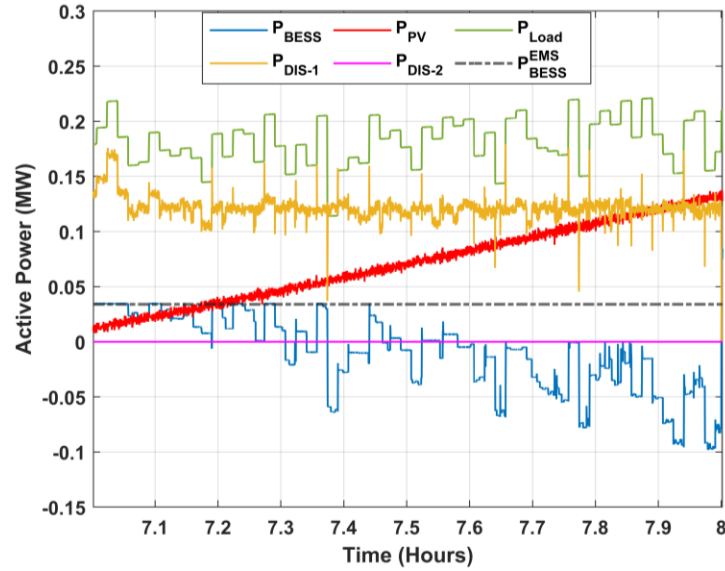


Figure 5-13: Diesel minimum loading scenario (8th hour): Active power.

Figure 5-14 presents a scenario where PMS responds to overloading of DIS-1 due to a sudden load increase. Initially, DIS-1 is supplying 0.38 MW while the BESS is charging at -0.0014 MW referenced by the EMS level signals (P_{BESS}^{EMS}). The PV unit active output is around zero corresponding to an irradiation level of zero W/m^2 . Due to the volatile nature of PV and load, the PMS incorporates a reserve capacity to deal with uncertainty. Hence, Diesel units tend to operate under their upper limits. A load increase takes a place close to 22.029 hr, violating the reserve constraint imposed by the secondary level control. Therefore, SEL-RTAC (PMS) commands the BESS to discharge at a higher level, overriding the EMS reference power command to prevent the overloading of DIS-1, and maintain the reserve requirement. Around 22.047 hr following a load decrease, the PMS instructs the BESS to follow its EMS reference signal according to the updated grid conditions.

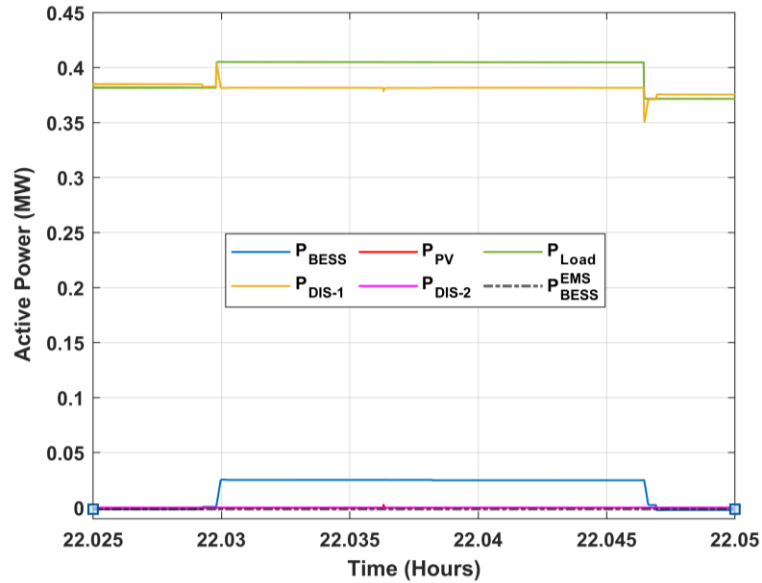


Figure 5-14: DIS-1 overloading scenario (23rd hour): Active power.

Figure 5-15 depicts the response when the PV unit enters limited-power mode to avoid overcharging the BESS. Initially, during this time frame, the PV is supplying 0.51 MW under MPPT control, while the BESS is forming the grid and providing the required active power slack. Close to 13.43 hr, the BESS reaches its maximum SOC, which is set to be 98.5% with a 0.5% hysteresis band as shown in Figure 5-15(b). The PMS anticipates an overcharging scenario and initiates PV limited-power mode. Subsequently, the PV unit starts tracking the load (P_{Load}) to push the BESS into an idle state while forming the grid. Close to 14.15 hr, the SOC hits 98%, which is the lower band of the hysteresis band. Therefore, MPPT mode is enabled and the BESS starts charging. As the SOC reaches 99% close to 14.18 hr, PV limited-power mode is activated. The mentioned scenarios satisfy the requirements of islanded dispatch test scenarios provided in Table 2 of IEEE 2030.8-2018.

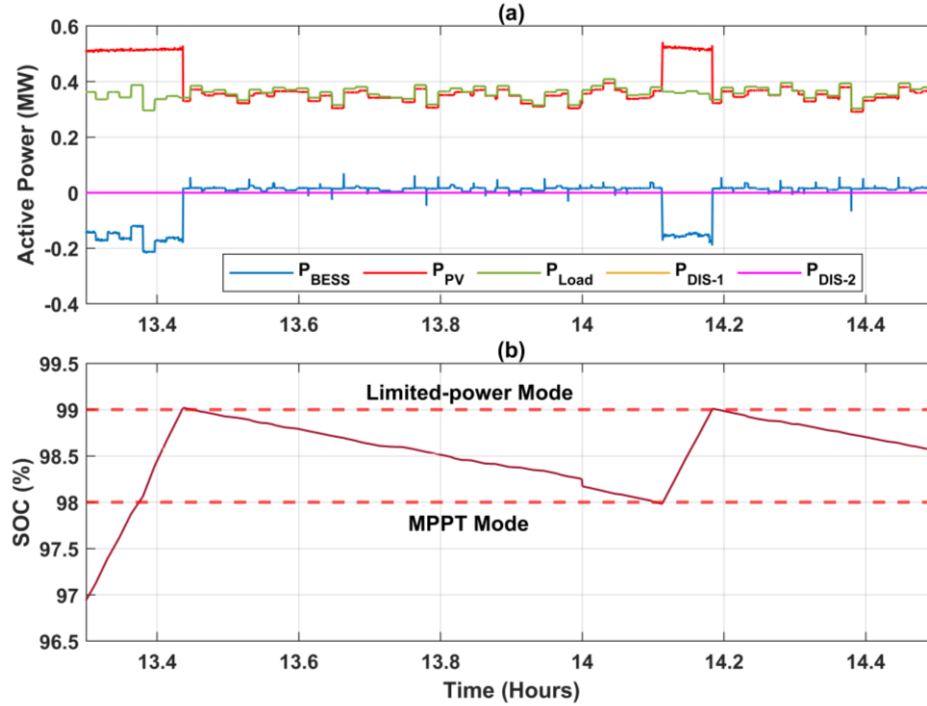


Figure 5-15: Results from 15th hour, when SOC reaches SOC_{MAX} : (a) active power and (b) SOC.

Figure 5-16 represents the experimental results of the planned islanding event at the start of the 9th hour. At first, DIS-1 is enabled and supplying power at 0.12 MW, the PV unit provides 0.13 MW under MPPT control, and the BESS outputs -0.078 MW. Around 8 hr the EMS level control requests the PMS to initiate an islanding scenario. The PMS then starts adjusting the active and reactive power at the POI by modifying the BESS power references in order to reduce the line current of the diesel unit to zero, which is very crucial to achieve seamless transitions. Around 8.003 hr, the PMS sends a disconnection signal to DIS-1 breaker (BRK_{DIS-1}) and turns the BESS control mode to grid-forming control. As depicted in Figure 5-16, this technique allows the system to island efficiently with minimal transients. This test was created according to Table 3 in IEEE 2030.8-2018.

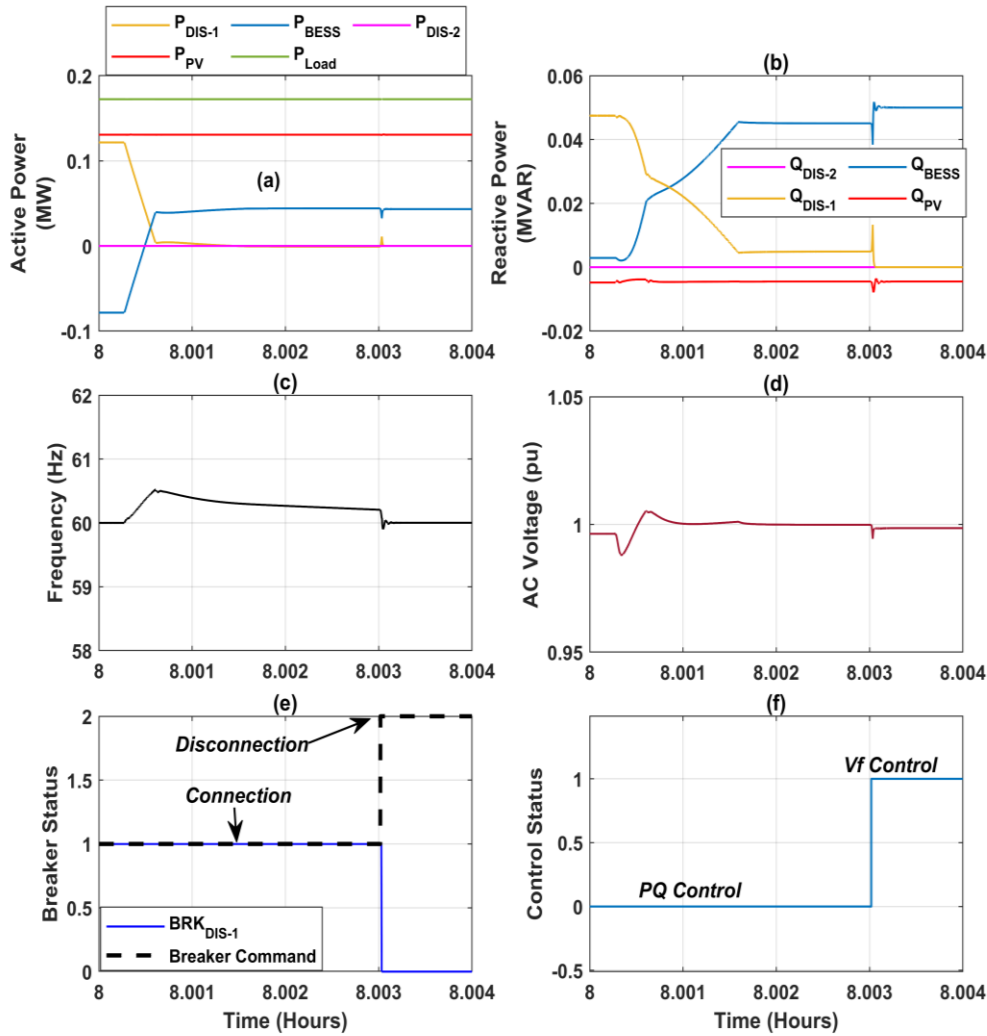


Figure 5-16: Planned islanding at the start of 9th hour: (a) active power, (b) reactive power, (c) frequency, (d) AC voltage, (e) diesel unit breaker status, and (f) BESS control mode.

Figure 5-17 shows the reconnection transition happening in the 21st hour. Initially, PV unit is governed by MPPT control while the BESS supplies the power balance operating in grid-forming mode. Around 20.005 hr, the PMS triggers a reconnection transition as recommended by the EMS. For reconnection, the PMS activates the synchronization scheme of DIS-1 to minimize the voltage and frequency difference over both sides of DIS-1 breaker. Close to 20.001 hr, once the voltage and frequency at both sides are below a certain threshold, a closing signal is sent to BRK_{DIS-1} . Following the DIS-1 connection,

the BESS switches to grid-following control and ramps down its power following the EMS power command. The developed reconnection test complies with Table 5 in IEEE 2030.8-2018.

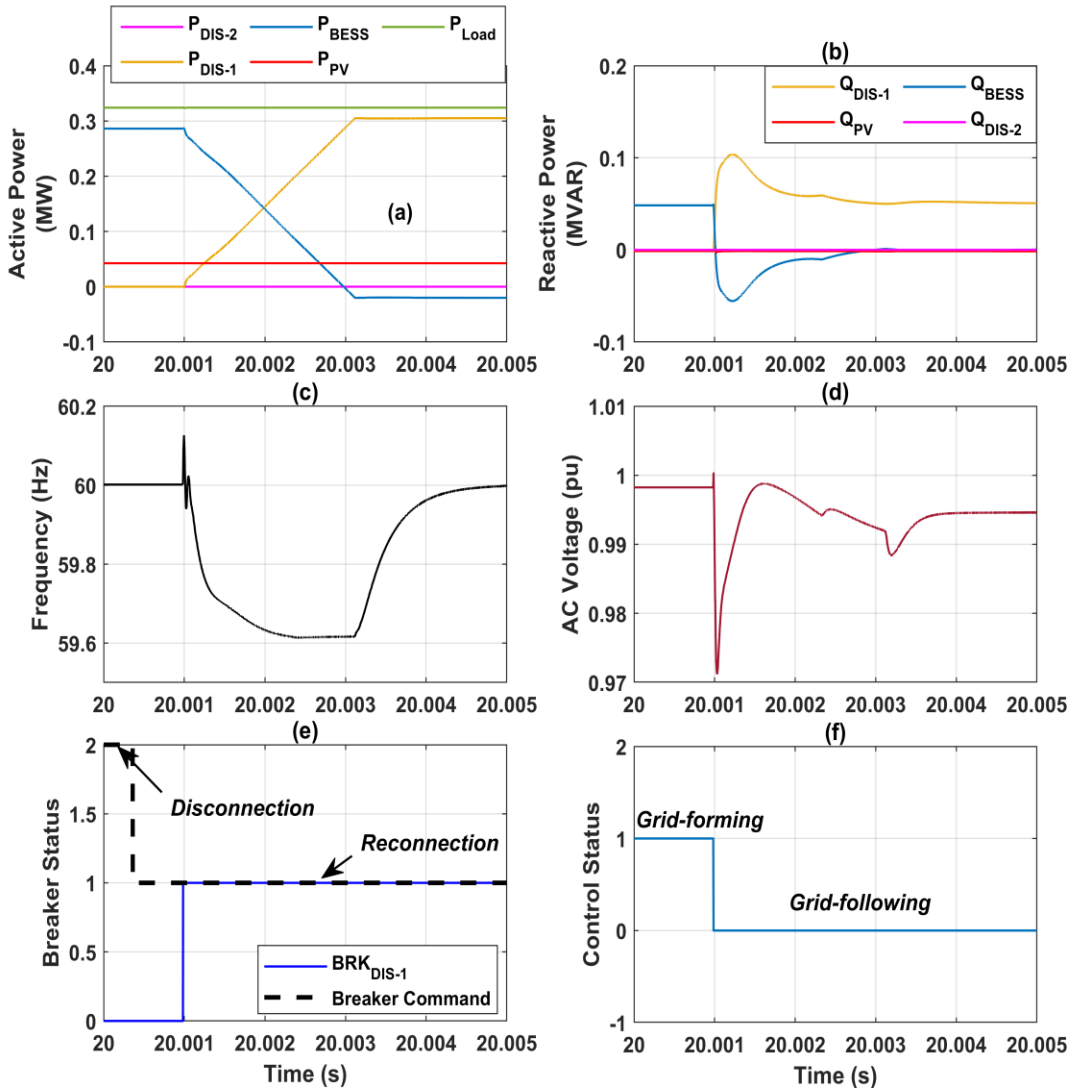


Figure 5-17: Reconnection at the start of 21st hour: (a) active power, (b) reactive power, (c) frequency, (d) AC voltage, (e) diesel unit breaker status, and (f) BESS control mode.

5.4 Summary

In this chapter, the steps followed in the development and evaluation of the microgrid testbed are presented. Short-term scenarios to target specific cases were considered to assess the performance of the proposed PMS. Moreover, the long-term overall operation derived from the EMS was evaluated under realistic system conditions simulated on the DRTS and control actions initiated by PMS to achieve the desired daily objectives and stable operation.

Chapter 6

Conclusions

6.1 Contributions and Conclusions

In this thesis, the implementation of a microgrid testbed composed of a real-time simulation model of a remote microgrid and a centralized microgrid controller is presented. The considered remote microgrid is modelled inside RTDS®, whereas the microgrid controller is developed on a SEL-RTAC automation controller to perform CHIL simulations. The main contributions of this work are listed below.

- A remote microgrid consisting of two diesel generators, a PV system and a BESS was modelled on a real-time simulation environment to facilitate hardware in the loop testing.
- Isochronous and droop control strategies were successfully implemented to govern the diesel plant operation. Two control strategies for PV and BESS, grid-following and grid-forming were implemented to permit the operation in GENSUP and islanded modes.
- A microgrid controller based on a centralized approach was developed in compliance with IEEE 2030.7-2017 standard. The centralized controller includes a PMS that contains two functions, dispatch and transitions functions. Two control strategies were considered for dispatch function to cover all expected scenarios in both GENSUP and

islanded modes. Reconnection, islanding and unplanned islanding are handled by the transition function. Furthermore, the dispatch and transition functions follow the recommended optimal schedule suggested by the EMS.

- An experimental test setup was implemented to test the proposed PMS. The proposed PMS was implemented on a real-time automation controller manufactured by Schweitzer Engineering Laboratories (SEL) called SEL RTAC-3350, representing a microgrid controller, which was interfaced to the RTDS® using GOOSE protocol for communicating measurements, status signals and control commands.
- The capability of GOOSE communication protocol to carry out data exchange between RTDS® and SEL RTAC-3350 for a PMS was tested.
- Development of test cases conforming to the IEEE 2030.8-2018 standard was accomplished. For example, 24 hours simulation scenario based on an optimization platform to extensively test the dispatch and transition functions was achieved. Short term simulations to target an expected scenario were also carried out.
- A web-based HMI to easily monitor and track the operation of the microgrid DERs was programmed.

Based on the carried research studies, the following conclusions can be drawn:

- In islanded mode, when the BESS operates in grid-forming mode, the PV system governed under the grid-following control performs well in achieving the expected output conditions under all considered operating modes.
- The conducted tests confirm the capability of the PV system to operate in grid-forming control along with the grid-forming BESS by deploying droop strategy, while maximizing the penetration of freely available solar energy.

- The conducted CHIL test scenarios considering a daily control horizon validated the competence of the proposed power management strategies in facilitating a stable power system operation under the influence of a quantitatively optimized operational routine. Seamless transitions can be also achieved through the developed PMS.
- PMS framework could successfully follow the unit commitment schedule provided by the optimization framework of the EMS, while adapting to the limitations of the units to attain stable power operation. The PMS could handle the unanticipated events by adjusting the unit commitments proposed by the EMS as needed, in order to protect the system and ensure the power supply to the loads.
- The reserve generation capacity accommodated by the PMS provided it adequate slack and time for responding to disturbances without overloading equipment and thus maintaining a stable operation.
- The developed testbed provides a flexible experimental setup for microgrid operational planning and evaluation and it can be further expanded easily to include more DERs for research purposes.
- The competence of the IEC 61850 GOOSE communication protocol to facilitate the interaction between the microgrid control system and the microgrid components was validated.
- The developed laboratory testbed setup can be further used to provide a realistic environment to test EMS algorithms for research purposes as well as for teaching purposes.

6.2 Future Work

In the context of this thesis, the following research are recommended as future work.

- Interface the DRTS with the existing rooftop weather station to provide real-time weather data for the simulated PV system.
- Development of an islanding detection algorithm to detect sudden disconnection of the diesel plant.
- Implementation of protection and relay settings for GENSUP and islanded modes. For example, when diesel plant is disconnected, protection system must adapt to the change in fault conditions as VSCs are current limited sources.
- Expand the microgrid model further by integrating more DERs and modelling a distribution network to capture accurate load dynamics.
- Extend the PMS to include search algorithm to select proper loads to be shed with the objective to minimize load shedding. This can be helpful when many loads are connected.

Appendix. A

Table A-1: SEL RTAC input and output signals.

SEL RTAC	Input from RTDS	Output to RTDS
	P_{DIS-1}	P_{PV}^{PMS}
	P_{DIS-2}	P_{BESS}^{PMS}
	P_{PV}	$P_{Shed}^{Interruptible}$
	P_{BESS}	$P_{Shed}^{Priority}$
	P_{Load}	$P_{Shed}^{Critical}$
	Q_{DIS-1}	Q_{BESS}^{PMS}
	Q_{DIS-2}	DIS-1 unloading signal
	Q_{Load}	DIS-2 unloading signal
	SOC	DIS-1 ON/OFF signal, including synchronization and synchro-check
	$Irradiance$	DIS-2 ON/OFF signals, including synchronization and synchro-check
	$Load_{Interruptible}$	Battery operation mode (Vf or PQ)
	$Load_{Priority}$	-----
	$Load_{Critical}$	-----
	CB_{DIS-1}	-----
	CB_{DIS-2}	-----
	CB_{PV}	-----
	CB_{BESS}	-----

Table A-2: EMS input and output signals.

EMS	Input from RTAC	Output to RTAC
	SOC	U_{DIS-1}^{EMS}
	Load average	U_{DIS-2}^{EMS}
	DERs dispatch average	P_{BESS}^{EMS}

References

- [1] R. Lasseter, A. Akhil, C. Marnay, and J. Ste, “Consortium for Electric Reliability Technology Solutions White Paper on Integration of Distributed Energy Resources The MicroGrid Concept,” no. April, 2002.
- [2] IEEE Standard Association, *IEEE Std. 1547-2018. Standard for Interconnection and Interoperability of Distributed Energy Resources with Associated Electric Power Systems Interfaces*. 2018.
- [3] F. Katiraei, R. Iravani, N. Hatziargyriou, and A. Dimeas, “Microgrids management,” *IEEE Power Energy Mag.*, vol. 6, no. 3, pp. 54–65, May 2008, doi: 10.1109/MPE.2008.918702.
- [4] R. Kaluthanthrige, A. D. Rajapakse, C. Lamothe, and F. Mosallat, “Optimal Sizing and Performance Evaluation of a Hybrid Renewable Energy System for an Off-Grid Power System in Northern Canada,” *Technol. Econ. Smart Grids Sustain. Energy*, vol. 4, no. 1, pp. 24–26, 2019, doi: 10.1007/s40866-019-0061-5.
- [5] P. Bajpai and V. Dash, “Hybrid renewable energy systems for power generation in stand-alone applications: A review,” *Renew. Sustain. Energy Rev.*, vol. 16, no. 5, pp. 2926–2939, Jun. 2012, doi: 10.1016/j.rser.2012.02.009.
- [6] M. M. Mahmoud and I. H. Ibrik, “Techno-economic feasibility of energy supply of remote villages in Palestine by PV-systems, diesel generators and electric grid,” *Renew. Sustain. Energy Rev.*, vol. 10, no. 2, pp. 128–138, 2006, doi:

10.1016/j.rser.2004.09.001.

- [7] E. M. Nfah, J. M. Ngundam, and R. Tchinda, “Modelling of solar/diesel/battery hybrid power systems for far-north Cameroon,” *Renew. Energy*, vol. 32, no. 5, pp. 832–844, Apr. 2007, doi: 10.1016/j.renene.2006.03.010.
- [8] R. Kaluthanthrige and A. D. Rajapakse, “Operational Optimization of a Remote Off-Grid Hybrid Renewable Energy System in Northern Canada,” *2019 IEEE 7th Int. Conf. Smart Energy Grid Eng.*, pp. 268–273, 2019, doi: 10.1109/sege.2019.8859885.
- [9] A. Bidram and A. Davoudi, “Hierarchical Structure of Microgrids Control System,” *IEEE Trans. Smart Grid*, vol. 3, no. 4, pp. 1963–1976, Dec. 2012, doi: 10.1109/TSG.2012.2197425.
- [10] R. Kaluthanthrige and A. D. Rajapakse, “Evaluation of hierarchical controls to manage power, energy and daily operation of remote off-grid power systems,” *Appl. Energy*, vol. 299, no. June, p. 117259, Oct. 2021, doi: 10.1016/j.apenergy.2021.117259.
- [11] M. Farraj, R. Kaluthanthrige, and A. Rajapakse, “Evaluating a Microgrid Control System Using Controller Hardware in the Loop Simulations,” 2021.
- [12] *IEEE Standard for the Specification of Microgrid Controllers*. 2018.
- [13] *IEEE Standard for the Testing of Microgrid Controllers*. 2018.
- [14] A. S. Vijay, S. Doolla, and M. C. Chandorkar, “Real-Time Testing Approaches for Microgrids,” *IEEE J. Emerg. Sel. Top. Power Electron.*, vol. 5, no. 3, pp. 1356–

1376, 2017, doi: 10.1109/JESTPE.2017.2695486.

- [15] R. H. Lasseter *et al.*, “CERTS microgrid laboratory test bed,” *IEEE Trans. Power Deliv.*, vol. 26, no. 1, pp. 325–332, 2011, doi: 10.1109/TPWRD.2010.2051819.
- [16] P. Kotsampopoulos *et al.*, “A Benchmark System for Hardware-in-the-Loop Testing of Distributed Energy Resources,” *IEEE Power Energy Technol. Syst. J.*, vol. 5, no. 3, pp. 94–103, 2018, doi: 10.1109/jpets.2018.2861559.
- [17] B. Xiao *et al.*, “Development of hardware-in-the-loop microgrid testbed,” *2015 IEEE Energy Convers. Congr. Expo. ECCE 2015*, pp. 1196–1202, 2015, doi: 10.1109/ECCE.2015.7309827.
- [18] M. Rasheduzzaman, S. N. Bhaskara, and B. H. Chowdhury, “Implementation of a microgrid central controller in a laboratory microgrid network,” *2012 North Am. Power Symp. NAPS 2012*, pp. 1–6, 2012, doi: 10.1109/NAPS.2012.6336332.
- [19] K. Prabakar *et al.*, “Site-Specific Evaluation of Microgrid Controller Using Controller and Power-Hardware-in-the-Loop,” *IECON Proc. (Industrial Electron. Conf.)*, vol. 2019-Octob, pp. 6463–6468, 2019, doi: 10.1109/IECON.2019.8927354.
- [20] J. H. Jeon *et al.*, “Development of hardware in-the-loop simulation system for testing operation and control functions of microgrid,” *IEEE Trans. Power Electron.*, vol. 25, no. 12, pp. 2919–2929, 2010, doi: 10.1109/TPEL.2010.2078518.
- [21] C. Sun *et al.*, “Design and Real-Time Implementation of a Centralized Microgrid Control System with Rule-Based Dispatch and Seamless Transition Function,” *IEEE Trans. Ind. Appl.*, vol. 56, no. 3, pp. 3168–3177, 2020, doi: 10.1109/TIA.2020.2979790.

- [22] C. Sun, J. N. Paquin, F. Al Jajeh, G. Joos, and F. Bouffard, "Implementation and CHIL Testing of a Microgrid Control System," *2018 IEEE Energy Convers. Congr. Expo. ECCE 2018*, pp. 2073–2080, 2018, doi: 10.1109/ECCE.2018.8557761.
- [23] H. Shayeghi and A. Younesi, *Microgrid Architectures, Control and Protection Methods*, no. January. 2020.
- [24] Q. Long *et al.*, "Community Microgrid Controller Evaluation using Hardware-in-the-Loop Testbed," *2018 North Am. Power Symp. NAPS 2018*, 2019, doi: 10.1109/NAPS.2018.8600556.
- [25] B. Xiao *et al.*, "Implementation of system level control and communications in a Hardware-in-the-Loop microgrid testbed," *2016 IEEE Power Energy Soc. Innov. Smart Grid Technol. Conf. ISGT 2016*, pp. 1–5, 2016, doi: 10.1109/ISGT.2016.7781245.
- [26] S. Marzal, R. Salas, R. González-Medina, G. Garcerá, and E. Figueres, "Current challenges and future trends in the field of communication architectures for microgrids," *Renew. Sustain. Energy Rev.*, vol. 82, no. October 2017, pp. 3610–3622, Feb. 2018, doi: 10.1016/j.rser.2017.10.101.
- [27] S. Kariyawasam, "Implementation of an IEC 61850 Sampled Values Based Line Protection IED with a New Transients-Based Hybrid Protection Algorithm," 2016.
- [28] Amulya, M. Patil, S. R. Bhide, and S. S. Bhat, "Experimenting with IEC 61850 and GOOSE messaging," in *2017 4th International Conference on Power, Control & Embedded Systems (ICPCES)*, Mar. 2017, vol. 2017-Janua, pp. 1–6, doi: 10.1109/ICPCES.2017.8117641.

- [29] R. Preston and C. Guerriero, "Utilizing GOOSE-based protection schemes to attain compliance with regulatory testing requirements," in *2014 67th Annual Conference for Protective Relay Engineers*, Mar. 2014, pp. 588–595, doi: 10.1109/CPRE.2014.6799030.
- [30] W. Huang, "Learn IEC 61850 configuration in 30 minutes," in *2018 71st Annual Conference for Protective Relay Engineers (CPRE)*, Mar. 2018, vol. 2018-Janua, pp. 1–5, doi: 10.1109/CPRE.2018.8349803.
- [31] C. Yang, J. Xu, and V. Vyatkin, "Towards Implementation of IEC 61850 GOOSE Messaging in Event-Driven IEC 61499 Environment," in *Proceedings of the 2014 IEEE Emerging Technology and Factory Automation (ETFA)*, 2014, pp. 1–4, doi: 10.1109/ETFA.2014.7005253.
- [32] Scott Aaronson, "6.045J Automata, Computability, and Complexity," *Massachusetts Institute of Technology: MIT OpenCourseWare*, <https://ocw.mit.edu>.
- [33] J. D. Hopcroft, John E. and Motwani, Rajeev and Ullman, *Introduction to Automata Theory, Languages, and Computation (3rd Edition)*. Addison-Wesley Longman Publishing Co., Inc., 2006.
- [34] X. Wang, J. M. Guerrero, and Z. Chen, "Control of grid interactive AC microgrids," *IEEE Int. Symp. Ind. Electron.*, pp. 2211–2216, 2010, doi: 10.1109/ISIE.2010.5637807.
- [35] S. Ansari, A. Chandel, and M. Tariq, "A Comprehensive Review on Power Converters Control and Control Strategies of AC/DC Microgrid," *IEEE Access*, vol.

XX, pp. 1–1, 2020, doi: 10.1109/ACCESS.2020.3020035.

- [36] J. Rocabert, A. Luna, F. Blaabjerg, and P. Rodríguez, “Control of Power Converters in AC Microgrids,” *IEEE Trans. Power Electron.*, vol. 27, no. 11, pp. 4734–4749, Nov. 2012, doi: 10.1109/TPEL.2012.2199334.
- [37] J. M. Guerrero, J. C. Vasquez, J. Matas, L. G. De Vicuña, and M. Castilla, “Hierarchical control of droop-controlled AC and DC microgrids - A general approach toward standardization,” *IEEE Trans. Ind. Electron.*, vol. 58, no. 1, pp. 158–172, 2011, doi: 10.1109/TIE.2010.2066534.
- [38] J. A. P. Lopes, C. L. Moreira, and A. G. Madureira, “Defining control strategies for analysing microgrids islanded operation,” *2005 IEEE Russ. Power Tech, PowerTech*, vol. 21, no. 2, pp. 916–924, 2005, doi: 10.1109/PTC.2005.4524548.
- [39] O. Palizban, K. Kauhaniemi, and J. M. Guerrero, “Microgrids in active network management - Part I: Hierarchical control, energy storage, virtual power plants, and market participation,” *Renew. Sustain. Energy Rev.*, vol. 36, pp. 428–439, 2014, doi: 10.1016/j.rser.2014.01.016.
- [40] Y. Hao, G. Wang, K. Wang, and Z. Deng, “Application of a novel virtual synchronous generator technology in islanded microgrid,” *2017 IEEE Conf. Energy Internet Energy Syst. Integr. EI2 2017 - Proc.*, vol. 2018-Janua, pp. 1–6, 2017, doi: 10.1109/EI2.2017.8245314.
- [41] D. Wang and H. Wu, “Application of virtual synchronous generator technology in microgrid,” *2016 IEEE 8th Int. Power Electron. Motion Control Conf. IPEMC-ECCE Asia 2016*, pp. 3142–3148, 2016, doi: 10.1109/IPEMC.2016.7512798.

- [42] A. Merabet, K. T. Ahmed, H. Ibrahim, R. Beguenane, and A. M. Y. M. Ghias, "Energy Management and Control System for Laboratory Scale Microgrid Based Wind-PV-Battery," *IEEE Trans. Sustain. Energy*, vol. 8, no. 1, pp. 145–154, 2017, doi: 10.1109/TSTE.2016.2587828.
- [43] Y. Guan, J. C. Vasquez, J. M. Guerrero, Y. Wang and W. Feng, "Frequency Stability of Hierarchically Controlled Hybrid Photovoltaic-Battery-Hydropower Microgrids," *IEEE Trans. Ind. Appl.*, vol. 51, no. 6, pp. 4729–4742, 2015, doi: 10.1109/TIA.2015.2458954.
- [44] Z. Yi, S. Member, W. Dong, and A. H. Etemadi, "A Unified Control and Power Management Scheme for PV-Battery-Based Hybrid Microgrids for Both Grid-Connected and Islanded Modes," vol. 9, no. 6, pp. 5975–5985, 2018.
- [45] M. S. Behzadi and M. Niasati, "Comparative performance analysis of a hybrid PV/FC/battery stand-alone system using different power management strategies and sizing approaches," *Int. J. Hydrogen Energy*, vol. 40, no. 1, pp. 538–548, Jan. 2015, doi: 10.1016/j.ijhydene.2014.10.097.
- [46] S. Wen, S. Wang, G. Liu, and R. Liu, "Energy management and coordinated control strategy of PV/HESS AC microgrid during islanded operation," *IEEE Access*, vol. 7, pp. 4432–4441, 2019, doi: 10.1109/ACCESS.2018.2887114.
- [47] Y. Karimi, H. Oraee, and J. M. Guerrero, "Decentralized Method for Load Sharing and Power Management in a Hybrid Single/Three-Phase-Islanded Microgrid Consisting of Hybrid Source PV/Battery Units," *IEEE Trans. Power Electron.*, vol. 32, no. 8, pp. 6135–6144, 2017, doi: 10.1109/TPEL.2016.2620258.

- [48] H. Mahmood, D. Michaelson, and J. Jiang, “A power management strategy for PV/battery hybrid systems in Islanded microgrids,” *IEEE J. Emerg. Sel. Top. Power Electron.*, vol. 2, no. 4, pp. 870–882, 2014, doi: 10.1109/JESTPE.2014.2334051.
- [49] T. Dragicevic, J. M. Guerrero, J. C. Vasquez, and D. Skrlec, “Supervisory Control of an Adaptive-Droop Regulated DC Microgrid With Battery Management Capability,” *IEEE Trans. Power Electron.*, vol. 29, no. 2, pp. 695–706, Feb. 2014, doi: 10.1109/TPEL.2013.2257857.
- [50] Z. Jin, J. Zhang, A. Ghasaei, and R. Iravani, “Transient Study of an Automata-Based Microgrid Supervisory Control,” *Int. Conf. Power Syst. Transients*, 2019.
- [51] A. Ghasaei, Z. J. Zhang, W. M. Wonham, and R. Iravani, “A Discrete-Event Supervisory Control for the AC Microgrid,” *IEEE Trans. Power Deliv.*, vol. 8977, no. c, pp. 1–1, 2020, doi: 10.1109/tpwr.2020.2988687.
- [52] X. Lu, M. Zhou, A. C. Ammari, and J. Ji, “Hybrid Petri nets for modeling and analysis of microgrid systems,” *IEEE/CAA J. Autom. Sin.*, vol. 3, no. 4, pp. 349–356, 2016, doi: 10.1109/JAS.2016.7510070.
- [53] P. Kotsampopoulos *et al.*, “A Benchmark System for Hardware-in-the-Loop Testing of Distributed Energy Resources,” *IEEE Power Energy Technol. Syst. J.*, vol. 5, no. 3, pp. 94–103, 2018, doi: 10.1109/jpets.2018.2861559.
- [54] G. Jóos, B. T. Ooi, D. McGillis, F. D. Galiana, and R. Marceau, “The potential of distributed generation to provide ancillary services,” *Proc. IEEE Power Eng. Soc. Transm. Distrib. Conf.*, vol. 3, no. d, pp. 1762–1767, 2000, doi: 10.1109/pess.2000.868792.

- [55] O. Nzimako and A. Rajapakse, "Real time simulation of a microgrid with multiple distributed energy resources," in *2016 International Conference on Cogeneration, Small Power Plants and District Energy (ICUE)*, Sep. 2016, no. August, pp. 1–6, doi: 10.1109/COGEN.2016.7728945.
- [56] H. Saadat, "Power System Analysis," *Milwaukee: McGraw-Hill*. 2002.
- [57] P. Kundur, *Power System Stability and Control Volume I*. 1994.
- [58] M. G. Villalva, J. R. Gazoli, and E. R. Filho, "Comprehensive Approach to Modeling and Simulation of Photovoltaic Arrays," *IEEE Trans. Power Electron.*, vol. 24, no. 5, pp. 1198–1208, 2009, doi: 10.1109/TPEL.2009.2013862.
- [59] Z. Chen, R. H. Lasseter, and T. M. Jahns, "Active Power Reserve Control for Grid-Forming PV Sources in Microgrids using Model-based Maximum Power Point Estimation," in *2019 IEEE Energy Conversion Congress and Exposition (ECCE)*, Sep. 2019, pp. 41–48, doi: 10.1109/ECCE.2019.8913174.
- [60] R. Technologies, "RTDS Manuals and Documentation." Winnipeg, 2009.
- [61] R. W. Erickson, *Fundamentals of Power Electronics*. Boston, MA: Springer US, 1997.
- [62] S. Ben-Yaakov, "Average simulation of PWM converters by direct implementation of behavioral relationships," in *Proceedings Eighth Annual Applied Power Electronics Conference and Exposition*, 1993, vol. 77, no. 5, pp. 510–516, doi: 10.1109/APEC.1993.290710.
- [63] A. D. F. Katiraei, R. Iravani, N. Hatziargyriou, "Microgrids Mamageent," *katiraei*,

Farid Iravani, Reza Hatziargyriou, Nikos Dimeas, Aris, no. june, pp. 54–65, 2008.

- [64] M. B. Delghavi and A. Yazdani, “A control strategy for islanded operation of a distributed resource (DR) unit,” *2009 IEEE Power Energy Soc. Gen. Meet. PES '09*, pp. 1–8, 2009, doi: 10.1109/PES.2009.5275592.
- [65] A. Yazdani and P. P. Dash, “A control methodology and characterization of dynamics for a photovoltaic (PV) system interfaced with a distribution network,” *IEEE Trans. Power Deliv.*, vol. 24, no. 3, pp. 1538–1551, 2009, doi: 10.1109/TPWRD.2009.2016632.
- [66] L. Huang, H. Xin, Z. Wang, L. Zhang, K. Wu, and J. Hu, “Transient Stability Analysis and Control Design of Droop-Controlled Voltage Source Converters Considering Current Limitation,” *IEEE Trans. Smart Grid*, vol. 10, no. 1, pp. 578–591, 2019, doi: 10.1109/TSG.2017.2749259.
- [67] W. Yao, M. Chen, J. Matas, J. M. Guerrero, and Z. M. Qian, “Design and analysis of the droop control method for parallel inverters considering the impact of the complex impedance on the power sharing,” *IEEE Trans. Ind. Electron.*, vol. 58, no. 2, pp. 576–588, 2011, doi: 10.1109/TIE.2010.2046001.
- [68] Z. Chen, R. H. Lasseter, and T. M. Jahns, “Active power reserve control for grid-forming PV sources in microgrids using model-based maximum power point estimation,” *2019 IEEE Energy Convers. Congr. Expo. ECCE 2019*, pp. 41–48, 2019, doi: 10.1109/ECCE.2019.8913174.
- [69] Yu-Pei Huang, “A Rapid Maximum Power Measurement System for High-Concentration Photovoltaic Modules Using the Fractional Open-Circuit Voltage

Technique and Controllable Electronic Load,” *IEEE J. Photovoltaics*, vol. 4, no. 6, pp. 1610–1617, Nov. 2014, doi: 10.1109/JPHOTOV.2014.2351613.

- [70] R. Kaluthanthrige and A. D. Rajapakse, “Demand response integrated day-ahead energy management strategy for remote off-grid hybrid renewable energy systems,” *Int. J. Electr. Power Energy Syst.*, vol. 129, no. December 2020, p. 106731, Jul. 2021, doi: 10.1016/j.ijepes.2020.106731.
- [71] F. Katiraei and C. Abbey, “Diesel Plant Sizing and Performance Analysis of a Remote Wind-Diesel Microgrid,” in *2007 IEEE Power Engineering Society General Meeting*, Jun. 2007, pp. 1–8, doi: 10.1109/PES.2007.386275.
- [72] Y. A. I. Mohamed, “New control algorithms for the distributed generation interface in grid-connected and micro-grid system,” *Ph.D. Diss. Univ. Waterloo, Waterloo, ON, Canada*, 2008.
- [73] Z. Gajić, S. Aganović, J. Benović, G. Leci, and S. Gazzari, “Using IEC 61850 analogue GOOSE messages for OLTC control of parallel transformers,” *IET Conf. Publ.*, vol. 2010, no. 558 CP, 2010, doi: 10.1049/cp.2010.0227.